Halbach Arrays in Aerospace Axial and Radial Flux Machines

Use of Halbach Arrays in Axial and Radial Flux Permanent Magnet Machines for Aerospace Applications

By ALEXANDER FORSYTH, B.A., B.A.Sc.

A Thesis Submitted to the School of Graduate Studies in Partial Fulfillment of the Requirements for the Degree of Master of Applied Science

McMaster University

McMaster University MASTER OF APPLIED SCIENCE (2023) Hamilton, Ontario, Canada (Electrical and Computer Engineering)

TITLE: Use of Halbach Arrays in Axial and Radial Flux Permanent Magnet Machines for Aerospace Applications

AUTHOR: Alexander Forsyth, B.A. (York University), B.A.Sc. (University of Waterloo)

SUPERVISOR: Dr. Ali Emadi

PAGES: xix, 117

Abstract

The need for reductions in global greenhouse gas emissions, coupled with rising fuel prices, has motivated intense research in the area of hybrid and fully electric crafts for commercial applications in the aviation sector. This thesis explores implementation of Halbach arrays in high-speed radial flux machines (RFMs) and low-speed axial flux machines (AFMs) for aerospace applications. Highly accurate analytical equations are developed for quickly predicting the magnetic field in the latter (both for coreless and steel core stators) due to the complex three dimensional axial flux paths which make traditional finite element analysis time-consuming. Electromagnetic design and optimization of two aerospace machines that use Halbachs are detailed. The first is a ~14 kW AFM intended to replace an existing high lift motor RFM concept in NASA's Maxwell X57 all-electric plane. Two design variants are selected which achieve a 10 % increase in torque/power and a 10 % decrease in mass/volume, respectively. The second machine is a 20,000 RPM surface permanent magnet RFM capable of 150 kW peak power output that is intended as a proof-of-concept for the later development of a megawatt machine for a hybrid and/or all-electric aircraft.

Acknowledgements

I acknowledge that this research was undertaken, in part, thanks to funding from the Canada Research Chair in Transportation Electrification and Smart Mobility, Eaton Aerospace, and MITACS.

I acknowledge Chapter 2 to be taken from my own previously published conference paper [1]:

A. Forsyth, G. Pietrini, A. Callegaro and A. Emadi, "Generalized Analytical Solution for N-Segment Axial Flux Halbach Arrays," *2022 IEEE Transportation Electrification Conference & Expo (ITEC)*, Anaheim, CA, USA, 2022, pp. 391-396, doi: 10.1109/ITEC53557.2022.9814007.

I would like to thank my thesis advisor Dr. Ali Emadi for believing in me and enabling me to do what I love most. Thank you to Dr. Giorgio Pietrini for his support and guidance over the years, on this thesis and other publications too. Thank you to Dr. Berker Bilgin for his teachings on switched reluctance motors, and for providing me with many chances to apply what I have learned. Thank you to Cheryl Gies for being incredibly approachable, supportive, and helpful. Thank you to my colleagues and team members Srikanth Vasudevan Pillai, Dr. Mohamed Abdalmagid, Colleen Jenkins, Islam Zaher, Akshay Manikandan, Federico Duperly, Kenneth Noronha, Ethan Pereira, Samantha Jones-Jackson, Dikhsita Choudhary, Gayan Madusanka Amaradasa Watthewaduge, Mohammad Ehsan Abdollahi, Francisco Juarez-Leon and Alexander Allca-Pekarovic for making many of the projects I worked on possible during my time at McMaster. Thank you to my loving partner Maya for being there through it all, and lastly thank you to my mother whom I owe everything to and will forever be in my heart.

Table of Contents

List of Figures

List of Tables

List of Abbreviations and Symbols

Abbreviations:

AATT	Advanced Air Transportation Technologies
AC	Alternating Current
AFM	Axial Flux Machine
AWG	American Wire Gauge
CFD	Computational Fluid Dynamics
DC	Direct Current
FEA	Finite Element Analysis
FSCW	Fractional Slot Concentrated Winding
HGEP	Hybrid Gas Electric Propulsion
HGTF	Hybrid-Geared Turbo Fan
HLM	High Lift Motor
HTS	High Temperature Superconductor
ID	Inner Diameter
IR	Inner Radius
MSL	Mean Sea Level
NASA	North American Space Agency
NEMA	National Electrical Manufacturers Association
OD	Outer Diameter
OR	Outer Radius
RFM	Radial Flux Machine
SC	Schwarz-Christoffel
SUGAR-volt	Subsonic Ultra Green Aircraft Research
STARC-ABL	Single Aisle Turbo-Electric Aircraft with Aft Boundary Layer
WFS	Wound Field Synchronous
YASA	Yokeless And Segmented Armature

Symbols:

$\vec{A}$	Electric loading
a	Inner radius of annulus
A_{wire}	Area occupied by covered litz wire
$alpha$	Angle of each vertex
α_i	Ratio of average to peak flux density over one pole
α_s	Arc angle of radial magnet
A_{slot}	Slot cross-sectional area
$\vec{B}$	Magnetic loading
B	Flux density
b	Outer radius of annulus
B_{ag}	Flux density of airgap in real plane
B_{cc}	Flux density of airgap in concentric cylinders
B_{Ir}	Fundamental radial flux density
B_{mg}	Airgap magnetic flux density
B_{m0}	Airgap magnetic flux density on surface of magnets
B_r	Remanent flux density
β	angle
c	Radial distance from origin to a current sheet
$*$	Complex conjugate
C_{turns}	Coil turns
C_{wraps}	Coil wraps
C_{ratio}	Coil aspect ratio
C_{gap}	Coil gap
C_{height}	Coil height
C_{width}	Coil width
D_{Cu}	Nominal copper wire diameter
dF_x	Differential unit of force
D_i	Inner diameter

D_{ins}	Insulated wire diameter
dir	Direction
dL	Increment length
D_o, d_1, d_2	Outer diameter
dS	Differential unit of surface area
$\Delta\theta$	Angular difference
ΔX	Length of rectangle in Z-plane along real axis
ΔY	Length of rectangle in Z-plane along imaginary axis
f	Array containing complex vertex coordinates in Z-plane
H_{cc}	Field strength of airgap in concentric cylinders
I, i	Current excitation
I_d	Peak current excitation in d-axis
i_q	Peak current excitation in q-axis
j	Index
j	Imaginary variable $\sqrt{-1}$
K_{cw}	Coil fill factor
K_t	Torque constant
K_w	Winding factor
L	Axial length
L_a	Spatial period wavelength
L_d	D-axis phase inductance
L_q	Q-axis phase inductance
L_{mag}	Magnet thickness
L_{tot}	Active axial length
m	Index
m	Array containing complex position coordinates and strengths of current sheets in W-plane
M_{mag}	Magnet mass
μ_0	Permeability of vacuum

μ, μ_{mag}, μ_r	Relative permeability
λ_{pm}	Peak flux linkage due to permanent magnets
M	Magnetization
n	Index
n	Number of harmonics to consider in the infinite series
N	Number of discretizations
N	Number of turns per coil
N_{bar}, N_s	Number of stator bars
N_m	Magnet segment number
N_{seg}, n_m	Number of Halbach magnet segments per pole pair
N_1, N_2	Rotational speed
p	Polygon array
ϕ	angle
ϕ_f	Average magnetic airgap flux per pole
ϕ_m	Indexing term
pp	Pole pairs
ψ	Angular offset
ψ_{cc}	Magnetomotive force of airgap in concentric cylinders
q	Flow rate
r	Radius
r	Radial distance to each sampling point
r_i	Inner radius
R_r	Rotor yoke radius
R_m	Magnet radius
R_s	Stator bore yoke radius
r_o	Outer radius
s	Surface
s	Array containing complex current sheet coordinates in Z-plane
T	Torque

T_{avg}, T_e, $T_{avg.\ est.}$	Average electromagnetic torque
t	Index
θ	Theta, angle
θ	Angle between each sampling point and η-axis
θ_I	Angle between each current sheet and η-axis
w	Field sampling point complex coordinates in W-plane
v	Complex array of vertex coordinates in W-plane
ω	Rotational speed
z	Axial length
z	Array containing complex field sampling coordinates in Z-plane
ζ	Array of vertex coordinates in ζ-plane
Z_m	Indexing term

Declaration of Academic Achievement

I, Alexander Forsyth declare the work performed in this thesis “Use of Halbach Arrays in Axial and Radial Flux Permanent Magnet Machines for Aerospace Applications” to be that of my own. I confirm that the chapters listed contain work performed by me, with work performed by others referenced where applicable.

Chapter 1:	Introduction
Chapter 2:	Analytical Equations for Predicting Flux Density in Axial Flux Halbach Arrays
Chapter 3:	Analytical Equations for Predicting Flux Density in Steel Core Axial Flux Halbach Machines
Chapter 4:	Axial Flux Machine Design with Halbach Array for Electric Aircraft
Chapter 5:	Radial Flux Machine Design with Halbach Array for Electric Aircraft
Note:	Initial sizing and slot/pole combination of inner rotor and outer rotor machines performed by Dr. Giorgio Pietrini
Chapter 6:	Conclusions and Future Work
Appendix	

1. Introduction

1.1 Background and Motivation

The electrification of aircraft in the aviation sector has begun. The need for reductions in global greenhouse gas emissions, coupled with rising fuel prices, has motivated intense research in the area of hybrid and fully electric crafts for commercial applications. These vessels use electric machines (i.e., motors and generators) both for propulsion and energy conversion. They are often hypersensitive to weight, volume, and efficiency penalties incurred by today's electric machines, whose technological advancement has primarily been driven by less stringent applications like HVAC and automotive where cost is the primary constraint rather than performance. The electric aircraft of tomorrow demand new innovations in electric machine technology that push the limits of performance. To that end, topologies of electric machines capable of increasing machine power output with less material are an area of active exploration. This thesis will look at two such areas of improvement for electric machines in aerospace, which are: Halbach arrays for use in (relatively) low-speed axial flux machines (AFMs), and Halbach arrays for use in high-speed radial flux machines (RFMs).

1.1.1 Halbach Arrays

A Halbach array is a combination of permanent magnets arranged in specific repeating patterns so as to modify and focus the flux field of a magnetic device. In the case of an electric machine, a typical four-segment (per pole pair) Halbach array is composed of a main polarity magnet whose orientation is pointed parallel to the flow of flux through the machine's airgap, towards the stator. It has secondary magnets adjacent to the main on either side with magnetic polarities that are perpendicular to the main magnet, as seen in Figure 1. These magnets are used to focus and amplify the flux density over the main magnets, as evidenced by the much stronger flux density on the focused side (top side) in Figure 1. This creates a more sinusoidal electromotive force and lower cogging torque than would otherwise be achieved using conventional magnet arrangements [2]. Halbach arrays can be generated in a complete magnetic ring or as a

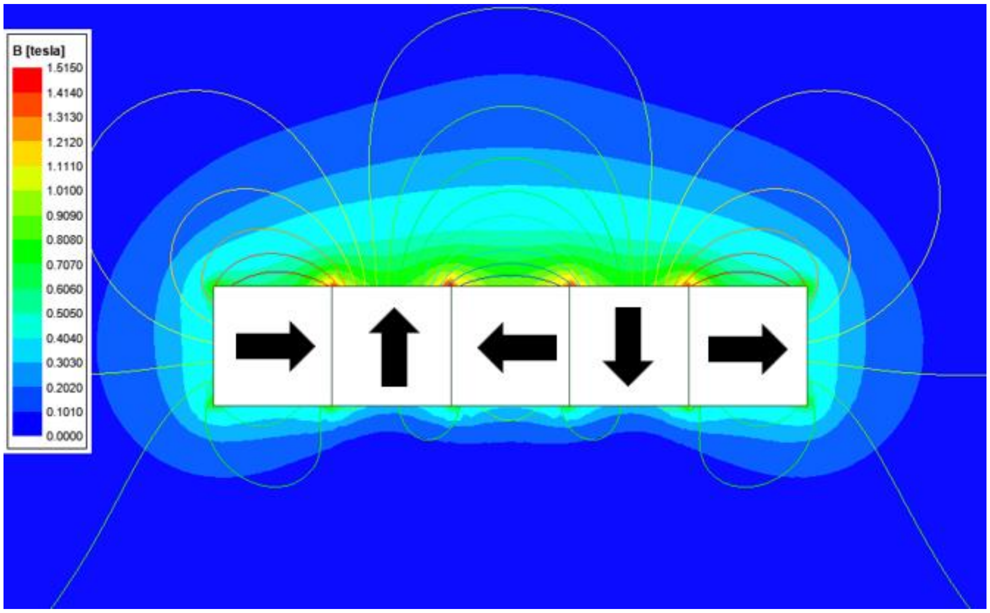

Figure 1. Two-segment Halbach array configuration, with magnet polarities (black), flux lines, and flux density visible

segmented array composed of individually magnetized pieces (i.e., Figure 1), the former being typically more difficult to realize, especially in large machine sizes. Thus, segmented Halbachs are more common [2]. Halbach arrays are almost unanimously implemented in surface permanent magnet machines rather than interior variants, which makes them an attractive choice for low-speed axial flux and high-speed radial flux topologies to maximize power output.

1.1.2 Radial Flux Machine Topologies

Radial flux machines get their name from the closed loop directional flow of flux between stator and rotor, as seen in Figure 2. Power in a rotating electric machine is the product of rotation (ω) and torque (T), which is produced by electromagnetic force acting in the airgap between stator and rotor. In the case of permanent magnet machines, electromagnetic force is the cross product of electric loading ($\vec{A}$) coming from the stator and magnetic loading ($\vec{B}$) coming from the rotor. These vectors are diagrammed for the airgap in a radial flux machine (represented as a cylinder) in Figure 3. Integrating force

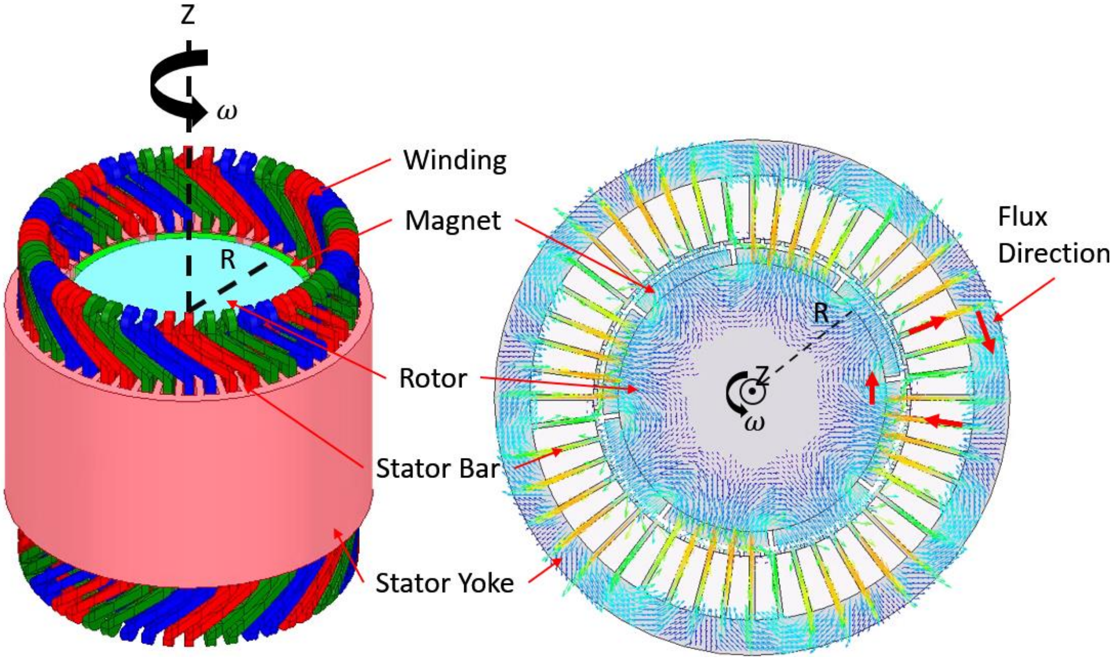

Figure 2. Radial flux machine, iso view (left), top view (right) with flux vectors visible

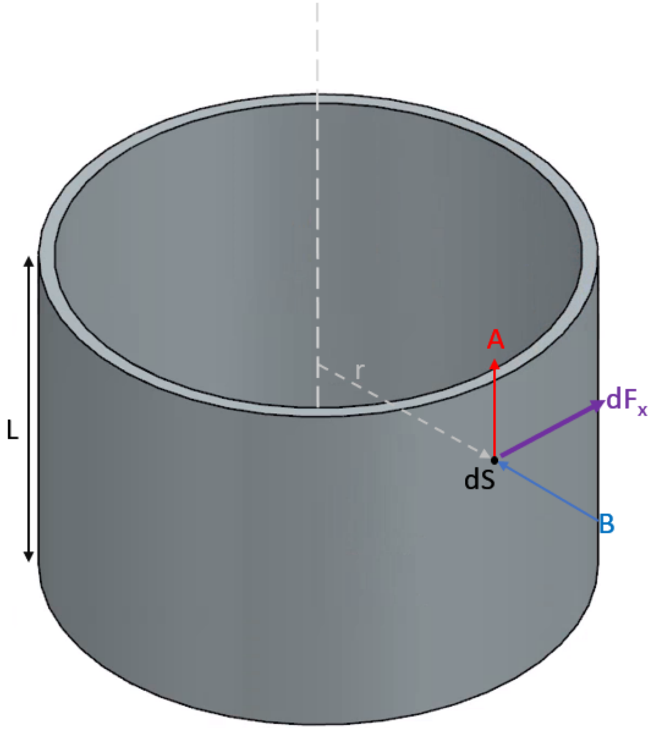

Figure 3. Radial flux machine force production

over the entire surface area, the electromagnetic torque for a radial flux machine can be expressed in Equation (1), where its linear relationship with length and parabolic relationship with radius is shown.

$$T_e = r^2 L \int_0^{2\pi} \vec{A}\vec{B} d\theta \tag{1}$$

There are two different rotor configurations that will be explored in this thesis, and they are inner rotor and outer rotor configurations, as diagrammed in Figure 4. Inner rotor RFMs are advantageous because they are inherently safe against rotor burst [3], have low rotor inertia which makes them ideal for high-speed maneuvering, and can implement salient pole configurations to produce wide constant power speed ranges [4]. Outer rotor RFMs, in contrast, are advantageous for their larger airgaps that can generate more torque for a given mass and volume. Their stator teeth, being on the outside, tend to be easier to wind [3] and can implement fly winding techniques for rapid manufacturing [5]. When magnets are used, the centrifugal force generated from rotation pushes the magnets outwards on outer rotor RFMs, rather than towards the stator, which eliminates the need for a retainer in the airgap [3] that would otherwise increases flux path reluctance. Their high inertia also helps to minimize torque ripple which provides for smoother operation at constant speeds [4].

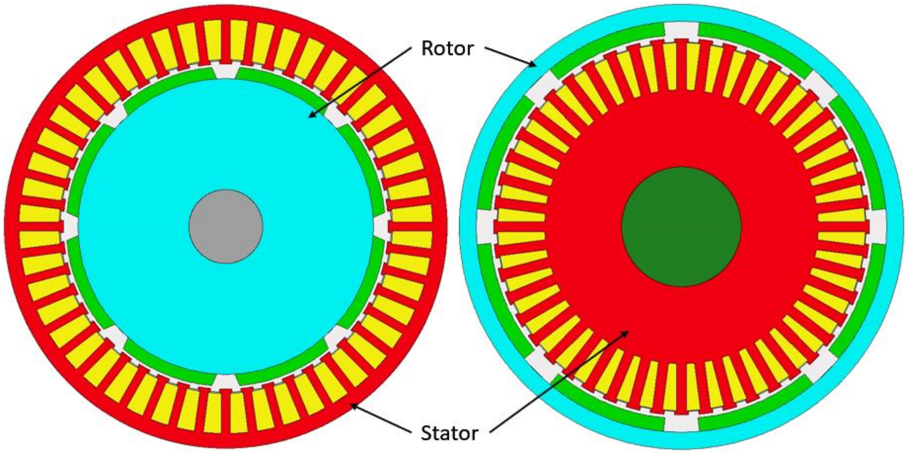

Figure 4. Top view, Inner rotor (left) and outer rotor (right) RFM configurations

1.1.3 Axial Flux Machine Topologies

Axial flux machines have components that are similar to most brushless electric machines. These include one or multiple stators, rotors, coil windings, bearings and a shaft. The main difference in this machine type is the direction of flux flow which travels axially along the machine's length. A diagram of this is presented in Figure 5. Axial flux machines have several benefits that make them an interesting choice for aerospace as compared to traditional RFMs. These include but are not limited to: Modularity [6], adjustable air gap [6], inherent centrifugal fan cooling design [6], high power-to-weight ratio [7], high efficiency [7], smaller volume and less active material use [6] for a similarly rated application.

A newer trend in the development of axial flux machines is the use of yokeless and segmented armature (YASA) designs. These machines make use of a double rotor topology with stator teeth that are physically detached from each other, having no stator back iron to complete a flux path between them as is normally the case. A diagram of this topology is displayed in Figure 6. The coils are wound axially along the stator teeth. Due

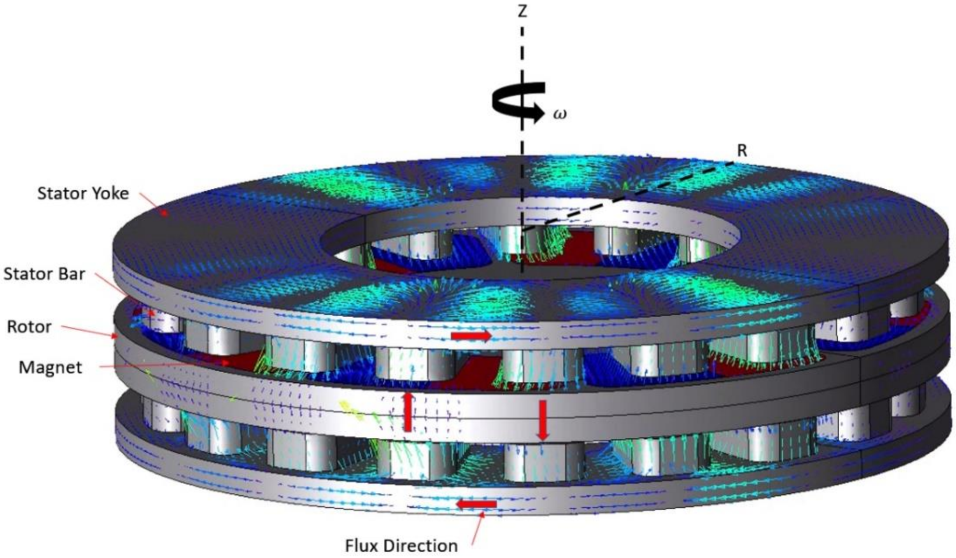

Figure 5. Single rotor, double stator axial flux machine, three-dimensional view with flux vectors visible

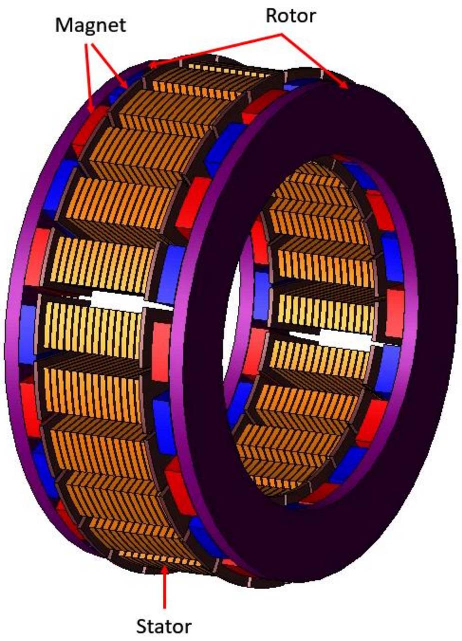

Figure 6. Typical YASA configuration

to their segmentation they can be pre-wound, prior to assembly, in order to achieve a higher packing factor. The YASA has a North-South (NS) configuration through which a North polarity magnet (red) on one rotor is synchronized with a South polarity (blue) on the second rotor, allowing flux to flow in a continuous line from one rotor, through the stator, to the next, before circling through the rotor’s back-iron to the adjacent magnet of opposite polarity. This design has the added benefit that the axial forces generated by the permanent magnets are balanced through the double rotors, reducing the axial forces that the bearings are required to withstand, which is usually high for single rotor, single stator variants. The stator segmentation also minimizes mutual inductance between phases and increases fault tolerance [8]. When the magnet arrangements are configured into a Halbach array, the YASA topology has a variation in which the rotor backiron can be eliminated entirely. As depicted in Figure 1, the weak side of the array has almost no flux at all, which greatly reduces the need for rotor back irons in electric machines typically used to support flux linkage. Removing the rotor back iron has the effect of reducing machine weight associated with a steel rotor, as well as reducing the cost and complexity of trying to use laminated steel for such a component. It can also improve the structural integrity of the AFM, as a magnetically permeable back iron (like silicon steel) is often glued into a rotor carrier of greater stiffness to prevent rotor bending, but paradoxically increases the risk of back iron adhesive delamination during operation.

Torque production in AFMs can be derived similarly to RFMs in Section 1.1.2. A diagram of the airgap in an AFM (represented as an annulus) is displayed Figure 7. Assuming $\vec{A}$ and $\vec{B}$ are largely independent of radius and again integrating over the entire rotor surface area, the electromagnetic torque for an axial flux machine can be expressed as shown in Equation (2),

$$T_e = \frac{(r_o^3 - r_i^3)}{3}\int_0^{2\pi} \vec{A}\vec{B}\,d\theta \tag{2}$$

Where r_o and r_i are the outer and inner radius of the annulus, respectively. Here the cubic relationship between radii and torque is demonstrated. It can also be concluded that AFM torque production is independent of machine length (at least in theory), and benefits more from a high radius-to-length ratio than radial flux machines do, which varies with the square of the radius. This often leads to very flat, wide, pancake-like axial flux machines that are designed to maximize power through high torque at low speeds, since the

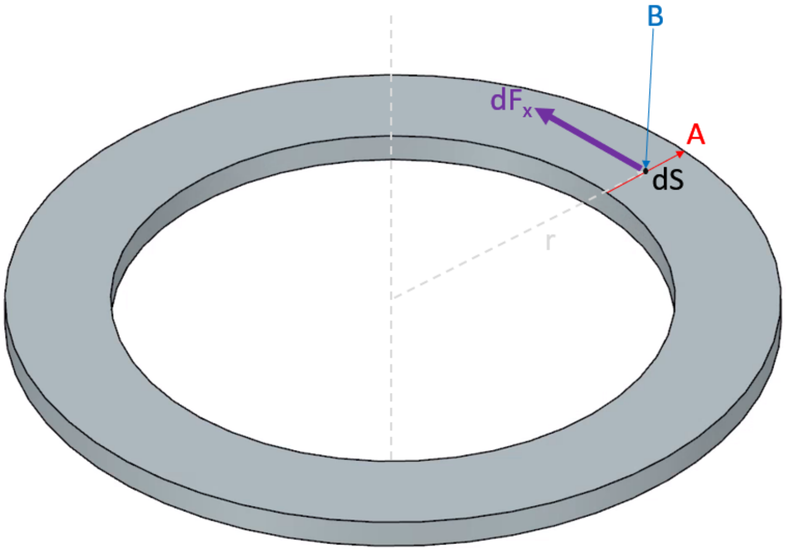

Figure 7. Axial flux machine force production

centrifugal and bending forces acting on such a rotor increase with diameter. Radial flux machines, in contrast, can benefit from increased axial length and smaller diameters. This often leads to long and thin RFMs that are designed to maximize power at high speeds made possible from reduced centrifugal stress. This is most evident in the automotive industry, which is trending towards higher and higher speed RFMs for use in powertrains as it is being increasingly found that there are mass, volume and cost savings to be had at high rotations [9]. The aerospace sector is poised to benefit from these configurations as well, both for low speed direct-drive propulsion applications, and high-speed turbine-generator applications, which will be presented in the chapters to come.

1.2 Thesis Outline and Contributions

The contributions of this thesis revolve around investigating the use of Halbach arrays in electric machines for aerospace applications, as highlighted in chapter 1. Two machines will be presented as design studies for demonstrating the application of Halbach arrays in axial flux and radial flux topologies. The first design is a ~14 kW axial flux motor intended to replace a pre-existing high lift radial flux machine used by NASA in their Maxwell X-57 all-electric plane project. Equations and methodologies are developed and presented for use in predicting the electromagnetic flux field produced by axial flux Halbach arrays for both air core (chapter 2) and steel core stator machines (chapter 3), which is something that normally requires three-dimensional finite element analysis to complete. Chapter 4 demonstrates how the steel core stator equations can be used to analyze torque performance in the high lift motor axial flux redesign. The second machine design study, presented in chapter 5, is a 150 kW high-speed radial flux machine designed to be used as proof-of-concept prior developing a scaled-up megawatt-class prototype (not covered herein). Coupled electromagnetic and thermal analysis of outer rotor and inner rotor topology design variants are compared. Different Halbach configurations for the rotor of the chosen design are also analyzed. The final Chapter 6 summarizes the preceding chapters, specifically the development of analytical equations for axial flux machine Halbachs and the design of two electric machines that use Halbachs intended for aerospace applications. Directions for future work are discussed.

2. Analytical Equations for Predicting Flux Density in Axial Flux Halbach Arrays

2.1 Pre-existing solutions

With the rising popularity of electric vehicles and the ever-increasing trend towards miniaturization of their components, axial flux permanent magnet machines are seen as an enticing method of improving torque density within these powertrains [8], [10]–[14]. Cost permitting, permanent magnet Halbach arrays are the method of choice to increase a surface permanent magnet machine's power rating further, while also allowing for the elimination of rotor back irons which represent added weight, complexity, and core loss [2], [15]. Machines or devices that make use of axial flux Halbach magnetic arrays typically require complex 3D models for accurate analysis, which can be much more time and resource intensive than 2D models, particularly for permanent magnet machines [16]. NASA researcher William Thompson originally developed analytical equations for a 4-segment (per pole-pair) axial flux cylindrical Halbach array for use in bearings [17]. While these equations are applicable to numerous applications, Halbach arrays employed in today's motors routinely have higher levels of segmentation designed to approximate the ideal sinusoidal array more closely. Since then, analytical solutions have been proposed by Li and Bird [18] for an 8-segment axial flux Halbach array used in magnetic couplings. Their solution first solved the problem at the magnet mid-radius where the radial flux density component is assumed to be zero, then uses the result as a source term in a magnetic charge disc model. This was done in order to avoid the double integration double summation terms used in Thompson's approach. They were able to evaluate the radial integration term and reduce their equations down to a single integration along the circumferential direction. But this method does not easily extend to Halbach segmentations other than the 8 segments used. Each type of array likely requires its own unique solution derived beforehand, with the radial integration term not necessarily disappearing for all types. Thus, there is no obvious way to extend it to N-segments. With Thompson's set of equations, there is. This chapter will extend Thompson's equations so that they can be used in arrays of N-segments, with the intent that they be used as buildings blocks for further analysis of electromagnetic assemblies, such as EV traction machines, particularly the coreless variety which these equations are bested suited for.

2.2 Proposed Method

2.2.1 Analytical Equations

The prototypical 4-segment axial flux cylindrical Halbach array can be seen in Figure 8, along with relevant variable notation used throughout this paper.

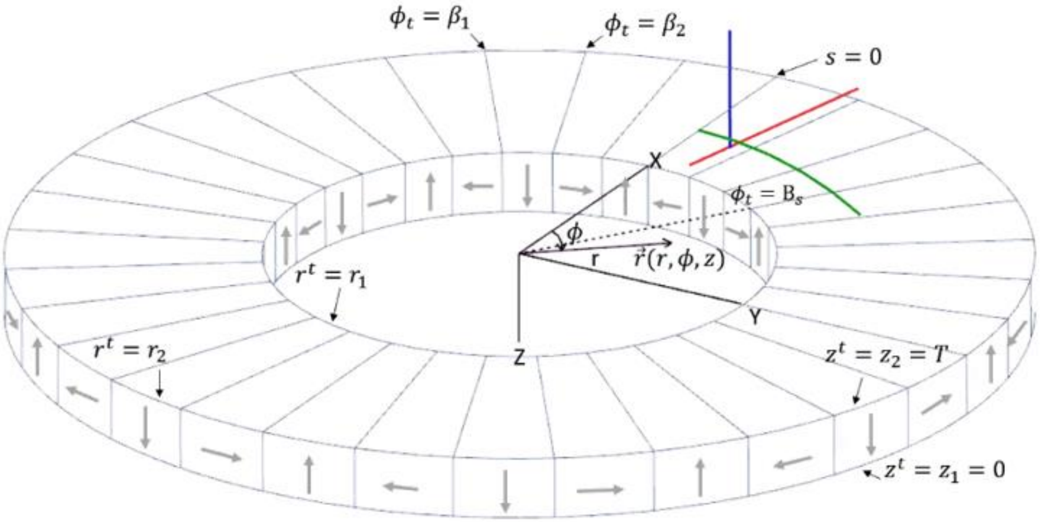

Figure 8 General diagram of axial Halbach array

Positive quantities are assumed along the indicated x-axis, z-axis, and counterclockwise in the ϕ-direction. The derivation of the equations used to characterize the flux density field initially proceed identical to those developed in Thompson's 4-segment array [17]. Readers interested in a detailed explanation of this should refer to the original work. The final equations presented here are with explanation only towards the modifications made to the original equations which makes analysis of other segmentation configurations possible. The equations for radial, tangential and axial components of Halbach array flux density, at any point in space, for any segmentation can be found in equations (3) – (5).

$$B_r(\vec{r}) = \frac{\mu_0 M}{4\pi}\sum_{n=0}^{N_m-1}\sum_{j=1}^{2}(-1)^j \left[\begin{array}{c} Z_m\left[\int_{z_1}^{z_2}\int_{\beta_1}^{\beta_2}\frac{(z-z')\,cos(\phi-\phi')}{|\,\vec{r}-\vec{r}'\,|^3}r'd\phi'dz'\right]_{r'=r_j} + \\ Z_m\left[\int_{z_1}^{z_2}\int_{r_1}^{r_2}\frac{(z-z')\,sin(\phi-\phi')}{|\,\vec{r}-\vec{r}'\,|^3}dr'dz'\right]_{\phi'=\beta_j} + \\ \phi_m\left[\int_{z_1}^{z_2}\int_{\beta_1}^{\beta_2}\frac{sin(\phi-\phi')}{|\,\vec{r}-\vec{r}'\,|^3}r'^2d\phi'dz'\right]_{r'=r_j} - \\ \phi_m\left[\int_{r_1}^{r_2}\int_{\beta_1}^{\beta_2}\frac{(z-z')sin(\phi-\phi')}{|\,\vec{r}-\vec{r}'\,|^3}r'd\phi'dr'\right]_{z'=z_j} \end{array}\right] \tag{3}$$

$$B_\phi(\vec{r}) = \frac{\mu_0 M}{4\pi}\sum_{n=0}^{N_m-1}\sum_{j=1}^{2}(-1)^{j+1} \left[\begin{array}{c} Z_m\left[\int_{z_1}^{z_2}\int_{\beta_1}^{\beta_2}\frac{(z-z')\,sin(\phi-\phi')}{|\,\vec{r}-\vec{r}'\,|^3}r'd\phi'dz'\right]_{r'=r_j} - \\ Z_m\left[\int_{z_1}^{z_2}\int_{r_1}^{r_2}\frac{(z-z')\,cos(\phi-\phi')}{|\,\vec{r}-\vec{r}'\,|^3}dr'dz'\right]_{\phi'=\beta_j} + \\ \phi_m\left[\int_{z_1}^{z_2}\int_{\beta_1}^{\beta_2}\frac{(z-z')cos(\phi-\phi')}{|\,\vec{r}-\vec{r}'\,|^3}r'd\phi'dr'\right]_{r'=r_j} + \\ \phi_m\left[\int_{r_1}^{r_2}\int_{\beta_1}^{\beta_2}\frac{(r-r'\,cos(\phi-\phi'))}{|\,\vec{r}-\vec{r}'\,|^3}r'd\phi'dz'\right]_{z'=z_j} \end{array}\right] \tag{4}$$

$$B_z(\vec{r}) = \frac{\mu_0 M}{4\pi}\sum_{n=0}^{N_m-1}\sum_{j=1}^{2}(-1)^{j+1} \left[\begin{array}{c} Z_m\left[\int_{z_1}^{z_2}\int_{\beta_1}^{\beta_2}\frac{rcos(\phi-\phi')-r'}{|\,\vec{r}-\vec{r}'\,|^3}r'd\phi'dz'\right]_{r'=r_j} - \\ Z_m\left[\int_{z_1}^{z_2}\int_{r_1}^{r_2}\frac{r\,sin(\phi-\phi')}{|\,\vec{r}-\vec{r}'\,|^3}dr'dz'\right]_{\phi'=\beta_j} + \\ \phi_m\left[\int_{r_1}^{r_2}\int_{\beta_1}^{\beta_2}\frac{rsin(\phi-\phi')}{|\,\vec{r}-\vec{r}'\,|^3}r'd\phi'dr'\right]_{z'=z_j} + \end{array}\right] \tag{5}$$

The major improvement to Thompson's equations set, implemented to allow for the analysis of N-segment Halbach arrays, is the introduction of superposition of the tangential and axial *B*-fields that are found simultaneously in transitional magnets (i.e., those found between magnets of purely tangential or axial magnetic orientation) of Halbach arrays with segmentations greater than 4 per pole pair. Thompson's 4-segment array has all magnets possessing pure tangential or axial orientations. Thus, he was able to account for the changing orientation of each magnet with a $(-1)^n$ term, which has since been removed, and instead replaced with more robust indexing terms Z_m and ϕ_m defined in equations (6) and (7).

$$Z_m = sin\left(mod\left(n, N_{seg}\right)\frac{2\pi}{N_{seg}} * dir + \psi\right) \tag{6}$$

$$\phi_m = cos\left(mod\left(n, N_{seg}\right)\frac{2\pi}{N_{seg}} * dir + \psi\right) \tag{7}$$

Where N_{seg} refers to the number of Halbach segments in one pole pair, *dir* refers to Halbach direction (+1 clockwise, –1 counterclockwise), that defines which side of the array has an amplified field, and ψ is the angular offset of the zeroth magnet's magnetic orientation, as registered from the xy-plane, with counterclockwise being positive. The tangential integration bounds were also altered to reflect the superposition analysis, as shown by equations (8) – (10).

$$\beta_1 = \frac{2(n+1)\pi}{N_m} \tag{8}$$

$$\beta_2 = \frac{2n\pi}{N_m} \tag{9}$$

$$\beta_j = \frac{2\pi(n+j-1)}{N_m} \tag{10}$$

The last modification to be mentioned is that the summation now begins and ends at the edge of the magnet. This makes for an altogether cleaner and less confusing set of equations, particularly regarding the summation bounds, rather than starting and ending on a magnet center, as was the case with the original equations.

2.2.2 Test Cases

Three Halbach arrays have been used to validate the new model. The first is the original 4-segment per pole-pair Halbach developed by Thompson [17] and is used for comparison. The second is a general 6-segment per pole-pair Halbach. The third is a general 8-segment per pole-pair Halbach, displayed in Figure 9. Their specifications are listed in Table I.

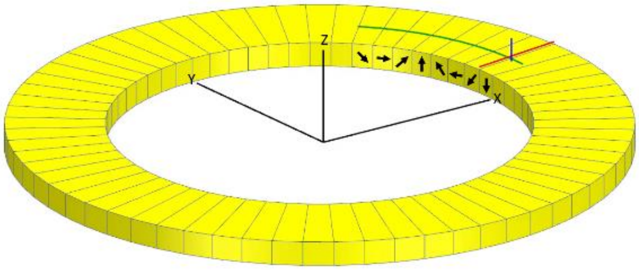

Figure 9. General 8-segment Halbach array

Table I. Halbach array specifications, 4, 6 and 8 segments

Specifications	Symbol	4-Segment	6-Segment	8-Segment
Number of magnets	N_m	32	60	64
Number of poles	-	16	20	16
Magnet grade	-	N55	N40	N48H
Amplified direction	-	–Z	+Z	+Z
Magnet IR	r_1	25.4 mm	53mm	85 mm
Magnet OR	r_2	50.8 mm	67mm	125 mm
Magnet thickness	z_2	6.35 mm	4.5mm	10 mm

A sensitivity analysis will be performed on the 8-segment Halbach to study the effects of changing magnet thickness, segmentation, inner radius and outer radius on flux density.

2.2.3 Tools Used

Equations (3) – (5) are implemented in MATLAB for ease of integration into larger MATLAB/Simulink models of electric machines and other magnetic devices as well as complex systems such as a full vehicle, that will be the subject of future work. The models are finally verified using Ansys magnetostatic 3D finite element analysis (FEA).

2.3 Results

2.3.1 Validation

The results of the 4-segment Halbach array are presented in Figure 10 through Figure 12. They are taken below the z-axis, shown in Figure 8, which corresponds to the array's amplified field side. Results taken from [17] are shown in blue.

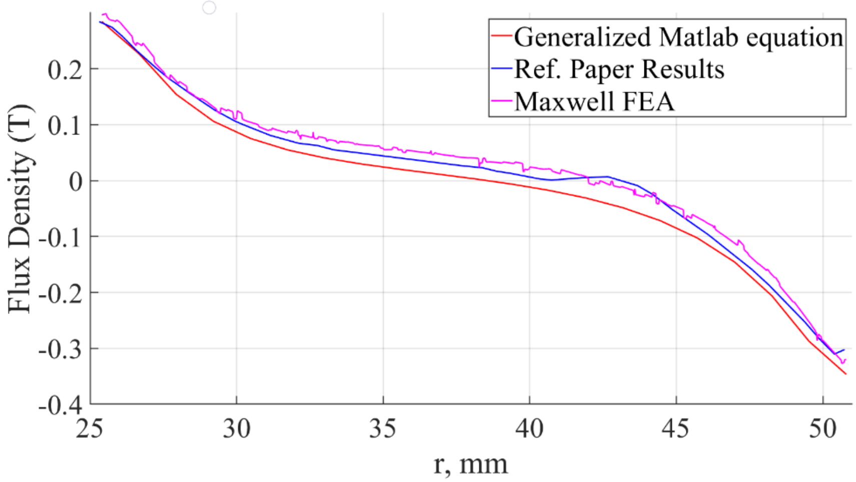

Figure 10. 4-segment Halbach array, radial flux density radial dependency comparison

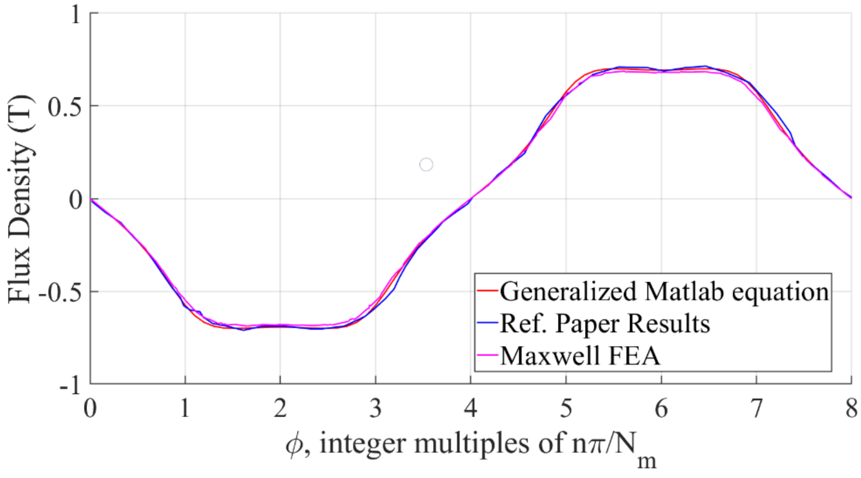

Figure 11. 4-segment Halbach array, tangential flux density tangential dependency comparison

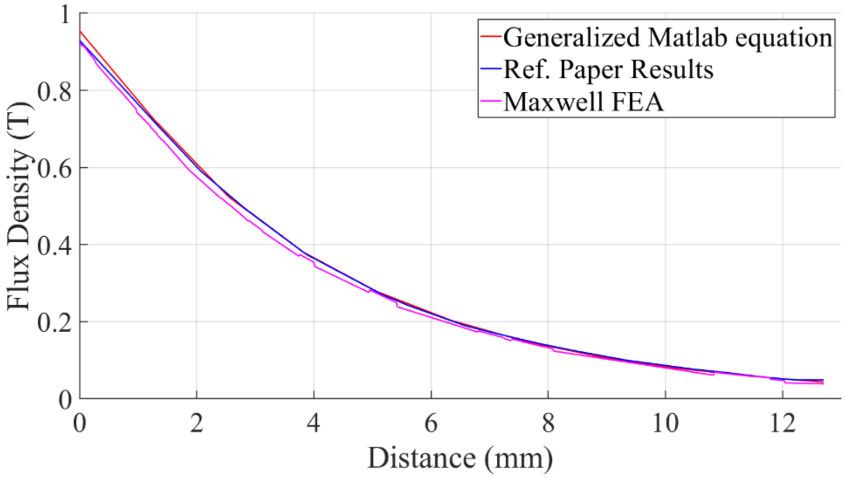

Figure 12. 4-segment Halbach array, axial flux density axial dependency, comparison

Figure 10 plots the radial flux density component sampled radially (Figure 8 red line) at z = –1.27 mm (–0.05 in.) with $\theta = \pi/N_m$. Figure 11 plots the tangential flux density component sampled circumferentially (Figure 8 green line) at r = 33 mm (1.3 in) and z = –1.27 mm (–0.05 in.). Figure 12 plots the axial flux component sampled axially (Figure 8 blue line) at r = 33.45 mm (1.317 in.) and $\phi = 0.5\pi/N_m$. Note that Figure 12 x-axis units are magnitude only. The measurements are taken along the negative z-axis. Results of the 6 and 8-segment Halbach array are presented in Figure 13 through Figure 15.

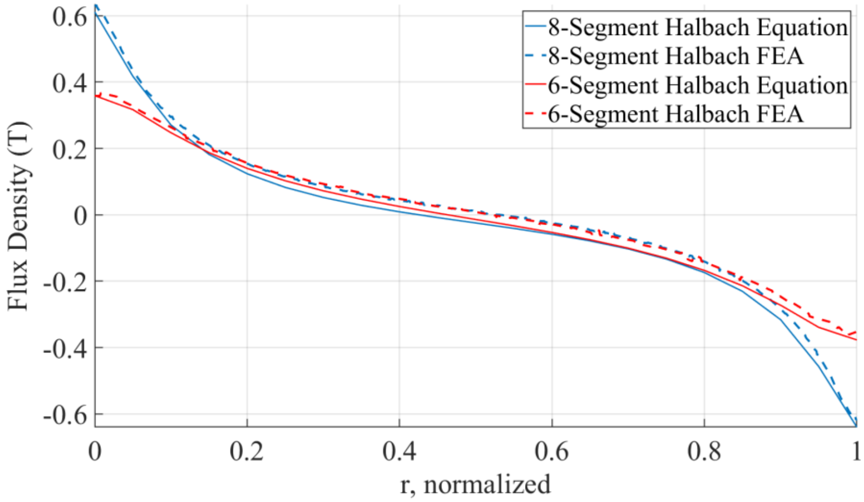

Figure 13. General 6 and 8-segment Halbach array, radial flux density radial dependency comparison

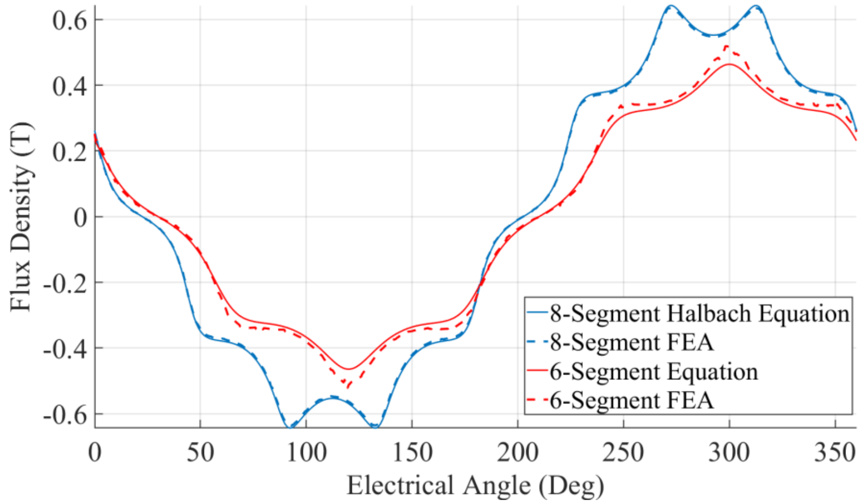

Figure 14. General 6 and 8-segment Halbach array, tangential flux density

Figure 13 plots the radial flux density component sampled radially (Figure 9 red line) at z = 11 mm, or 1 mm above the array's amplified field side with $\theta = \pi/N_m$. The x-axis is normalized from the inner to outer radius of the magnet, to account for the difference in diameters used between the two arrays. Figure 14 plots the tangential flux density component sampled circumferentially (Figure 9 green line) at r = 100 mm and z = 11 mm.

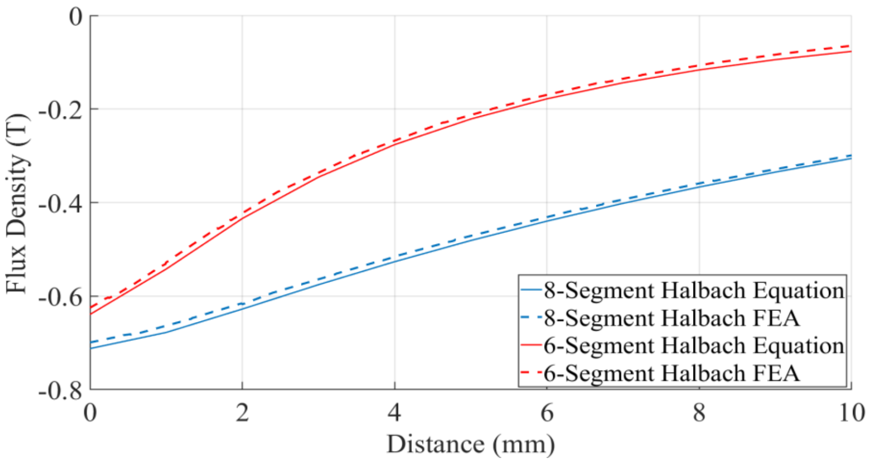

Figure 15. General 6 and 8-segment Halbach array, axial flux density axial dependency, generalized comparison

Figure 15 plots the axial flux component sampled axially (Figure 9 blue line) at $\phi = 0.5\pi/N_m$, r = 57 mm and r = 100 mm for the 6-segment and 8-segment array, respectively. Table II presents a summarized comparison of the accuracy for the three magnet arrays for each of the flux density components shown.

Table II. Summary comparison of 4, 6 and 8-segment analytical solutions to FEA

	4-segment Halbach array		6-segment Halbach array		8-segment Halbach array	
	Average Delta (mT)	Max Delta (mT)	Average Delta (mT)	Max Delta (mT)	Average Delta (mT)	Max Delta (mT)
Radial flux density, radial dependency	3.21	46.0	20.8	35.8	31.0	44.5
Tangential flux density, tangential dependency	1.36	37.9	16.6	57.5	4.9	11
Axial flux density, axial dependency	1.34	37.1	16.2	11.0	10.0	14.4

2.3.2 Sensitivity Analysis

A sensitivity analysis is performed on the 8-segment Halbach configuration presented in Figure 9 and Table I where one geometric property is varied while the rest are held constant. Note that throughout this analysis, as the magnet shapes change, the measurement points must move accordingly to stay at a constant position relative to those used in Section 2.2.2. Radial and tangential flux densities are consistently sampled 1 mm above the magnet surface.

The first analysis performed varies the segmentation of the magnet from 4 segments to 12 segments, per pole pair. The results are presented in Figure 16 through Figure 18. Figure 19 is a spatial Fast Fourier Transform (FFT) demonstrating the effect of increased segmentation on Halbach flux density harmonics, using data shown in Figure 17.

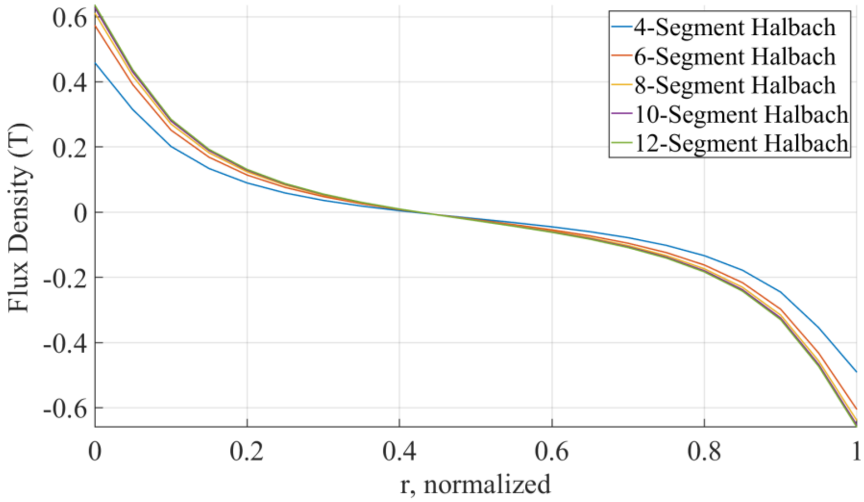

Figure 16. Radial flux density radial dependency comparison of various segmentation Halbachs

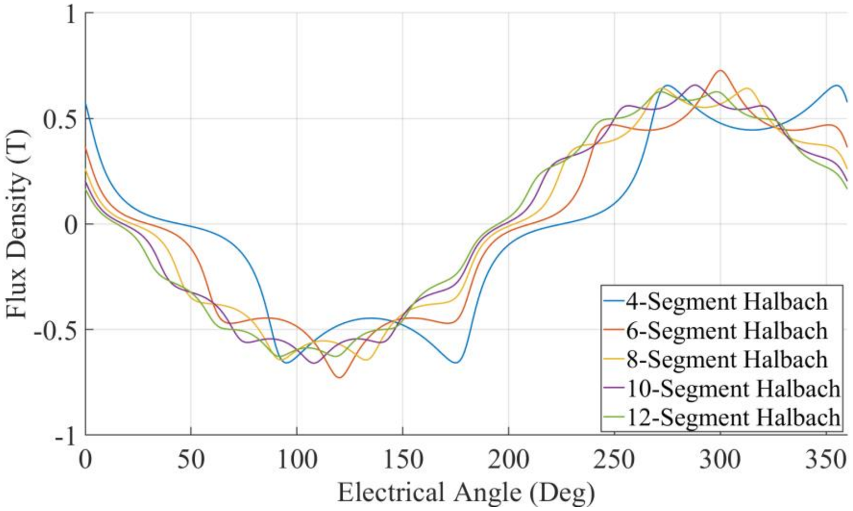

Figure 17. Tangential flux density tangential dependency comparison of various segmentation Halbachs

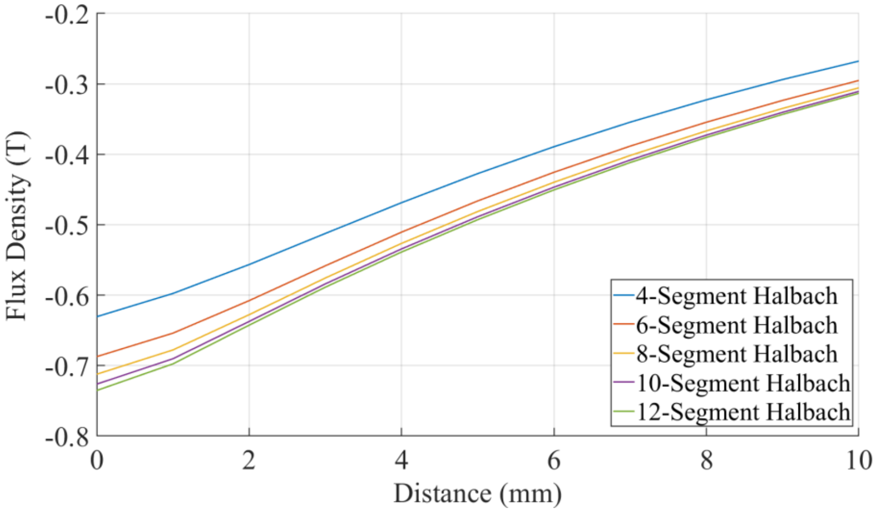

Figure 18. Axial flux density axial dependency comparison of various segmentation Halbachs

While the peak magnitudes of the waveform in Figure 17 are all roughly the same, the lower segments have significant higher order harmonics, whereas the fundamental component of flux density increases with greater segmentation. Peak radial and axial flux density also increase with segmentation.

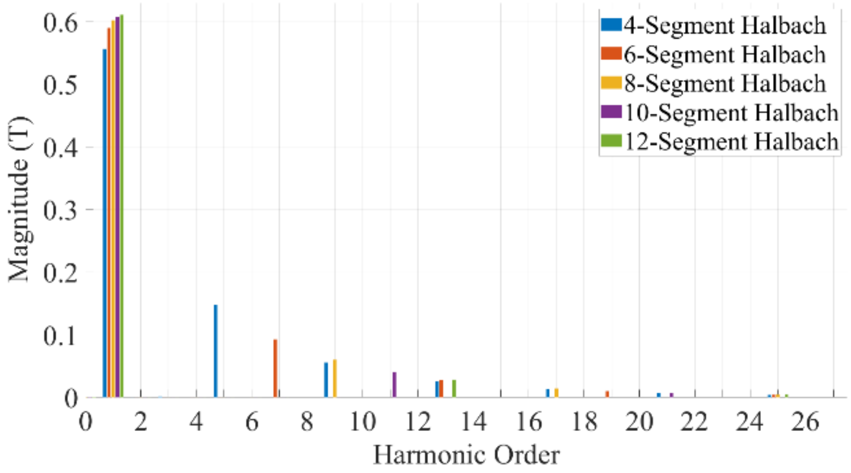

Figure 19. Spatial FFT of tangential flux density, tangential dependency

For all three components, flux density plateaus with increasing segmentation. Figure 20 through Figure 22 display the results of the magnet axial thickness sensitivity analysis. Peak flux density values increase before plateauing out.

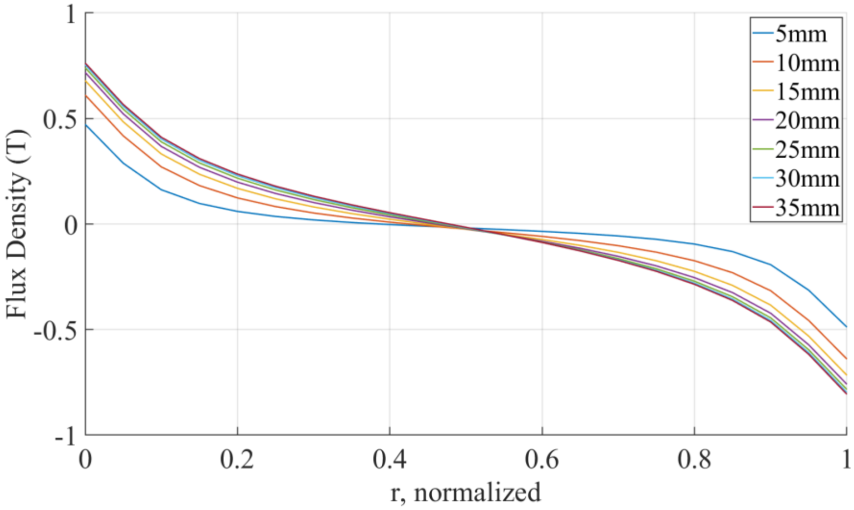

Figure 20. Radial flux density radial dependency comparison of various thickness Halbachs

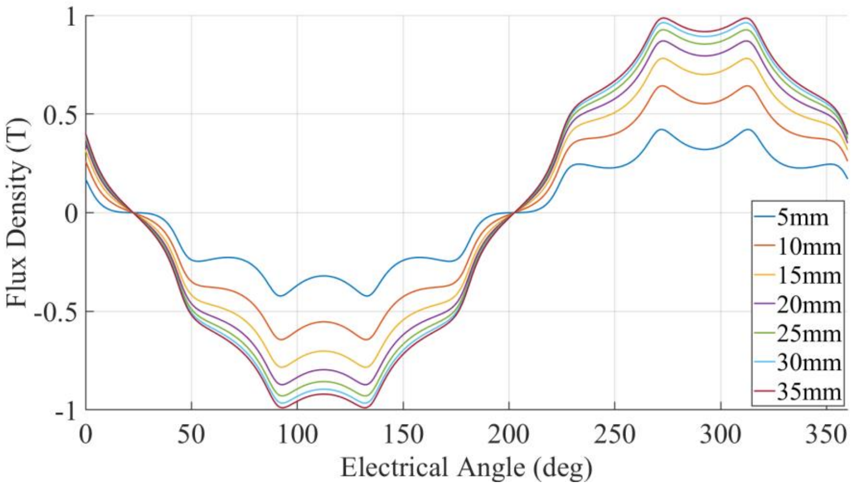

Figure 21. Tangential flux density tangential dependency comparison of various thickness Halbachs

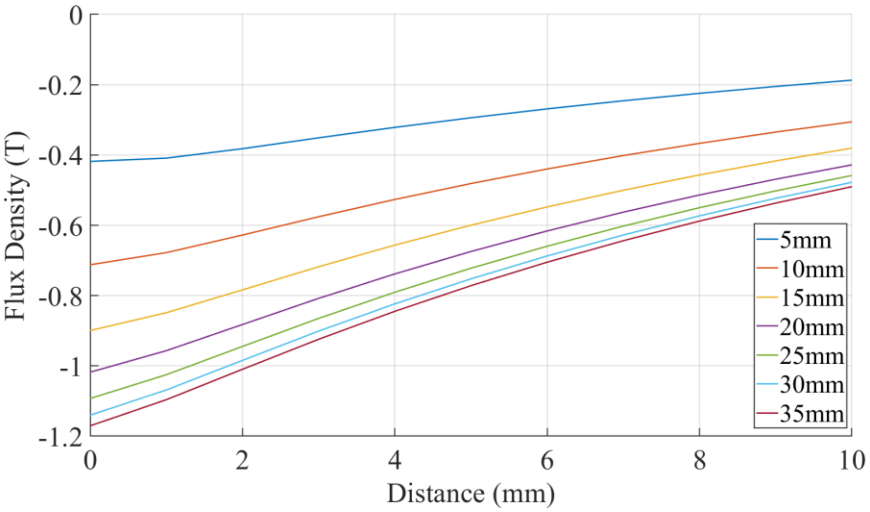

Figure 22. Axial flux density axial dependency comparison of various thickness Halbachs

Figure 23 through Figure 25 display the results of the magnet inner radius sensitivity analysis. Peak flux density values tend to improve with larger inner radii sizes before plateauing out.

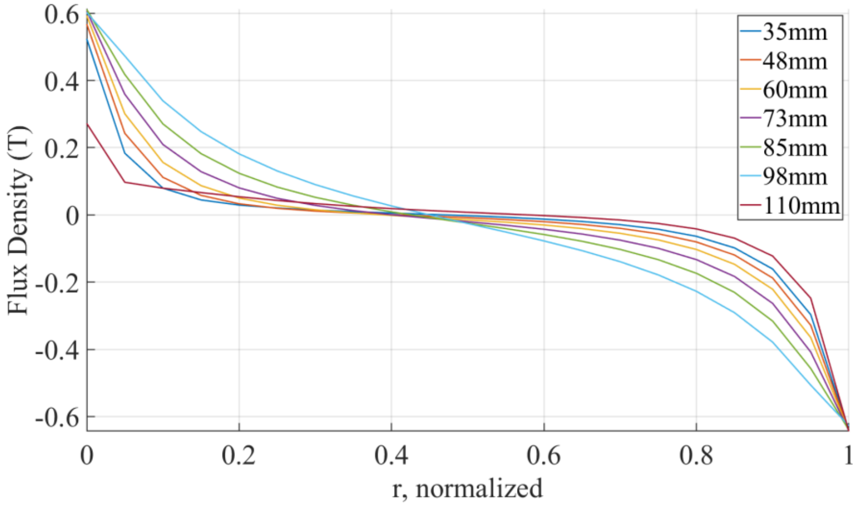

Figure 23. Radial flux density radial dependency comparison of varying inner radius Halbachs

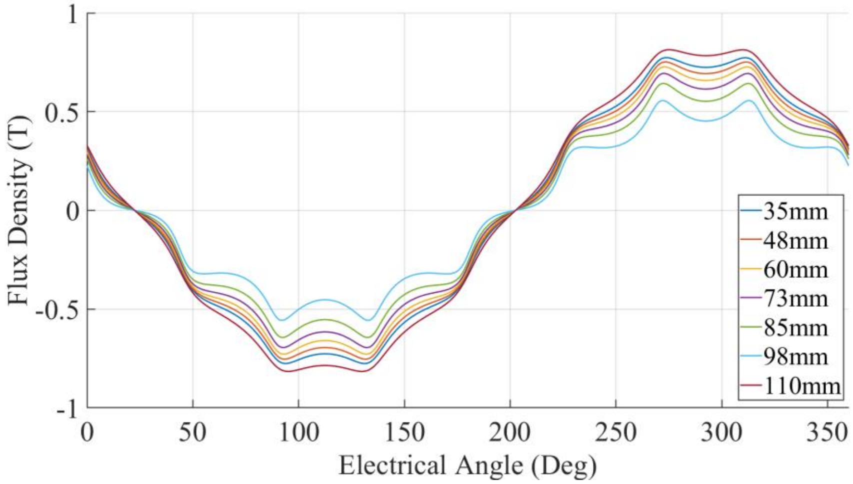

Figure 24. Tangential flux density tangential dependency of varying inner radius Halbachs

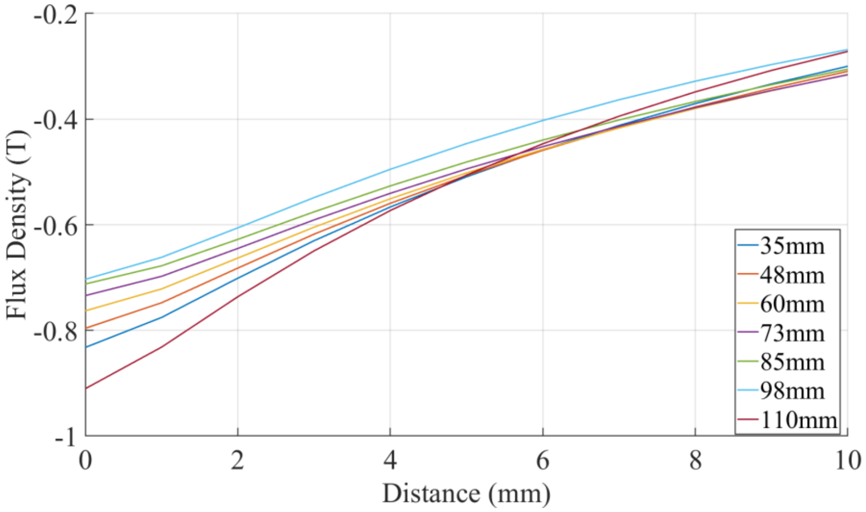

Figure 25. Axial flux density axial dependency of varying inner radius Halbachs

Figure 26 through Figure 28 display the results of the magnet outer radius sensitivity analysis. Peak tangential flux density values tend to improve with larger outer radii sizes before plateauing out. Axial flux density shows the opposite trend. Radial flux density becomes more curvilinear with increasing radii.

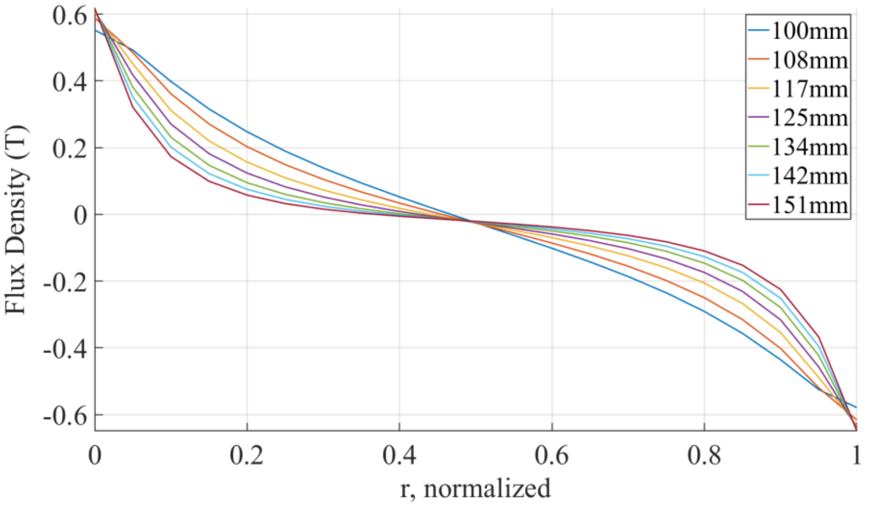

Figure 26. Radial flux density radial dependency comparison of various outer radius Halbachs

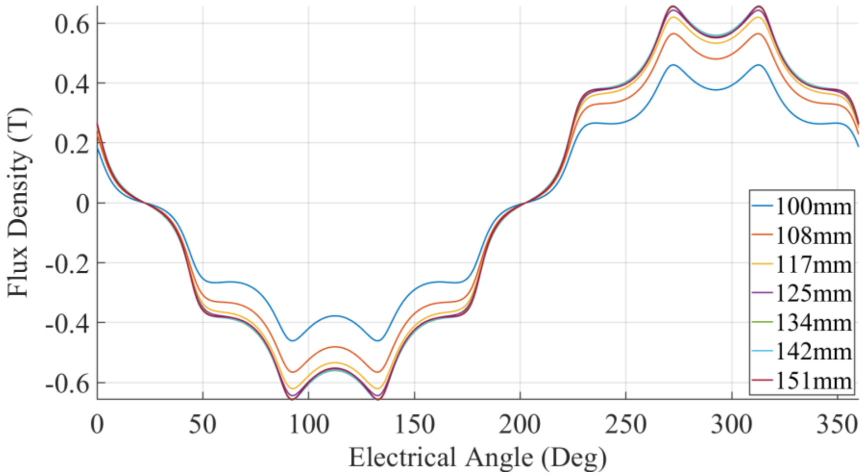

Figure 27. Tangential flux density tangential dependency comparison of various outer radius Halbachs

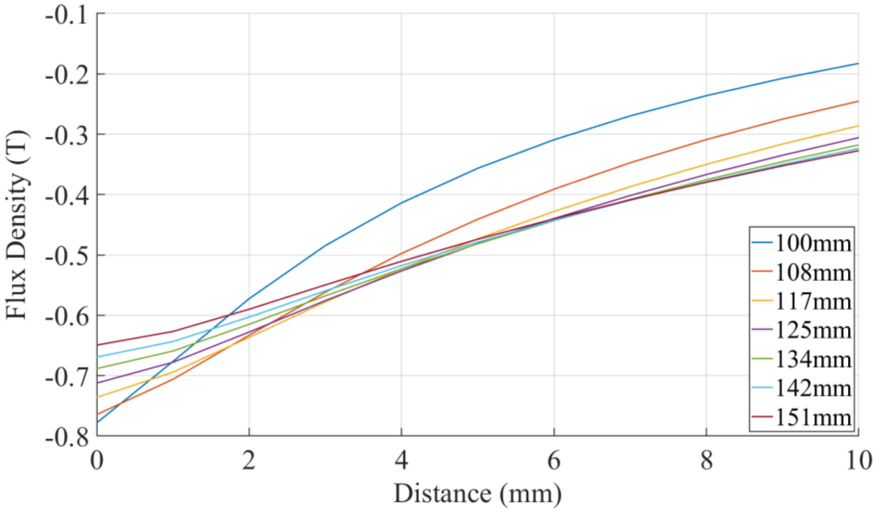

Figure 28. Axial flux density axial dependency comparison of various outer radius Halbachs

2.4 Summary

An analytical solution to predict the flux density field in an axial flux cylindrical Halbach array of any size and segmentation has been demonstrated. The results of 4, 6 and 8-segment per pole pair Halbach arrays suggest good accuracy when compared to FEA. These equations can be useful for development of more complicated electromagnetic assemblies involving Halbach arrays, for example in electric vehicle motors. A sensitivity analysis was conducted on the 8-segment Halbach demonstrating a general increase in peak flux density from increasing segmentation, thickness, and inner radius of the magnets. Increasing the outer radius strengthened the tangential component but weakened the axial component. In all cases, a general plateauing effect was observed where further increases to the dimensions yielded negligible results.

3. Analytical Equations for Predicting Flux Density in Steel Core Axial Flux Halbach Machines

Axial flux machines have challenges inherent to their design that make quick analysis difficult. Some of the most prominent of these are edge and curvature effects that affect flux density distributions at the machine's inner (ID) and outer diameters (OD). Edge effects are due to the machine's pole pitch which varies along its radius. Curvature effects are due to flux fringing. The best and most accurate method of addressing these is through 3D FEA, which is typically the most time consuming. 2D models can speed up the process but, unlike radial flux machines which are identical along their third axis, axial flux machines must employ correction factors for edge and curvature effects. This is the case for mean-radius models which take a slice of the machine halfway between the inner and outer diameter. Multi-slice models that take slices at multiple points along the machine radius can also be employed and will generally account for edge and curvature effects better [12]. Multi-slice machines may fail to consider the radial migration of flux between the sliced segments in the event of localized saturation effects, but the impact of this effect is usually low, and they are a good compromise between accuracy and computational burden. Multi-sliced axial flux models are also advantageous for analytical analysis because the solutions to the scalar magnetic potential second order ordinary differential equations which characterizes the magnetic fields are 2D, which have closed form solutions that take much less computation to evaluate than their 3D counterparts, which usually require Bessel functions to solve. These 2D analytical equations can be even faster to compute than multi-sliced 2D FEA models, and yield solution times that are appropriate for geometric customization and optimization.

3.1 Schwarz-Christoffel Mapping

Chapter 2 presented an analytical solution for cylindrical Halbachs that could be used in coreless axial flux motors. The permeability being near constant everywhere greatly simplified the derivation of a system of equations to model the complex 3D flux field. For Halbach motors with permeable steel stators there are many different boundary conditions in the machine where the permeability changes (i.e., rotor, airgap, stator), and the additional effect of stator slotting tends to distort the flux field in ways that require advanced methodologies to solve analytically. Schwarz-Christoffel (SC) mapping is one such analytical approach that has been employed successfully in radial flux machines [19]–[36] but to a limited extent in axial flux machines [37], [38]. In essence, Schwarz-Christoffel mapping for use in electric machines involves mapping vertices of complex machine geometry from one domain to a much simpler one, where readily available analytical solutions to the magnetic field exist, then transforming it back to the original domain. A relatively modern treatise on the mechanisms of the century-old Schwarz-Christoffel mapping technique was written by Driscoll and Trefethen, and can be found in [24]. What follows is a summarized description of how this is accomplished for an axial flux machine with a Halbach array. Further details on how SC mapping can be applied to electric machines more generally has already been described thoroughly elsewhere and the interested reader is recommended to [28].

3.2 W-Plane Geometry Creation

The first stage is to develop a 2D cross-section of the 3-dimensional geometry at a given radius, as seen in the example of Figure 29. This can be done using mathematical equations which characterize the geometry or through use of cad software like Siemens NX, which can extract features projected on a curve, then unwrapping the surface. From here, the vertices of the permeable steel in the 2D cross-section are extracted from the

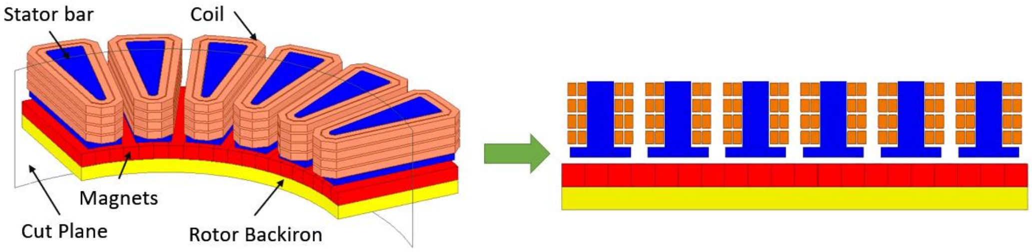

Figure 29. Anti-periodic 3D AFM model (left) to 2D model (right) example

design and converted to a closed polygon using the MATLAB SC mapping toolbox by issuing the *p = polygon(v)* command where *v* is an array of the stator and rotor geometry in complex coordinates, as seen in Figure 30. A counterclockwise numbering of the array is essential, from the bottom left first corner to the top left Nth corner. Note that while anti-periodic models can be used for FEA (i.e., 1/8 models for this slot-pole combination example), periodic models must be used for SC mapping (i.e., 1/4 models for this example). There are periodic boundary conditions at either side of the polygon, as will become apparent in the proceeding steps. Also, the permeability must be defined for the various sections, namely the rotor back iron (μ_1), the airgap and slots (μ_2) and the stator teeth and back iron (μ_3). A fixed value of 1000 times that of vacuum is typical for μ_1 and μ_3, whereas a relative permeability of 1 is used for μ_2, due to the airgap and slots. At this point the magnet flux density must be defined in the model. This is done by representing the magnet flux as a series of current sheets, as seen in Figure 31.

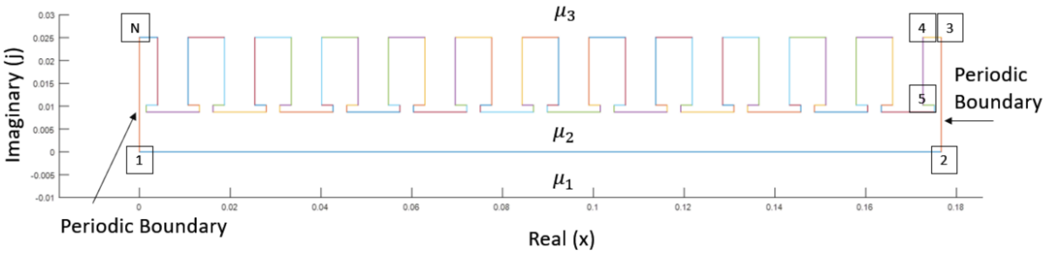

Figure 30. Periodic 2D AFM model polygon with permeable steel

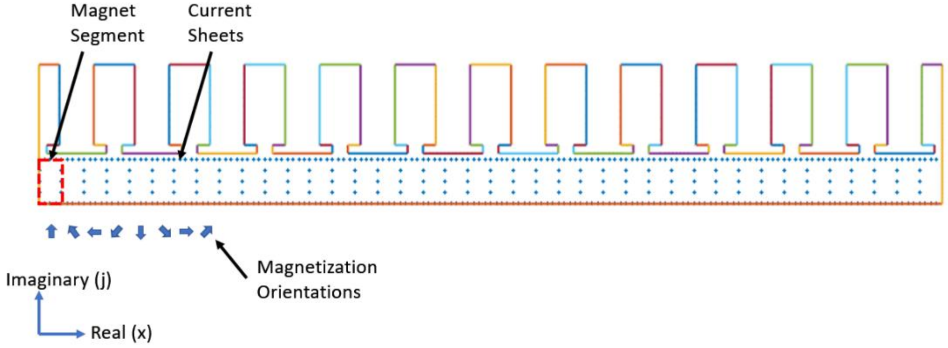

Figure 31. Polygon with current sheets used to represent Halbach magnets

The strength and position of each sheet are contained within array, *m* (separate columns). The direction of the current defines the induced magnetic field. Field accuracy is dependent on the number of discretizations used for each magnet, up to a point. A discretization of 5 on each side of the magnet seems to provide sufficiently accurate results. When Halbach arrays are used, magnets will have superposed axial and tangential magnetization orientations (see chapter 2), as labeled by the arrows below each segment in Figure 31. The vertical current sheets carry the axial component of each magnet's magnetization, and the horizontal sheets carry the tangential component. The four corner sheets will carry net magnitudes for axial and tangential magnetizations when both are present. This is done to reduce the overall number of current sheets required, and thus reduce model complexity and simulation time. The vertical current sheets can also be shared by adjacent magnets when gaps between magnets are not required for simulation. A custom algorithm is needed to determine the net magnitude of each current sheet and their positions in space and time, being dependent on the Halbach geometry used. In general, the current sheet excitation can be defined using the following equation,

$$I = \frac{B_r \mu_{mag} dL}{\mu_0 N} \qquad (11)$$

Where I is the current excitation (A), B_r is the remanent flux density (T), dL is the increment length (m) either on the j or x-axis, μ_{mag} is the magnet relative permeability, μ_0 is the permeability of free space (H/m), and N is the number of discretizations used, either on the j or x-axis. The last thing to do at this stage is to select positions anywhere within the μ_2 region at which to sample the field properties during the simulation. An example of this is points that are equally spaced over one slot pitch and axially centered within the airgap, as seen in Figure 32. They are stored in the MATLAB array, *w*.

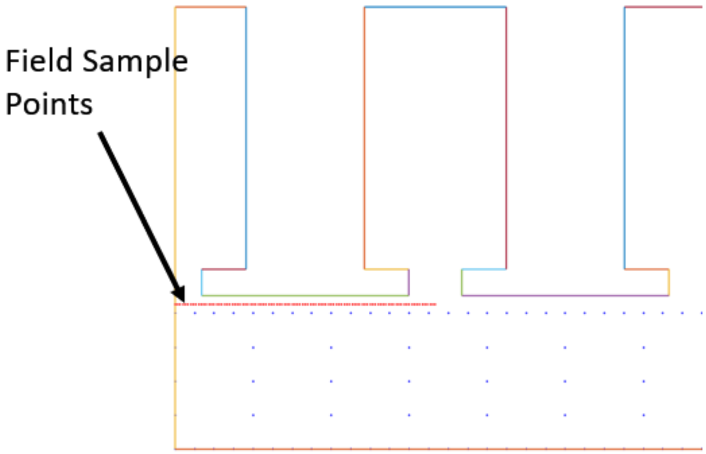

Figure 32. Field sample points

Any number of points can be selected, but simulation time generally increases with quantity. 100 discretizations are usually sufficient, it is somewhat dependent on motor size and area of interest.

3.3 Z-Plane Mapping

At this point, the SC transformation can be applied in order to map the geometry from the real (aka *W*) plane to the canonical rectangle in the Z-plane. Using MATLAB's SC toolbox, this is done by issuing the command *f* = *crrectmap(p, alpha)*. Alpha is an array containing the requisite angle of each vertex when mapped to the Z-plane. The four main corners of the polygon in Figure 30 (1, 2, 3, N) will be mapped to the four corners of the rectangle as seen in Figure 33, and so need an alpha-value of 0.5 (i.e., 90 degree right angle, 0.5π rads), with all other vertices having a 180-degree angle in the Z-plane, and an alpha-value of 1 (i.e., 1π rads). This is the Schwarz-Christoffel transformation. The sample field points can then be mapped to the Z-plane using the command *z = evalinv (f, w)* in MATLAB. Current sheets can be mapped through *s = evalinv (f, m(:,1)),* the first column of *m* in this case representing position points with complex coordinates (the second is for current magnitudes).

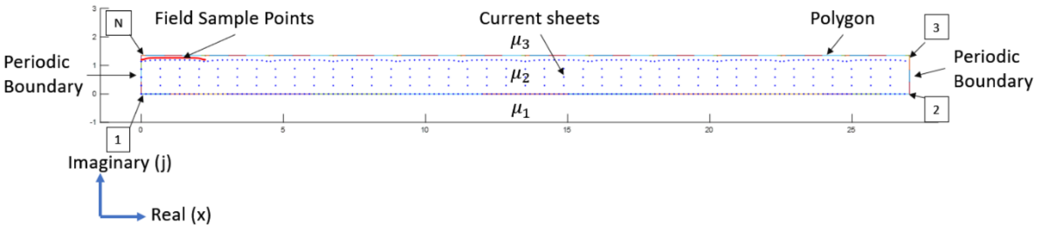

Figure 33. Z-plane transformation geometry

3.4 ζ-Plane Mapping

One further transformation is applied in order for this technique to be useful in the analysis of electric machines. It involves re-scaling and wrapping the rectangle in the Z-plane about itself, until the four corners touch, forming an annulus, as shown in Figure 34. Note that the shape of the annulus generally becomes more circular as the number of vertices used for the stator/rotor in the W-plane increases. This forms the ζ-plane. Arrays containing the equivalent points in the ζ-plane can be obtained with equation (12). In this equation ΔX is the length of the rectangle in the Z-plane along the real axis, ΔY is the length of the rectangle in the Z-plane along the imaginary axis, and j is the imaginary

$$\zeta = \exp\left(\frac{2\pi}{j\Delta X}\left(z - \frac{j\Delta Y}{2}\right) - \frac{\pi}{j}\right) \qquad (12)$$

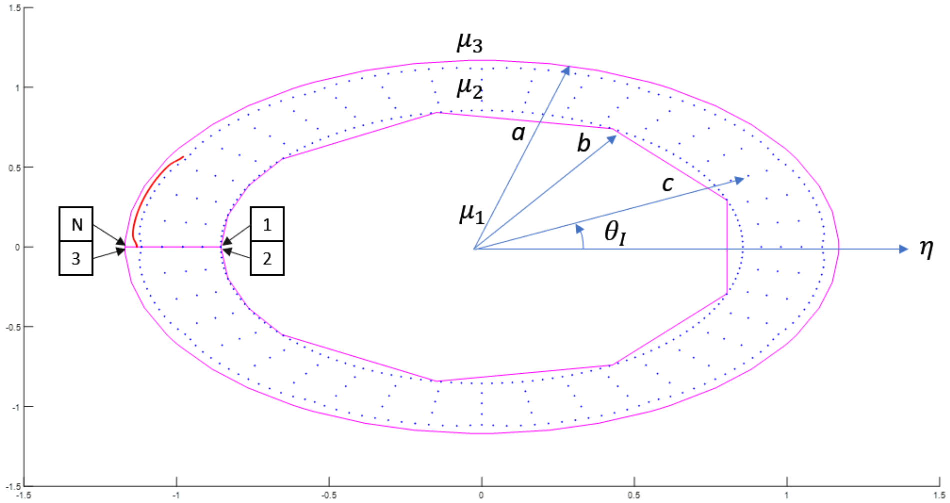

Figure 34. ζ-plane transformation geometry

unit $\sqrt{-1}$. Current sheet and sample points can be mapped through a similar equation by substituting *z* for *s* or *f*.

With the motor geometry now transformed into an annulus, a ready-made solution for the electromagnetic field between two smooth, concentric cylinders can be used to characterize the machine. It was developed by Bernard Hague [39] almost a century ago using the magnetic scalar potential, as seen in equation (13).

$$H_{cc} = \frac{B_{cc}}{\mu_0} = -\nabla\psi_{cc} \tag{13}$$

Where H_{cc}, B_{cc}, and ψ_{cc} are the field strength, flux density, and magnetomotive force in the ζ-plane. The expansion and subsequent solution to the derivation is listed below.

$$\begin{aligned} B_{cc}(r,\theta) = \hat{x}\left[-\frac{d\psi_{cc}}{dr}\mu_0 cos\theta + \frac{1}{r}\frac{d\psi_{cc}}{d\theta}\mu_0 sin\theta\right] \\ + \hat{y}\left[-\frac{d\psi_{cc}}{dr}\mu_0 sin\theta - \frac{1}{r}\frac{d\psi_{cc}}{d\theta}\mu_0 cos\theta\right] \end{aligned} \tag{14}$$

When, $r < c$:

$$\frac{d\psi_{cc}}{dr} = \sum_{n=1}^{\infty}\left(\left(A_n - \frac{I}{2\pi nc^n}\right)nr^{n-1} - nB_n r^{-n-1}\right)sin\,(n\Delta_\theta) \tag{15}$$

$r < c$:

$$\frac{d\psi_{cc}}{d\theta} = \sum_{n=1}^{\infty}\left(\left(A_n - \frac{I}{2\pi nc^n}\right)r^n - B_n r^{-n}\right)ncos(n\Delta_\theta) \tag{16}$$

$r = c$:

$$\frac{d\psi_{cc}}{dr} = \sum_{n=1}^{\infty}(A_n nr^{n-1} - nB_n r^{-n-1})\,sin\,(n\Delta_\theta) \tag{17}$$

$r = c$:

$$\frac{d\psi_{cc}}{d\theta} = \frac{I}{4\pi}\sum_{n=1}^{\infty}(A_n r^n + B_n r^{-n})\,ncos(n\Delta_\theta) \tag{18}$$

$$r > c: \qquad \frac{d\psi_{cc}}{dr} = \sum_{n=1}^{\infty} \left(A_n n r^{n-1} - \left(\frac{Ic^n}{2\pi n} + B_n \right) n r^{-n-1} \right) sin\,(n\Delta_\theta) \tag{19}$$

$$r > c: \qquad \frac{d\psi_{cc}}{d\theta} = \frac{I}{2\pi} \sum_{n=1}^{\infty} \left(A_n r^n + \left(\frac{Ic^n}{2\pi n} + B_n \right) r^{-n} \right) ncos(n\Delta_\theta) \tag{20}$$

$$A_n = \frac{-I(\mu_1 - \mu_2)\big(b^{2n}(\mu_3 - \mu_2) + c^{2n}(\mu_2 + \mu_3)\big)}{c^n 2\pi n\big(b^{2n}(\mu_1 - \mu_2)(\mu_2 - \mu_3) + a^{2n}(\mu_1 + \mu_2)(\mu_2 + \mu_3)\big)} \tag{21}$$

$$B_n = \frac{b^{2n} I(\mu_3 - \mu_2)\big(c^{2n}(\mu_1 - \mu_2) + a^{2n}(\mu_1 + \mu_2)\big)}{c^n 2\pi n\big(b^{2n}(\mu_1 - \mu_2)(\mu_2 - \mu_3) + a^{2n}(\mu_1 + \mu_2)(\mu_2 + \mu_3)\big)} \tag{22}$$

$$\Delta_\theta = \theta - \theta_I \tag{23}$$

Where *a* and *b* are the inner and outer radii of the annulus, *c* is the radial distance to each current sheet, θ_I is the angle between each current sheet and the η-axis, as depicted in Figure 34. θ is the angle between each sampling point (i.e., red points in Figure 34) and the η-axis, *r* is the radial distance to each sampling point, and *n* represents the number of harmonics to consider in the infinite series. Considering just the first 100 terms usually yields reasonable results. This calculation needs to be repeated for every current sheet in array *m*, with the final result being a superposition of the flux fields caused by each sheet, independently. This completes the calculation for one sampling point. It must then be repeated for each sampling point, at each rotor position as the machine completes an electrical cycle. Also, since this is an axial flux machine, multiple radial slices along the annulus should be analyzed in order to better capture effects from radially changing geometry, with each representing a portion of the active material that contributes to the total machine. Here it should be highlighted that reducing the current sheets, sampling points, infinite series terms, rotor position increments, and radial slices to a minimum is key to a quick analysis. 7 radial slices and 37 steps per electrical cycle usually create sufficiently discretized rotor positions. Essentially, the current sheets move linearly along the real axis in the W-plane, recycling when they reach the right periodic boundary, back to the left side, as seen in Figure 31. In the ζ-plane they rotate clockwise, with no discontinuity in their position, as the two periodic boundaries touch (Figure 34).

3.5 Converting Results Back to W-Plane

Once the B_{cc} is solved for all sample points, it can be transformed back, through the Z-plane and into the W (i.e., real) plane using the following equation.

$$B_{ag}(W) = B_{cc}\frac{\left(\frac{2\pi j\zeta^*}{\mu_0 \Delta X}\right)}{\left(\frac{df}{dz}\right)^*} \tag{24}$$

Where * represents the complex conjugate, and df/dz can be calculated using the MATLAB command *df/dz = evaldiff(f ,z)*. This completes the SC mapping analysis. The full process is loosely diagrammed in Figure 35.

Current sheets can be added to represent the conductors that produce stator field excitation as well, and this is a common addition in literature in order to analyze a machine’s full-load performance, but such an approach is neglected for this thesis in favour of collecting the no-load flux density instead. The no-load flux density can be used to predict the average full-load torque using the following equation [40].

$$T_{avg} = \frac{3}{2}pp\left(\lambda_{pm}i_q + \left(L_d - L_q\right)i_d\right) \tag{25}$$

Where λ_{pm} is the peak phase flux linkage produced by the permanent magnets, *i* is the peak current flowing through each stator coil (note that this will be less than the phase current if there are parallel connections), *L* is the phase inductance, and *d* and *q* represent the direct and quadrature components. The flux linkage can be calculated by integrating the flux density over the surface area of sampling points in the airgap for one slot pitch, as shown in Figure 32, then multiplied by the number of coil-turns per phase. The no-load flux density is used to predict torque in this thesis rather than performing a full-load analysis using SC mapping because today’s aerospace motors tend to operate under high

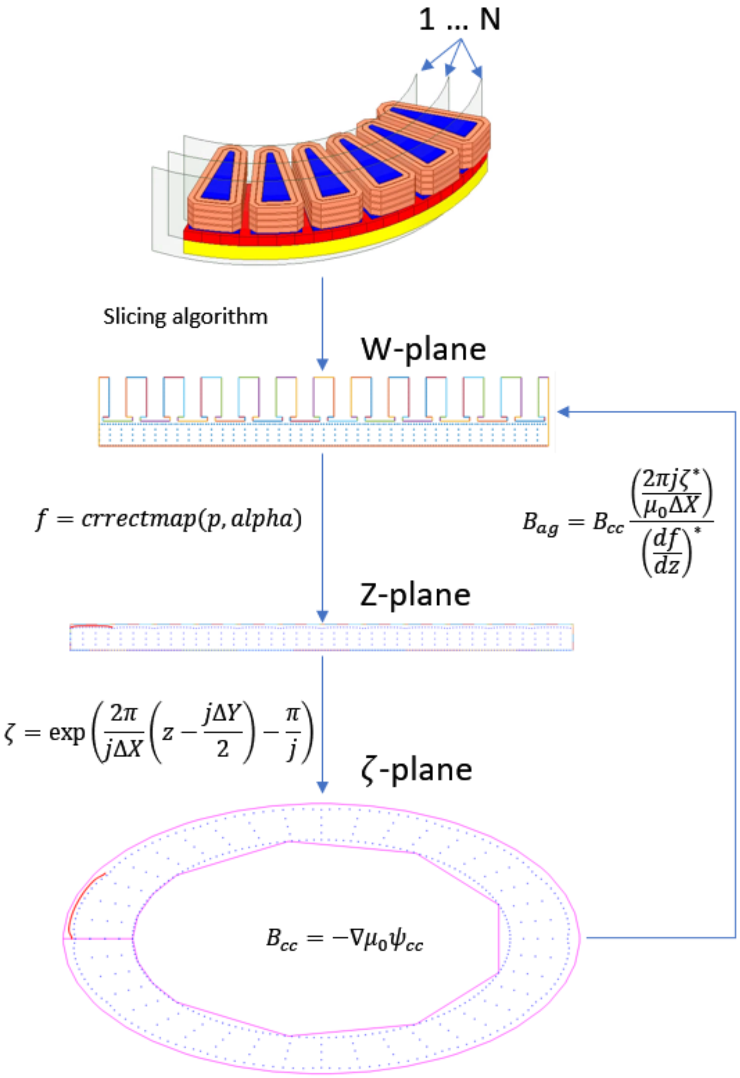

Figure 35. SC mapping process diagram

flux density saturation conditions during full load, in order to optimize material usage. Hague’s electromagnetic solution (equations (13) – (23)) assumes linear saturation of all components, but as the soft magnetic steel in a motor saturates it becomes increasingly non-linear, thus reducing analytical solution accuracy. To get around this the no-load flux density is analyzed instead, as the material is generally less saturated when stator excitation is zero.

3.6 Summary

This chapter introduced the summarized analytical equations and method for using Schwarz-Christoffel mapping to solve the magnetic field in the airgap of a slotted steel core axial flux motor with Halbach array, minimizing the need for resorting to time-consuming finite element analysis. This technique, while used occasionally for radial flux machines that can be analyzed in the 2D domain, has been slow to adapt for use in AFMs due to the three-dimensional nature of the flux field that AFMs possess. To account for this, the technique has been modified to extract two-dimensional geometry of the AFM at various slices along the radius, then mapping it to the Z and ζ-planes before solving for the magnetic field using Hague's solution to the scalar magnetic potential between two concentric rings. An inverse transformation is then used to convert the results back to the real (i.e., W) plane. The final solution is an amalgamation of the results observed from each individual machine slice. Chapter 4 will cover in detail an example of SC mapping for use in axial flux motor design involving Halbach arrays for aerospace applications.

4. Axial Flux Machine Design with Halbach Array for Electric Aircraft

4.1 Introduction to the Maxwell X-57 NASA High Lift Radial Flux Motor

NASA is in the process of prototyping a four seat, all-electric light aircraft as a proof-of-concept demonstrator for new and emerging technologies, termed Maxwell X-57. The project involves retrofitting a Tecnam 2006T twin engine gas-powered aircraft to run off lithium-ion batteries and uses 14 electric motors for propulsion. Two large 60 kW motors are used during all phases of flight, while the remaining 12 are smaller and are only active during climb and descent phases. These machines are termed 'high lift' motors (HLM). The X57 has a relatively high wing loading of 2154 Pa, compared to the base model Tecnam's 814 Pa [41]. This high wing loading is much more aerodynamically efficient at cruising speeds because of the reduction in drag. However, extra lift is needed during take-off due to this higher wing loading and this is where the HLMs come in. They employ collapsible propellers that can fold away during cruise so as to reduce drag. The aircraft, shown in Figure 36, is developing in several stages of increasing technological readiness, with the final stage culminating in a flight test where all 14 motors are fully operational. NASA is working with Joby Aviation to develop the cruise motors jointly [42], but has opted to develop the high lift motor independently instead, and opened the

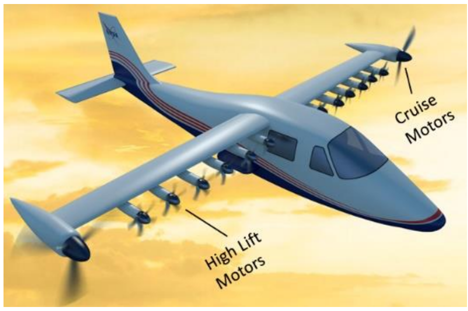

Figure 36. Maxwell X-57, High lift and cruise motors depicted [43]

project to the public to encourage further improvement. NASA Engineers at the Glen Research Center (GRC) have provided the machine requirements list in Table III.

Currently, NASA is designing a radial flux machine to meet these requirements. As part of this thesis, the mechanical assembly was reverse engineered based upon the drawings provided by NASA in [41]. The reconstruction can be seen in Figure 37 and Figure 38. The machine is cooled during operation by a propeller which attaches to the rotor hub flange (to provide lift) and forces air over the outer machine housing, which NASA has referred to as a heat sink.

The final specifications of the machine achieve the requisite 24 Nm of torque up to 6100 RPM, with a max efficiency of 96.6 %. The specific power of the active components reaches 5.64 kW/kg. Verifications performed by NASA in the design process include electromagnetic, mechanical, thermal FEA and computational fluid dynamics (CFD). The machine is already highly optimized to use as little mass as possible. Still, it

Table III. NASA HLM requirements

Torque / Speed	24 Nm / 5400 RPM
Torque / Speed	22 Nm / 5460 RPM
Efficiency / Voltage / Torque / Speed	≥ 93 % / 460 V_{DC} / 22 Nm / 4440 RPM
Minimum Voltage Supply	385 VDC
Insulation Rating	1200 V
Phases	3
Peak Current	50 A
Phase Inductance	$\geq 75\ \mu H$
Bonding Material Rating	$\geq 220\ °C$
Major Diameter	≤161.5 mm
Axial Length	≤ 66.04 mm
Active Weight	≤ 2.72 kg

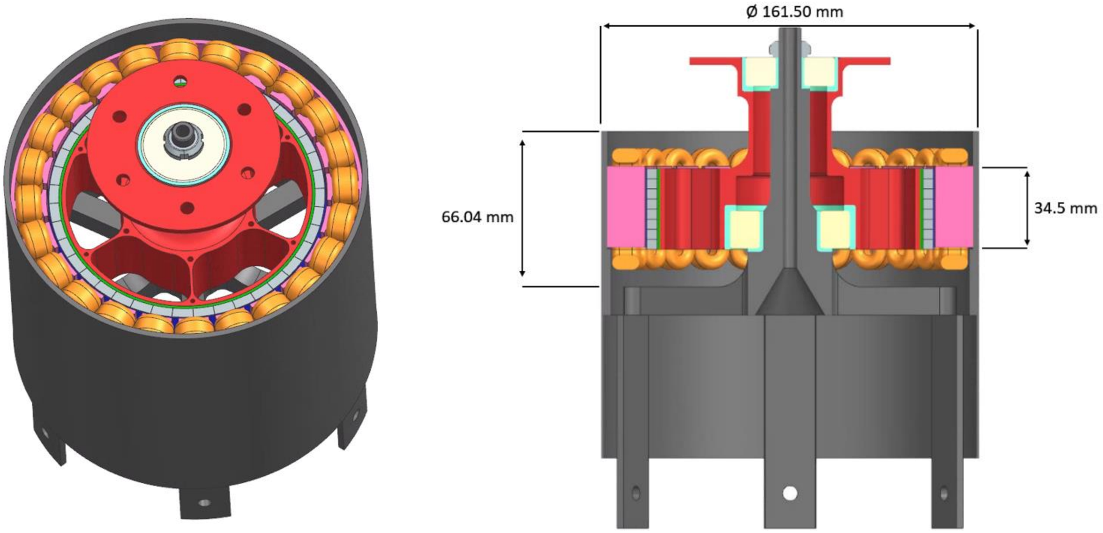

Figure 37. Reconstructed NASA HLM, angled view (left), cross-sectional view (right)

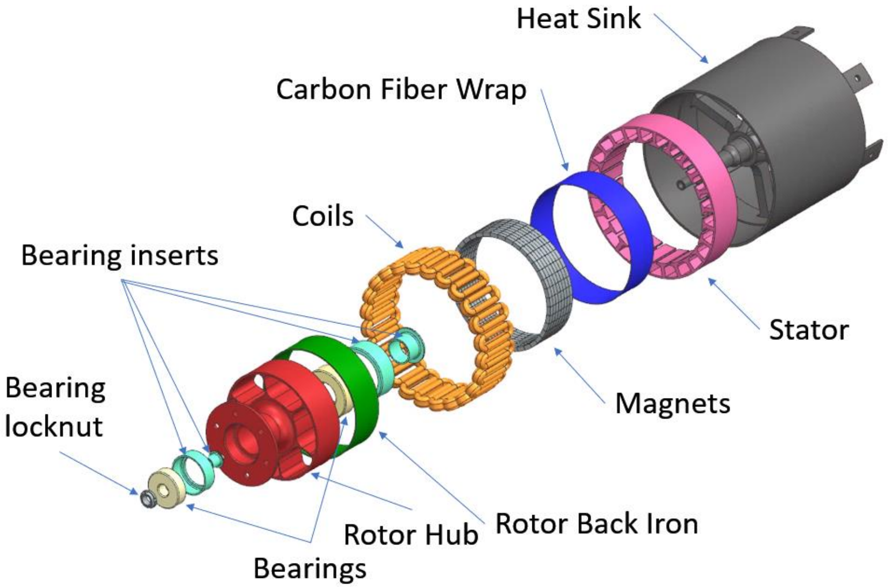

Figure 38. Reconstructed NASA HLM, exploded view

is theorized by the author of this thesis that such a design could be enhanced further. Subsequent sections will detail the redesign process of the HLM. But first, a number of important details were left out of NASA's reporting which are essential for improving upon their pre-existing body of work. To obtain these, mechanical and electromagnetic FEA of the existing radial flux machine will be re-performed and compared against those which NASA has already reported to ensure completeness of the models. Thermal FEA and CFD are being performed by other researchers at MARC.

4.1.1 Verification of NASA's Electromagnetic Results

Electromagnetic performance for the HLM was done by NASA using Motor-CAD. Therefore, it makes sense to start there. The active components of the machine are listed in Table IV and are shown in the re-constructed Motor-CAD model in Figure 39. Hiperco 50 is a cobalt steel alloy, made by Carpenter Technologies. It has exceptionally high permeability, saturation flux density, and low core loss. It is a premium alloy normally reserved for the most demanding applications, such as those found in aerospace. N48H is a high temperature resistivity magnet capable of withstanding up to 120 °C, with room temperature remanence of 1.39 T. The bonding agent used, EB 548, is a relatively low temperature epoxy that only exhibits useful peel strength up to 140 °C. As specified in Table III, this falls well below the 220 °C requirement. NASA has addressed this by providing additional spot welds to reinforce the laminations, should 140 °C be exceeded.

The winding configuration used is diagrammed in Figure 40. A concentrated winding is implemented to obtain the shortest possible end turns.

Table IV. NASA HLM active materials

Stator Laminations	Hiperco 50, Stator Grade, 0.15 mm
Rotor Back Iron Laminations	Hiperco 50, Rotor Grade, 0.15 mm
Coils	Copper, 100 % IACS
Magnets	N48H
Lamination Bonding Agent	Remisol EB 548

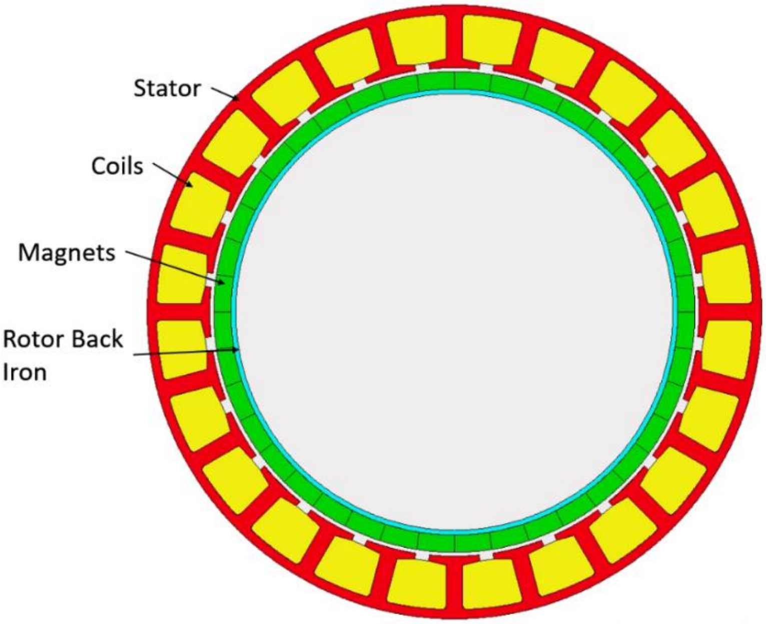

Figure 39. Reconstructed NASA HLM Motor-CAD model

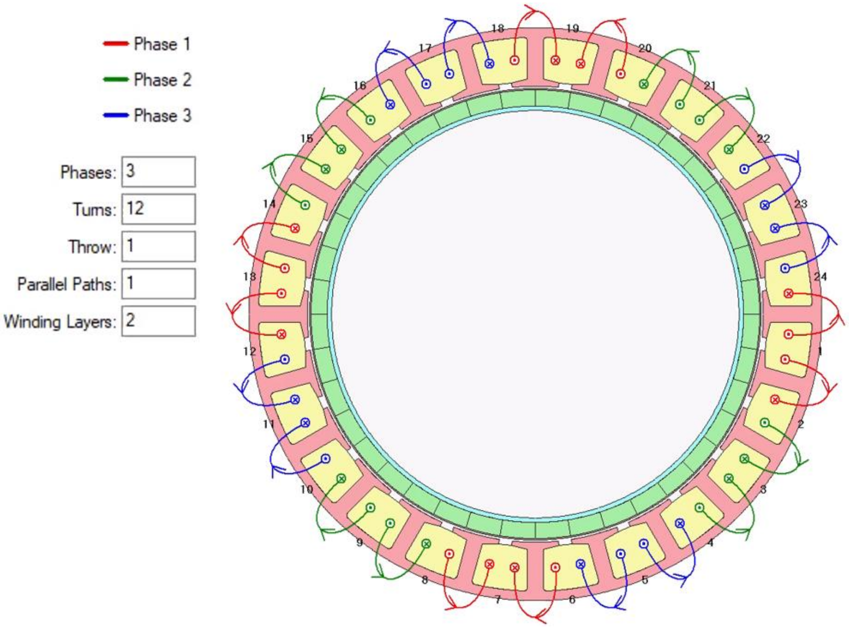

Phases: 3
Turns: 12
Throw: 1
Parallel Paths: 1
Winding Layers: 2

Figure 40. Reconstructed NASA HLM winding

NASA specifies litz wire to be used for the coils, along with the winding properties listed in Table V. Their target is a maximum of 60 % coil fill factor (K_{cw}), as defined by equation (26), where N is the number of turns per coil, A_{wire} is the area occupied by the covered litz wire, and A_{slot} is the slot cross-sectional area. Copper fill factor is defined similarly, except A_{wire} represents the area of uncovered litz wire instead.

$$K_{cw} = \frac{NA_{wire}}{A_{slot}} \tag{26}$$

K_{cw} of 60 % is a very optimistic target, usually only achieved under ideal circumstances. NASA has specified litz bundle type 1, which is a relatively straight forward litz bundle. In type 1, a series of insulated conductor strands are twisted together at regular intervals to form a larger equivalent conductor. The use of round wires, individual insulations, and twisting (transposition) all work to reduce maximum achievable K_{cw} with litz. Litz can also be insulated at the bundle level (served), which decreases fill factor further. A typical litz bundle fill factor, as defined by litz wire manufacturer, Elektriksola, is approximately 60 % for 28 AWG strands. That is the ratio of conductor area to bundle cross-sectional area [44]. Assuming 100 % of slot space is used by the litz (meaning zero space between bundles), the maximum theoretical coil factor would be ~60 %. It is anticipated that NASA might have difficulty reaching a K_{cw} of 60 % in practice.

Table V. Reported NASA HLM winding properties

Litz Bundle Type	1
Number of Strands in Hand	48
Wire Gage	28 AWG
Connection	Wye
Coils	24
Wire Insulation	Polyimide MW-16C, Single Build
Slot Liner Insulation	Nomex-410
Slot Liner Thickness	0.127 mm

The results of the winding reconstruction compared to NASA's reported results are shown in Figure 41 and Table VI. Note that a nominal copper wire diameter (D_{Cu}) of 0.32 mm and minimum insulation thickness of 0.01016 mm are used for the reconstruction, as specified by NEMA MW 1000 for the 28 AWG MW-16C, single build wires [45] listed in Table V.

When 48 strands of 28 AWG wire are used, the copper fill factor and total copper mass are reasonably accurate when compared against NASA's at 56.35% and 1.04 kg, but the coil fill factor exceeds the 60 % cut-off. It can be calculated by using the following formula,

$$\frac{Coil\ Fill}{Copper\ Fill} = \left(\frac{D_{ins}}{D_{Cu}}\right)^2 \tag{27}$$

Where D_{ins} is the insulated wire diameter. For NASA's copper and coil fill factor to actually be 56.18 and 58.41%, the insulation thickness would have to be 3 microns thick, which seems unlikely. Insulation typically results in an increase of coil versus copper fill

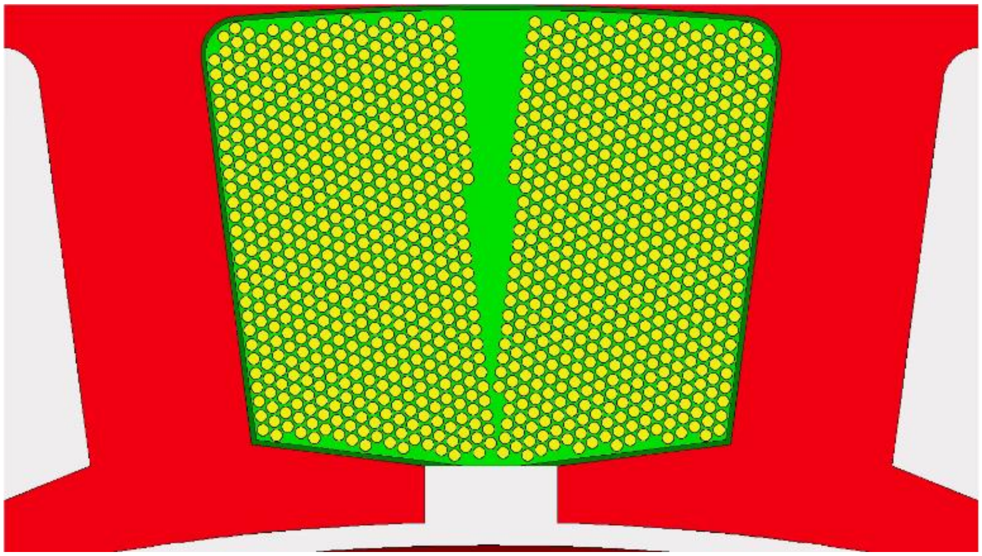

Figure 41. Reconstructed coil winding design, 48 strands, 12 turns

Table VI. Reported versus reconstructed winding specifications

	NASA Reported	Reconstructed
Copper Fill Factor	56.18 %	56.35 %
Coil Fill Factor (K_{cw})	58.41 %	63.76 %
Slot Fill Factor	N/A	67.33 %
Total Copper Mass	1.0 kg	1.04 kg
Current Density	10.7 A/mm^2	9.16 A/mm^2
DC Coil Loss (129 $°C$)	N/A	240.6 W
AC Coil Loss (129 $°C$)	N/A	5.0 W
Total Coil Loss (129 $°C$)	253.8 W	245.6 W

around 5–10 % for highly stranded windings such as this. Slot fill factor includes the non-negligible area occupied by the slot liner, in addition to covered wire, and exceeds 67 %. This was neglected by NASA but calculated for the reconstruction. Additionally, the reconstructed current density of 9.16 is significantly lower than 10.7 A/mm^2. It is presumed that the 'worst-case current density' NASA stipulates in their report as 10.7 refers to some undisclosed over-current condition. NASA does not report coil losses as AC or DC, just 'Windings' loss at 5400 RPM and 50 A current. The DC loss is reconstructed in Motor-CAD, whereas the AC loss was reconstructed in ANSYS Maxwell, as shown in Figure 42. A 2D quarter model was used to simulate coil AC losses. The 3 phase windings are colour coded and each litz bundle conductor is represented by one circle. Note that the conductors are reflective of bundle conductor equivalent area, not bundle diameter, which is unknown. ANSYS Maxwell's litz wire setting is used to simulate the effect of using litz wire on loss reduction. The size and quantity of individual strands (from Table V) are used as inputs and the solver calculates the losses using the time derivative of flux and current density passing through the wires. The software assumes that the bundles are sufficiently stranded to eliminate skin effect, and strands are twisted at length intervals of 15–20 times the individual strand diameter, so as to ensure each strand sees the same flux linkage across its length, which is done to minimize proximity effect. ANSYS Maxwell's litz wire setting is a post-processed

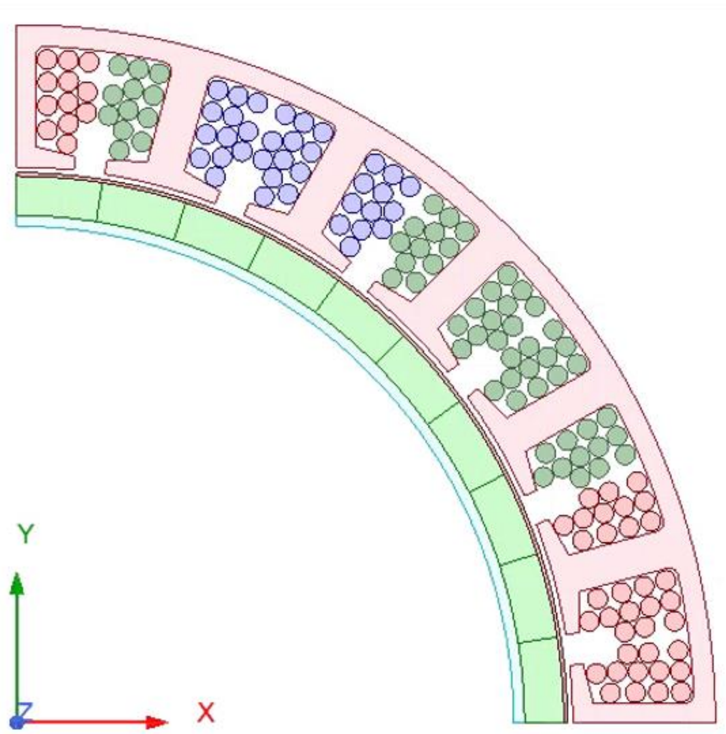

Figure 42. ANSYS Maxwell HLM reconstruction, 2D quarter model

analytical calculation that the solver makes, as it would be otherwise impractical to model every strand and twist in the litz [46] for FEA. Litz modeling is something that Motor-CAD cannot do, which is why Maxwell was used, just for the AC loss. Note that the AC loss calculated in ANSYS Maxwell 2D is only for the axial stack length of the machine and does not consider any AC loss occurring in the end windings. It is possible the total AC loss would increase if it did, but it is assumed that the skin and proximity effect in this area are small.

The rotor and stator core performance were reconstructed at 5400 RPM, 50 A current input, and comparisons against NASA specifications can be found in Table VII. NASA does not specify whether they use rotor grade Hiperco for the rotor back iron or not, but it is assumed to be the case in this instance. The material is heat treated differently than stator grade Hiperco, in order to improve its structural properties at moderate expense to its magnetic properties. The lamination is quite thin at 0.15 mm, and so since a stacking

Table VII. Reported versus reconstructed rotor and stator core specifications

	NASA reported	Reconstructed
Slots	24	24
Stator Stacking Factor	N/A	95 %
Rotor Stacking Factor	N/A	95 %
Stator Core Loss	117.6 W	111.0 W
Rotor Core Loss	3.85 W	2.80 W
Stator Mass	0.826 kg	0.805 kg
Rotor Mass	0.099 kg	0.115 kg

factor is not specified by NASA, an assumed upper limit of 95 % is chosen for both rotor and stator, which was identified as a reasonable balance between mass, core loss, torque accuracy and manufacturer capability, during the model reconstruction process.

The magnet array performance was reconstructed at 5400 RPM, 50 A current input, and comparisons against NASA specifications can be found in Table VIII.

Table VIII. Reported versus reconstructed magnet specifications

	NASA reported	Reconstructed
Magnet Material	N48H	Arnold Magnetics N48H
Remanence (20 °C)	1.39 T	1.39 T
Coercivity (20 °C)	1046 KA/m	1054 KA/m
Remanence (90 °C)	N/A	1.273 T
Coercivity (90 °C)	N/A	755 KA/m
Poles	20	20
Halbach Array	4-segment	4-segment
Axial Segmentation	8	8
Total Magnet Pieces	320	320
Mass	0.418 kg	0.422 kg
Magnet Loss (90 °C)	15.0 W	7.5 W

The machine uses a 20-pole magnet array configured into a 4-segment (per pole pair) Halbach, which NASA states improves torque by 6 % compared to a conventional North-South array. The magnet orientations can be seen in Figure 43. They are split axially (into the page) by up to 8 segments in order to lower the magnet eddy current losses as much as possible. Arnold Magnetics N48H is selected to replicate the performance of the N48H magnet used in NASA's analysis. The flux density remanence and coercivity at 20 $°C$ match their reported values well. Total magnet mass is also very close to the NASA estimate. The magnet loss, however, is 50 % lower (15 W versus 7.5 W) than that reported by NASA. It is assumed that this discrepancy is due to the resistivity of the magnet material used by NASA, likely coming from a different supplier. The difference is considered negligible given the very low magnet loss in general, relative to other sources of loss in the machine.

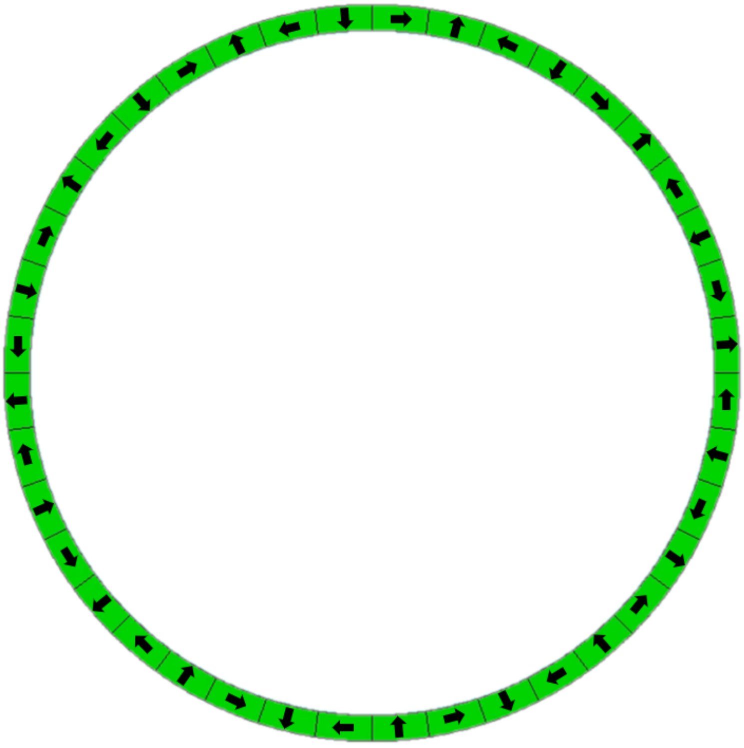

Figure 43. Reconstructed NASA HLM magnet Halbach array orientations

The final machine performance comparison at 5400 RPM and 50 A current input is summarized in Table IX. Note that some results have already been presented in previous tables and are reported here again just for clarity. The torque matches closely to NASA's reported value. The base speed is 358 RPM (i.e., 6 %) higher and it is anticipated this is due to slight differences in the model affecting Motor-CAD's estimation, such as the q-axis inductance, which was not reported by NASA.

4.1.2 Verification of NASA's Mechanical Results

A mechanical static stress analysis using Ansys Workbench (also used by NASA) was run on the motor using most of the reconstructed geometry in Figure 38 in an effort to verify material selection, loading and support constraints. A cross-section of this set-up can be seen in Figure 44. Note that the rotor back iron, magnets, and carbon fiber wrap were deemed unnecessary for this study. The loading is based on NASA's reported worst case scenario of combined moments, forces and accelerations. There is a vector force of -414 N, -119 N and 119 N in the X, Y, and Z-direction, respectively. Note the positive directions of the coordinate system are displayed in the Figure 44 cross-sectional view.

Table IX. Reported versus reconstructed machine performance summary

	NASA reported	Reconstructed
Peak Torque	24 Nm	24.17 Nm
Torque Ripple	N/A	7.1 %
Cogging Torque	N/A	1.50 Nm
Induced Voltage	N/A	190.5 V
Base speed	6100 RPM	6458 RPM
DC Coil Loss (129 $°C$)	N/A	240.6 W
AC Coil Loss (129 $°C$)	N/A	5.0 W
Total Coil Loss (129 $°C$)	253.8	245.6 W
Stator Core Loss	117.6 W	111.0 W
Rotor Core Loss	3.85 W	2.80 W
Magnet Loss (90 °C)	15.0 W	7.5 W

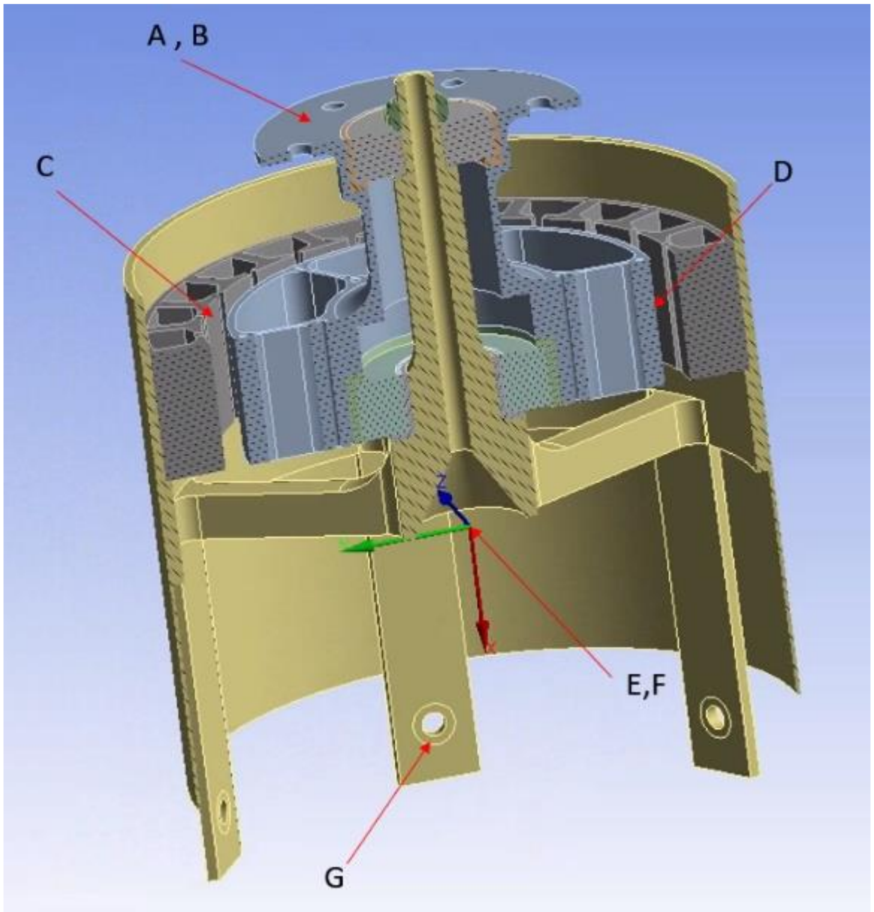

Figure 44.NASA HLM reconstruction mechanical FEA setup

NASA specifies force application at the propeller centroid. Propeller geometry was not provided with NASA's data and so this exact location is unknown. Since force is transmitted through the rotor flange, the point of application is selected to be on the top rotor flange face (A), for the reconstructed FEA. An extra load of 1 Nm is applied about the Y and Z-axis to account for any moments generated by the forces being applied at the rotor flange rather than propeller centroid, which would be slightly offset in the X-direction. NASA also reports moment loads of 24 Nm, 29 Nm and 44 Nm about the X, Y and Z-axis, respectively. These moments, also applied about the propeller centroid, are positioned on the rotor flange (B) for this study. NASA specifies accelerations of -1.33 G and -3.4 G in the Y and Z-directions, respectively, and these are applied about the origin (E). In addition to these forces, a reactive moment of -24 Nm is applied about the rotor hub (D) to oppose the load torque applied about the rotor flange. The two forces together create net zero rotor acceleration but exert a torsional stress on the rotor hub. Similarly, a moment of 24 Nm is applied to the stator shoes (C), which simulates the effect of tangential electromagnetic force exerted by the rotor on the stator, exerting torsion of the stator and heat sink. Fixed supports are applied to the bolt holes (G). It is possible NASA intends to weld the heat sink to the wing rather than use fasteners. This was not made clear from their designs, which sometimes included bolt holes in the cad but no corresponding dimensions on the drawings. Because of this, place holder 6.35 mm (1/4 in.) holes were used, and it is assumed that the motor is held in place at these points. The final stress results on the heat sink and rotor hub are shown in Figure 45 and Figure 46.

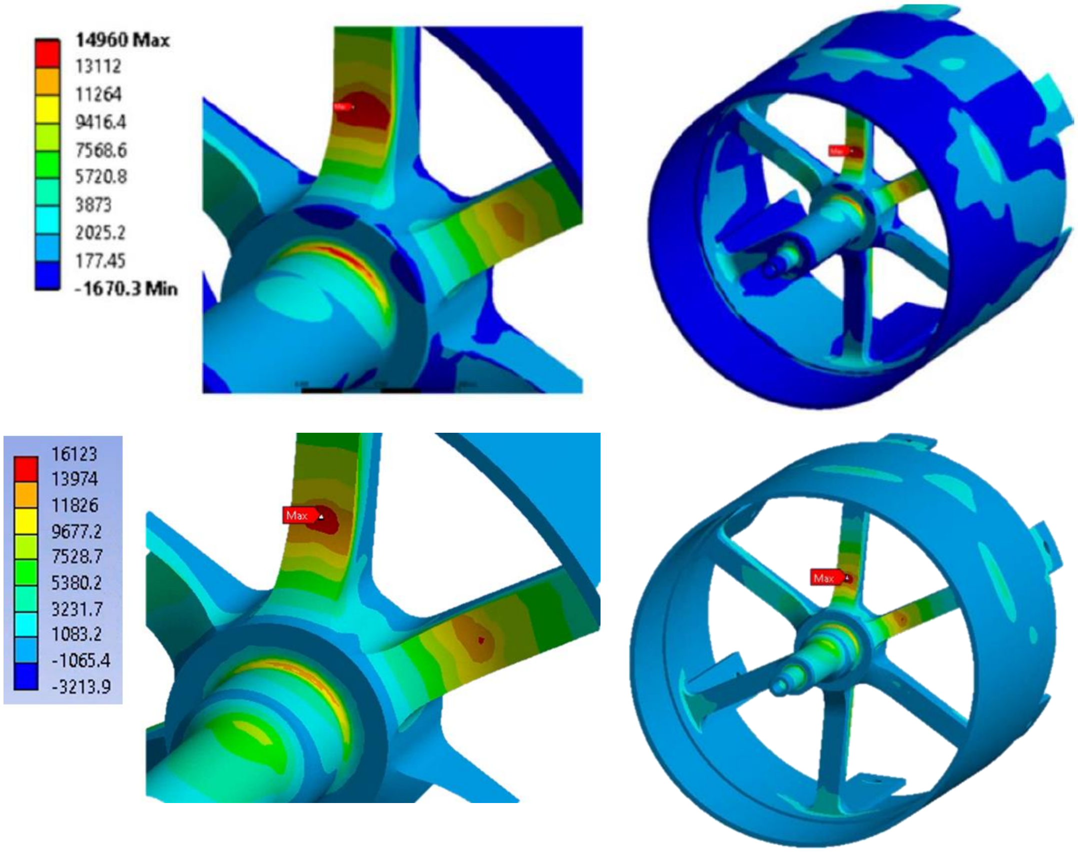

Figure 45. Comparison of principal stress (in PSI) on heatsink, NASA results (top) [41] versus reconstructed results (bottom)

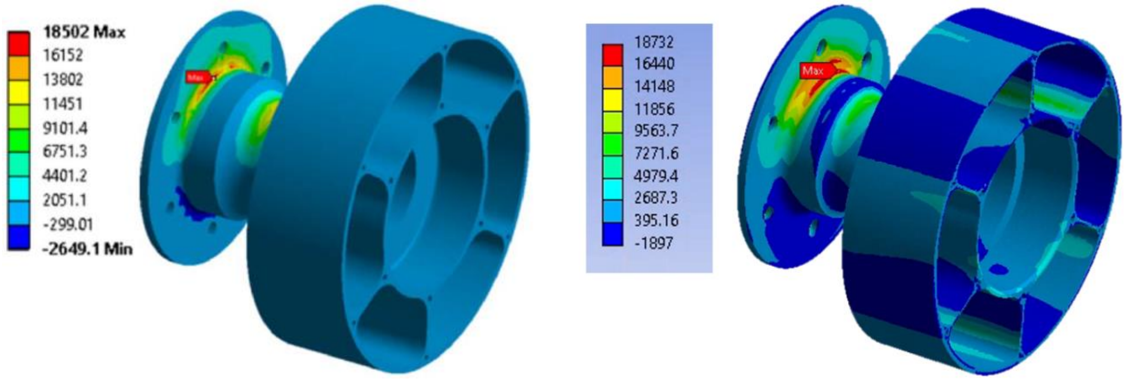

Figure 46. Comparison of principal stress (in PSI) on rotor hub, NASA results (left) [41] versus reconstructed results (right)

The rotor hub peak tensile principal stress shows a decent match for the rotor hub at 18.5 vs. 18.7 KSI. There are striations induced on the rotor hub magnet surface OD not visible in NASA's model. This may be caused by their bearing joint model conditions inhibiting free rotation and thus no reaction moment would be needed on the rotor hub OD (at the expense of neglecting any torsion). The heat sink tensile stress is somewhat off when compared against NASA's, at 14.96 KSI vs. 16.1 KSI. It is theorized that this is caused by differences in the overall assembly not reported by NASA. For example, the bearings and bearing inserts were largely reconstructed based on the images presented in publications as NASA neglected to provide information for these components, including what were the exact materials used. It also seems like NASA changed the design somewhat, before FEA, as compared against the part drawings they have provided. This is evident from the differences in the bearing seat on the rotor hub, which is much thicker in NASA's FEA design, as indicated by the circles in Figure 47, and also can be seen, somewhat, in comparing the reconstruction to the original in Figure 46.

It is because of the limited information provided by NASA for certain mechanical components, especially the propeller and propeller mount, and the outdated nature of the drawings that the mechanical analysis validation is concluded as is, and rotordynamic verification is not pursued as the results would not reflect NASA's current design.

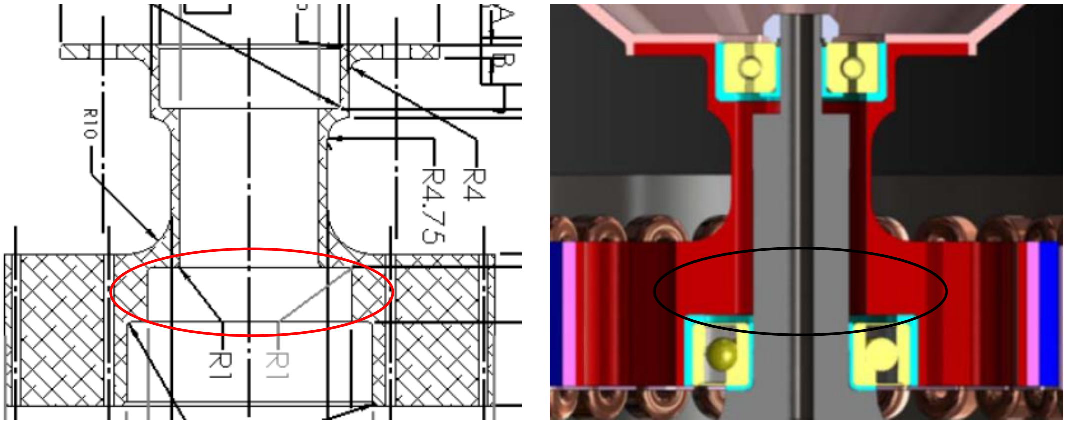

Figure 47. NASA HLM model differences between drawing (left) and cad (right) [41]

4.2 Proposed YASA Configuration Redesign

Typical goals that are targeted during a machine redesign include: reducing mass or volume, increasing efficiency, improving torque quality and/or increasing power. It is difficult to reduce mass or volume in NASA’s concept because it has been minimized and lightweighted to the point where there is very little excess material left. For example, the rotor and stator yokes are as thin as 1.23 mm and 1.9 mm, respectively. Improving efficiency would also be difficult, as it already exceeds 96 % at the requisite operating point. Any gains in motor efficiency risk being marginal. Similarly, the Halbach array implemented greatly reduces the cogging torque and torque ripple inherent in the design. Increasing the power, in contrast, seems like a potentially achievable outcome.

NASA reports an HLM base speed of 6100 RPM at 24 Nm. That represents a 13% increase in power over the maximum required (13.57 kW). This provides some level of robustness, as 24 Nm can be achieved at requisite operating speed (5400 RPM) even if the battery supply voltage drops below minimum specification (385 VDC). However, the added benefits end there. Increasing the rotational speed is not practical at the system level, because the structural loading of the propeller blades can only take a maximum of 5460 RPM [47]. It is also not possible to increase the torque, because the maximum current is already being used to achieve the 24 Nm required. Thus, while it is clear that that some level of power increase is feasible prior to exceeding the voltage and current limits of the system, for electrical and mechanical reasons it is not achievable with the current design, and room for improvement exists.

An increase in HLM power would be useful because it enhances lift and increases the altitude ceiling at which the X57 can cruise at. A higher ceiling would increase the vehicle's true airspeed and potentially make flight more efficient. The current limit for the Maxwell X57 is between 1800 and 2100 meters Mean Sea Level (MSL) [47], whereas the Tecnam P2006T it is built from can reach 4200 meters [48]. While increases in power through higher rotational speeds are not practical due to system constraints, increased power through higher torque could still be realized, as there is no currently identified upper limit on how much torque the motors can be capable of. Another compelling reason to increase torque capability is that it would provide a margin of error to still achieve torque output objectives when comparing simulated to experimental values during prototyping. The current design achieves the 24 Nm target exactly at the peak current specification. It is likely that the as-manufactured condition will reduce this amount. This could come from weld spot heat affected zones locally reducing stator/rotor core permeability (the laminations are spot welded and bonded), or from the laser cutting process (low volume production Hiperco laminations are usually laser cut) which also reduces lamination edge permeability. Or it could from general airgap manufacturing and assembly tolerances inducing rotor eccentricities (which are predicted to create airgap variance of greater than 50 % in the worst case [41]), or from PWM effect in the inverter, or from errors in the estimated magnet temperature coming from thermal FEA (a 20 % factor of safety is not uncommon), or from slot fill factor manufacturing limitations which already will be difficult as the design exceeds 60 %.

There are several traditional redesign options to increase torque in the existing motor configuration that can be ruled out fairly quickly. These include reducing the magnetic airgap, increasing the magnet thickness, using a higher segmentation Halbach array, increasing the winding turns, reducing the magnet temperature or using a different magnet grade with higher remanent flux density at the requisite operating temperature. Reducing the airgap is not possible as the current tolerance requirement takes up 0.89 mm of the 1 mm mechanical gap [41]. Increasing the winding turns is unfeasible due to the pre-existing high fill factor discussed in Section 4.1.1. Reducing the magnet temperature would be difficult without somehow further reducing the pre-existing machine losses. Increasing the Halbach segmentation, magnet thickness, or improving the magnet grade are also unlikely to yield much improvement, as the average flux density in the stator teeth and yoke exceeds 2.3 T [41] which, for Hiperco50, equates to a relative permeability of about 60, compared to its peak of 15,700. This was intentional, as the machine is crafted to operate under heavy saturation so as to reduce the component thicknesses and thus, mass, to its utmost minimum. It is unclear how much torque increase would be gained through any changes to the magnet, without substantial changes to the stator/rotor.

Thus, the current concept is so highly optimized that it would be difficult to yield higher torque outputs without impacting the overall machine weight, volume, and/or efficiency. Instead, a different topology is proposed for investigation, this being the YASA axial flux machine. YASAs typically yield high torque-to-weight ratios, and could potentially achieve higher than desired torque targets, in part due to the elimination of the stator yoke needed for other topologies whose thickness restricts maximum flux linkage. In addition to stator yoke elimination, use of a Halbach array makes it very possible to eliminate the rotor yoke that is also typically needed to support flux linkage. By removing the two thinnest components of the machine and using a very torque dense axial flux design, it may also be possible to reduce the active mass and volume of the motor beyond what NASA has already achieved with an RFM, while still reaching the requisite torque. Such reductions can be very beneficial towards energy conservation of the limited capacity battery, which takes energy to propel the plane mass forward, and to resist drag force on the 12 motor cross-sections. Therefore, two redesign AFM variants will be explored, and are summarized in Table X.

The first variant will be a high torque design that can achieve at least 110 % of the RFM's rated torque while the mass, volume and power loss are equal to or better than the RFM. The second variant will be a low mass and volume design that needs less than 90 %

Table X. Redesign objectives summary

AFM Design 1 (AKA 110 % torque)	• ≥ 110 % RFM torque (26.4 Nm) • ≤ 100 % RFM active mass (2.343 kg) • ≤ 100 % RFM volume (19,223 mm^2) • ≤ 100 % RFM losses at 5400 RPM (390.25 W)
AFM Design 2 (AKA 90 % mass/volume)	• ≥ 100 % RFM torque (24 Nm) • ≤ 90 % RFM active mass (2.109 kg) • ≤ 90 % RFM volume (17,300 mm^2) • ≤ 100 % RFM losses at 5400 RPM (390.25 W)

of the material and cross-sectional area used in the RFM while torque and power loss are equal to or better. Active length will also be held constant (or better) in this design, such that the volume reduction will be most beneficial towards reducing the frontal area of the plane. An improvement threshold of 10 % for both cases is perceived to be the minimum value that could justify a redesign from RFM to AFM at the system level and would be observable upon completion of a prototype possessing a tolerance band on how much better or worse the machine could be from the nominal after manufacturing imperfections are accounted for.

The difficulty of this redesign will be improving performance while holding other constraints constant. The present design has already been iterated upon extensively, so it would not make sense to improve one machine parameter at the expense of another, as NASA has already tried that and found the present configuration to be optimal. By that same logic, it could also be the case that extra torque is not desirable from a system perspective for some undisclosed reason, or perhaps that a reduction in mass reduces the wing loading of the plane, making it disadvantageous. From an external perspective, it is difficult to know what combinations of performance are considered desirable improvement for the system as a whole. By targeting two separate machine improvement objectives, it increases the likelihood of at least one variant being superior when the system-level design is considered.

For such a redesign, the specifications and performance metrics listed in Table XI will be used as guides. Where applicable, values reported by NASA are used and reconstructed values are chosen for those left unreported. Machine constraints largely adhere to those set forth by NASA, with the exception of the mass constraint, which will be equal to or better than NASA's final design, depending on the variant. Material specifications used during the reconstruction will continue to be applied for the redesign. The litz bundle type, winding configuration, insulation class and thickness adhere to NASA's, but the strands, gage and coils are left free to vary, as there is no compelling reason to reuse NASA values. The slot fill factor is capped at 67.33 %, as per NASA's design, but there is an added litz fill factor, which is new. As mentioned in section 4.1.1, litz wire does not have a 100 % bundle fill factor. Voids between wire strands, strand insulation, transposition and serving/taping all work to reduce what percentage of space is actually occupied by copper in a litz bundle cross-section. It is unclear if NASA accounted for this in their initial design, but it will be henceforth. Profiled litz wire by

Table XI. HLM RFM specifications used in YASA redesign

Machine Constraints	-Table III, except mass (see Table X)
Material Specifications	-Table IV, with Arnold Magnetics N48H
Winding Specifications	-Table V, except strands/gage/coils -Litz fill factor = 80 % -Wire aspect ratio = 1.7 -Strands = 26 AWG -Slot Fill Factor $\leq$ 67.33 %
Temperature Specifications	129 $°C$ Windings, 90 $°C$ Magnets
Torque / Speed / Phase Voltage Torque / Speed / Efficiency	24 Nm or 26.4 Nm / 5460 RPM / 222 V 22 Nm / 4440 RPM / 93 %
Airgap	1.0 mm
Magnet Array	24-pole Halbach, except 8-segment, no rotor backiron

manufacturer Elektrisola is selected for the design. Profiled litz wire is typically formed by rolling round wire strands into square shapes, which reduces the inter-wire voids and increases litz bundle fill factor. Elektrisola stipulates that they can achieve an 80 % litz fill factor with 26 AWG strands, and that their profiled litz is restricted to a 1.7 with-to-height aspect ratio [49], so these values and wire gauge are used for the redesign. Typical profiled litz wire from Elektriksola can be seen in Figure 48, note the transpositions. The litz fill factor links the coil and copper fill factors by the following relationship.

$$\frac{Copper\ Fill\ Factor}{Litz\ Fill\ Factor} = Coil\ Fill\ Factor \tag{28}$$

The same magnet and winding temperatures from NASA's thermal analysis will be used for the purposes of electromagnetic analysis, until updated values become available for the redesigns. The torque/speed points were taken from NASA's reference design and used as metrics to meet or exceed. The mechanical airgap is also reused from NASA's design, for comparative purposes, although hypothetically an AFM is less likely to need a rotor airgap retainer than an RFM (which is 0.381 mm in NASA's design) and could potentially have a smaller airgap. The magnet array is selected to be a 24-pole Halbach, similar to the reference design and thus ensuring similar fundamental frequencies, but an 8-segment (per pole pair) array, yokeless rotor is selected for the YASA redesign. This is in contrast to the 4-segment array with rotor backiron used in NASA's machine. An 8-segment array will increase airgap flux densities for the same

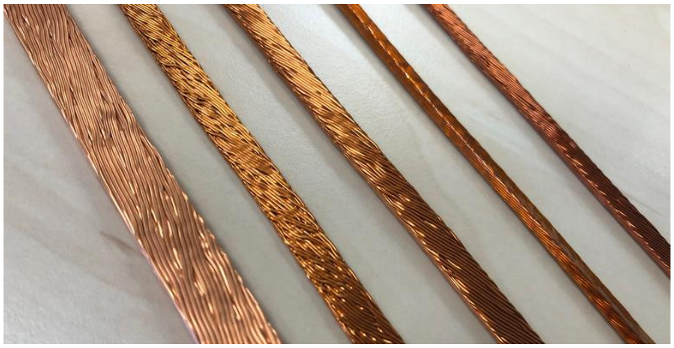

Figure 48. Profiled rectangular litz wires [49]

magnet volume, as well as reduce magnet loss through the added segmentation. The higher airgap flux densities will also assist in removal of the rotor back iron altogether. NASA's reference design implements a 1.23 mm thick Hiperco50 rotor yoke that makes up less than 4 % of the total active mass but 37 % of the active material cost. Compared to the stator, which is also made of Hiperco 50, it is 8 times less massive, but only 25% cheaper. Thus, it is concluded that the amount of material used in its design is not a key cost driver, but rather the complexity associated with its construction. The rotor has a thickness-to-length ratio of 1:24, which likely makes it difficult to manufacture reliably with the precisions needed. It is therefore viewed as beneficial from both a cost and system design perspective to choose solutions that allow for its removal. This is even more essential for an axial flux machine, which typically has a more complex rotor yoke to manufacture (due to lamination direction), and often contributes to a reduction in rotor structural integrity, rather than improvement.

4.3 Analytical Optimization of YASA Machine

Typical AFM optimization involves numerous painstakingly slow adjustments to geometry in 3D FEA that take weeks to months to conclude. It is strongly advantageous to have an analytical solution for AFMs that can be processed orders of magnitude faster than typical FEA and cover a much broader range of possibilities. Potential analytical solutions to the flux field in AFMs have been presented in chapters 2 and 3. While the analytical equations presented in chapter 2 are suitable for coreless AFMs, they struggle to accurately capture performance of steel core machines, particularly when the stator has slots, as will be the case for a YASA. Coreless AFMs, while great for efficiency, really struggle to achieve high power density that make them poorly suited for this HLM redesign, and thus have not been considered. SC mapping presented in Section 3, in contrast, is very well-suited to accommodate the slotting effect in YASA AFMs, and a solution demonstrating this approach will be presented in the following sub-sections.

To find the best possible AFM design to match NASA's specifications, the machine geometry is fully transcribed into mathematical equations for analysis. Once this is done, many of the machine parameters (i.e., spacings) are fixed, due to mechanical constraints, while seven variables are left free to vary, as they do not have obvious mechanical constraints, and are concluded to substantially impact the machine's overall design. These variables are listed in Table XII. The active axial length of the machine includes distance from the one side of the machine to the other, as depicted in Figure 49. A minimum bound on the axial length is set at 30 mm just because it seems unrealistic that the design could be any smaller than that, from experience. The maximum upper bound on the active axial length is set at 50 mm. Since the maximum machine length is 66.4 mm, this gives room for at least a 7 mm rotor carrier thickness to hold the magnets, with 1(+) mm clearance from any endcap. A minimum magnet thickness of 4 mm is set just below the NASA RFM design of 4.31 mm and a maximum magnet thickness is set at 8 mm, roughly double the RFM design. The bounds on magnet mass are similarly set to vary between slightly lower and roughly double the RFM design of 0.418 kg. The bounds on magnet

Table XII. AFM parametric variables

	Bounds	Increment	Divisions
Active Axial Length (L_{tot})	30.0 mm Lower 50.0 mm Upper	0.1 mm	201
Magnet Thickness (L_{mag})	4.0 mm Lower 8.0 mm Upper	0.1 mm	41
Magnet Mass (M_{mag})	0.30 kg Lower 0.80 kg Upper	0.025 kg	21
Coil Turns (C_{turns})	6 Lower 24 Upper	1	19
Coil Wraps (C_{wraps})	1 Lower 2 Upper	1	2
Coil Aspect Ratio (C_{ratio})	1 : 1.7 Lower 1.7 : 1 Upper	1.11	2
Coil Gap (C_{gap})	1.0 mm Lower 3.0 mm Upper	0.1 mm	21

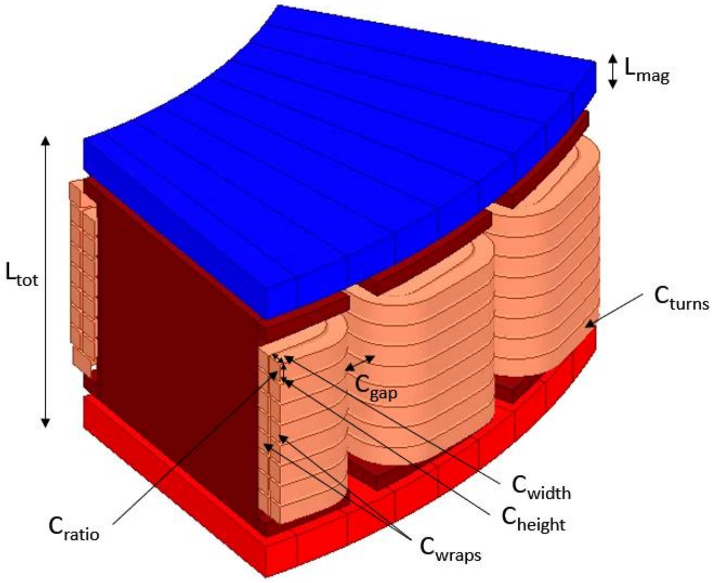

Figure 49. Machine cross-section with variables

length and mass are skewed towards the high end because there is no permeable rotor and also because YASA designs tend to use more permanent magnet material than RFMs due to increased flux path reluctance. Coil turns are the number of turns per stator bar. The coil turn bounds are set at 50 % lower than and 100 % higher than the 12 turns used in NASA's RFM. The relation between coil turns in an RFM versus a YASA is less obvious so a larger range is considered. A maximum of two layers of coil wrap are considered. Generally, the equivalent thermal resistance of the coils increases with extra layers in a YASA and reduces its ability to dissipate heat through any cooling medium. This design is intended to be heat sink cooled, like the RFM, through the housing and so it seemed unlikely that extra layers would be competitive. However, extra layers beyond two were not actively explored and so it is possible that the opposite could be true. As mentioned, profiled Litz wire, by Elektrisola [50] is selected for this design, and so a coil aspect ratio of 1 : 1.7 is chosen to adhere to their specifications of applicable bundle ratios and is referenced as coil width to coil height (C_{width} : C_{height}). The lower coil gap between adjacent coils was chosen based upon the mechanical constraints and tolerances of the machine. The upper bound was chosen to keep the slot fill factor above 40 % and make optimal use of the packaging. Increments are chosen for all variables such that a sufficient range of options can be explored.

An array containing all the possible combinations of variables in Table XII is generated for analysis in a full factorial experiment, resulting in 276,205,356 test cases. The large number of cases is due in part to the increment sizes chosen. These discretizations are selected to avoid missing any ideal combinations. While they can be loosened somewhat, for example to 0.25 mm increments, the machine geometry is highly sensitive to these variables and so it could not be reduced much more than that for a machine of this size, without missing optimal values. While SC mapping is fast, it is not fast enough to process 276 million cases in a reasonable time frame. Many of these (greater than 99.99 %) will produce invalid combinations or insufficient torque. Since the entire geometry is mathematically transcribed, most of these cases can be weeded out quickly through implementation of MATLAB scripting that implements the following constraints:

1. Stator bar inner diameter must be greater than 3 mm
2. Stator bar cross-sectional area can support enough no-load flux linkage for requisite torque without exceeding 1.95 T flux density, average
3. Copper fill factor must not exceed 56.18 %
4. DC copper loss must not exceed 270 W
5. Total active mass must not exceed 2.11 kg, 2.343 kg
6. Torque must not be less than 21.6 Nm, 24 Nm

Constraint 1 comes from the difficulties of bending a thick rectangular conductor around too small of a radius. Constraint 2 reflects the linear nature of the analytical field solution used in the SC mapping. At 1.95 T the relative permeability of Hiperco 50 is around 6000 and is less likely to suffer from the effects of saturation that would reduce solution accuracy. Constraint 3 is selected to not exceed NASA’s final copper fill factor. Constraint 4 is selected to minimize the number of solutions with coil losses that would be too high for an ideal solution at peak load (i.e., Winding loss in the RFM design was

253.8 W). Constraint 5 is selected to not exceed NASA's final machine active mass for the 110 % torque design, and to be 10 % lower for the 90 % mass/volume design. Constraint 6 provides a rough average torque estimate ($T_{avg.\ est.}$) using the following equations.

$$T_{avg.\ est.} = K_t i \tag{29}$$

$$K_t = \frac{C_{turns} N_{bar} K_w \phi_f pp}{\sqrt{2}} \tag{30}$$

$$\phi_f = \alpha_i B_{mg} \frac{\pi}{8pp} (D_o^2 - D_i^2) \tag{31}$$

$$B_{mg} \approx B_{m0} = B_r \left[1 - \exp\left(-\frac{2\pi}{l_a} L_{mag}\right)\right] \frac{\sin\left(\frac{\pi}{n_M}\right)}{\pi n_M} \tag{32}$$

$$l_a = \frac{\pi(D_o + D_i)}{2pp} \tag{33}$$

Where B_r is the remanent flux density, D_o and D_i are the outer and inner stator diameters, n_M is the number of Halbach segments in one pole pair, N_{bar} is the total number of stator bars in the machine, K_w is the winding factor, α_i is the ratio of the average to peak flux density over one pole and is equal to $2/\pi$ for a sinusoidal field from a continuous Halbach array. Equation (32) was used in [6], mainly for coreless AFMs. It predicts the peak flux density at the surface of an axial flux Halbach array (B_{m0}), which is approximate to the middle of the axial airgap flux density (B_{mg}). It tends to underpredict the actual torque in a steel core machine and gets worse with increasing airgap, currently set at 1 mm. Consequently, the requisite torque in constraint 6 is set 10 % lower than required for the two designs to account for this inaccuracy. It is not considered ideal to have to use equations (29) – (33) in this way, but without them the possible AFM design variants are still numbered in the hundreds of thousands. Thus constraint 6 is optional, to be neglected when time permits. Anecdotally comparing results both with and without, its predictive capability is considered to be reasonably consistent for this machine, and its use is considered a trade-off between accuracy and total analysis time, which was reduced by an order of magnitude (approximately 1 day versus 5 days).

After implementing constraints 1 to 6, the total potential combinations reduced to 8409 and 20,008 for the 110 % torque and 90 % mass/volume designs. From here, the SC mapping technique is implemented to analyze the torque of the remaining variants. Figure 50 and Figure 51 compare torque using equations (29) – (33) to the results obtained from SC mapping and shows mainly underprediction from the equations. Note that equation (25) is used to predict the torque using the flux linkage generated via SC mapping. Although fractional slot concentrated windings (FSCW) like the 24-slot, 20-pole configuration used here can produce some exploitable saliency, this is not specified in NASA's original design, so only q-axis current is used. After SC mapping is complete, any design below the cut-off torque is discarded. Designs with average stator bar flux density over 2 T are also discarded. Mostly because this tends to result in excessive core

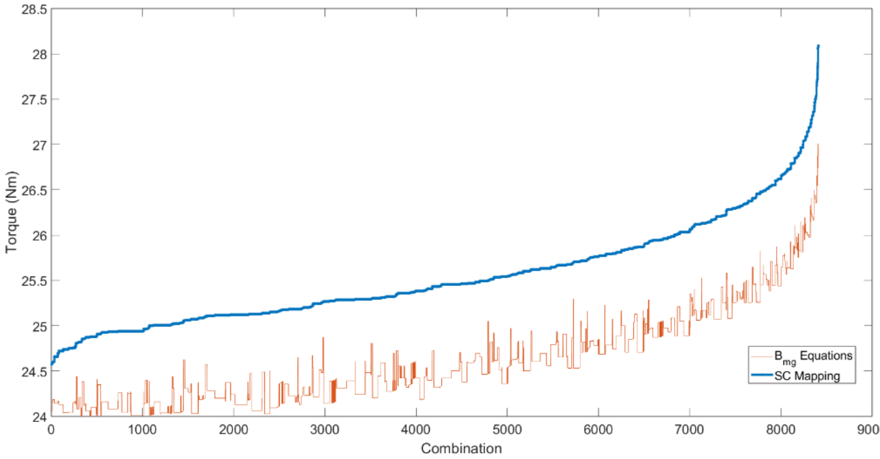

Figure 50. Comparison of the torque estimated from SC mapping and B_{mg} equations for 110 % torque design

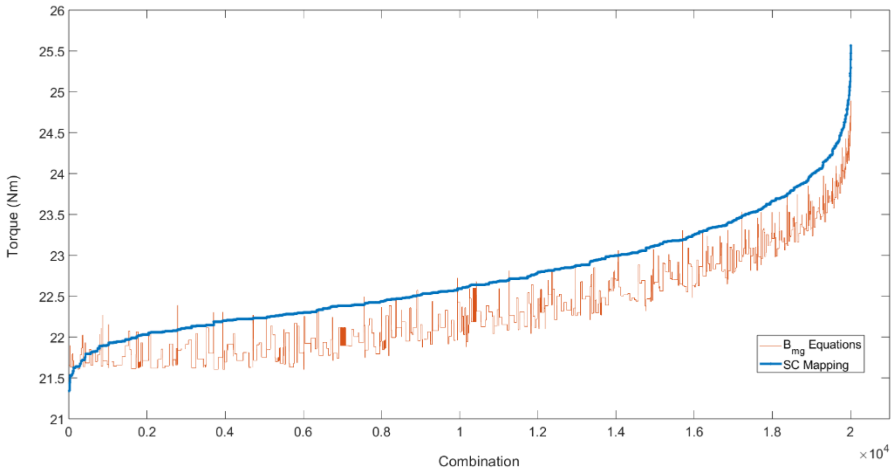

Figure 51. Comparison of the torque estimated from SC mapping and B_{mg} equations for 90 % mass/volume design

loss values at full load and speed. This leaves 673 and 902 combinations for the 110 % torque and 90 % mass/volume designs. The top 20 of each are shown in Table XIII and Table XIV, ordered from lowest to highest (DC) copper loss. For the 90 % mass/volume design, combination 1A is selected because it achieves the requisite torque while possessing the lowest coil loss, which is necessary to minimize total machine losses and prevent overheating. For the 110 % torque design combination 15B is selected, also to minimize loss, but this selection is more of a balance between reducing copper loss and core loss. While the copper loss is somewhat higher than 1B (259 vs. 251 W), its average stator bar flux density is ~0.1T lower, reducing the total machine core loss and offsetting the added copper loss. It also reduces machine saturation and improves torque predictability when the non-linear effects of saturation are accounted for in FEA, minimizing the chance that it will fall below the cut-off torque of 26.4 Nm.

4.4 YASA Results and Comparison

The active components of the chosen configurations 1A and 15B are designed in Siemens NX using the parameters in Table XIII and Table XIV, before being imported into Ansys Maxwell 3D, as seen in Figure 52. The Maxwell FEA is linked to the cad files in Siemens NX, where the design features are controlled parametrically. This allows for

Table XIII. SC mapping results for 90 % mass/volume design

	Torque (Nm)	Flux Density (T)	Copper Loss (W)	Current Density (A/mm^2)	Total Mass (kg)	Copper Mass (kg)	Steel Mass (kg)	L_{tot} (mm)	L_{mag} (mm)	M_{mag} (kg)	C_{turns}	C_{wraps}	C_{ratio}	C_{gap} (mm)
1A	24.02	1.95	253.25	11.07	2.098	0.744	0.729	47.4	6.8	0.625	18	2	0.59	1.5
2A	24.07	1.94	254.41	12.02	2.107	0.632	0.725	45.6	7.8	0.750	16	2	0.59	1.1
3A	24.03	1.93	257.49	12.02	2.093	0.640	0.728	44.6	7.3	0.725	16	2	0.59	1.3
4A	24.15	1.94	257.86	11.51	2.090	0.698	0.717	49.1	7.9	0.675	18	2	0.59	1.1
5A	24.03	1.91	258.30	12.02	2.103	0.642	0.736	44.6	7.3	0.725	16	2	0.59	1.2
6A	24.31	1.95	258.66	11.51	2.092	0.700	0.717	48.9	7.8	0.675	18	2	0.59	1.2
7A	24.15	1.91	258.73	11.51	2.100	0.700	0.725	49.1	7.9	0.675	18	2	0.59	1
8A	24.20	1.95	258.76	12.02	2.096	0.643	0.728	44.4	7.2	0.725	16	2	0.59	1.4
9A	24.05	1.93	258.95	11.07	2.102	0.760	0.742	46.2	6.2	0.600	18	2	0.59	1.7
10A	24.46	1.97	259.52	11.51	2.094	0.702	0.717	48.7	7.7	0.675	18	2	0.59	1.3
11A	24.31	1.93	259.53	11.51	2.102	0.702	0.725	48.9	7.8	0.675	18	2	0.59	1.1
12A	24.20	1.93	259.56	12.02	2.106	0.645	0.736	44.4	7.2	0.725	16	2	0.59	1.3
13A	24.03	1.94	259.78	11.91	2.099	0.646	0.728	44.7	7.3	0.725	16	2	0.59	1.3
14A	24.01	1.93	259.79	11.51	2.071	0.703	0.718	48.1	7.4	0.650	18	2	0.59	1.3
15A	24.15	1.94	259.88	11.42	2.096	0.703	0.717	49.2	7.9	0.675	18	2	0.59	1.1
16A	24.37	1.97	260.09	12.02	2.099	0.646	0.727	44.2	7.1	0.725	16	2	0.59	1.5
17A	24.46	1.95	260.39	11.51	2.104	0.705	0.725	48.7	7.7	0.675	18	2	0.59	1.2
18A	24.63	1.99	260.43	11.51	2.096	0.705	0.716	48.5	7.6	0.675	18	2	0.59	1.4
19A	24.23	1.95	260.55	11.07	2.107	0.765	0.742	46.0	6.1	0.600	18	2	0.59	1.8
20A	24.01	1.91	260.66	11.51	2.081	0.705	0.726	48.1	7.4	0.650	18	2	0.59	1.2

Table XIV. SC mapping results for 110 % torque design

	Torque (Nm)	Flux Density (T)	Copper Loss (W)	Current Density (A/mm^2)	Total Mass (kg)	Copper Mass (kg)	Steel Mass (kg)	L_{tot} (mm)	L_{mag} (mm)	M_{mag} (kg)	C_{turns}	C_{wraps}	C_{ratio}	C_{gap} (mm)
1B	26.55	1.95	250.85	10.66	2.342	0.797	0.820	48.9	7.3	0.725	18	2	0.59	1.8
2B	26.48	1.95	254.15	10.66	2.333	0.807	0.826	47.9	6.8	0.700	18	2	0.59	2.0
3B	26.66	1.96	255.45	10.66	2.338	0.811	0.826	47.7	6.7	0.700	18	2	0.59	2.1
4B	26.48	1.95	256.07	10.58	2.339	0.813	0.826	48.0	6.8	0.700	18	2	0.59	2.0
5B	26.85	1.98	256.82	10.66	2.342	0.816	0.827	47.5	6.6	0.700	18	2	0.59	2.2
6B	26.45	1.94	256.82	11.07	2.310	0.754	0.805	49.6	7.9	0.750	18	2	0.59	1.6
7B	26.45	1.92	257.65	11.07	2.321	0.757	0.814	49.6	7.9	0.750	18	2	0.59	1.5
8B	26.62	1.96	257.67	11.07	2.312	0.757	0.806	49.4	7.8	0.750	18	2	0.59	1.7
9B	26.41	1.93	258.31	10.66	2.329	0.820	0.833	46.9	6.3	0.675	18	2	0.59	2.2
10B	26.45	1.89	258.48	11.07	2.332	0.759	0.822	49.6	7.9	0.750	18	2	0.59	1.4
11B	26.62	1.93	258.50	11.07	2.323	0.759	0.814	49.4	7.8	0.750	18	2	0.59	1.6
12B	26.79	1.97	258.56	11.07	2.315	0.759	0.806	49.2	7.7	0.750	18	2	0.59	1.8
13B	26.45	1.95	258.79	10.99	2.316	0.760	0.806	49.7	7.9	0.750	18	2	0.59	1.6
14B	26.41	1.91	259.10	10.66	2.341	0.823	0.843	46.9	6.3	0.675	18	2	0.59	2.1
15B	26.45	1.87	259.31	11.07	2.342	0.762	0.831	49.6	7.9	0.750	18	2	0.59	1.3
16B	26.62	1.91	259.33	11.07	2.334	0.762	0.823	49.4	7.8	0.750	18	2	0.59	1.5
17B	26.79	1.95	259.39	11.07	2.326	0.762	0.815	49.2	7.7	0.750	18	2	0.59	1.7
18B	26.49	1.95	259.45	11.50	2.326	0.702	0.824	44.7	7.1	0.800	16	2	0.59	1.9
19B	26.96	1.99	259.51	11.07	2.318	0.762	0.806	49.0	7.6	0.750	18	2	0.59	1.9
20B	26.45	1.92	259.63	10.99	2.327	0.762	0.814	49.7	7.9	0.750	18	2	0.59	1.5

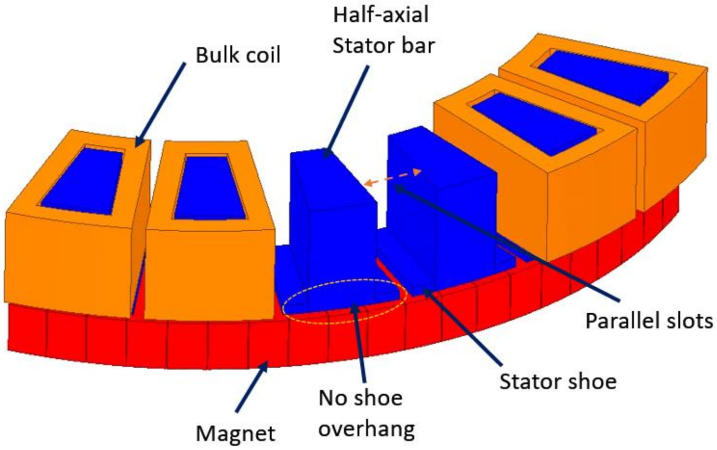

Figure 52. Ansys Maxwell 1/8th YASA HLM, bulk coil geometry

easy adjustment of component sizes and features through the geometry equations developed for analysis. The largest common multiple between the slots and poles combination is 4, which means there is quarter periodicity about its circumference. YASA configurations are also symmetric axially, which allows for a total model reduction to just 1/8th full machine size. This greatly reduces the simulation time.

Two of the coils in Figure 52 are hidden to show the underlying parallel stator slot geometry. Typical AFM designs will use slots that are parallel to the machine radius. This causes the coil sides to be closer together at the ID and further apart at the OD, which produces sub-optimal winding fill factors, determined by the mechanical spacing constraints at the ID of the machine. The design used for the AFMs in this thesis instead implements parallel slots, whereby the coil sides at the ID and OD are equidistant. This optimizes both winding fill factor and stator steel material usage, which puts more material at the OD of the machine where more of the total torque is produced. Some stator skew is introduced through the parallel slot design, but its effect on back EMF, total torque, and torque ripple are considered negligible for this design.

Figure 52 also shows that no stator shoe overhangs at the ID/OD of the machine were used. Shoe overhangs, coupled with an increase of the magnet ID/OD, can work to increase stator bar saturation and thus enhance flux density. They also somewhat shield the coil end turns from the rotating magnet flux field which causes extra coil AC loss. In this AFM design, winding AC loss is already very low due to the transposed litz wire used, and the shoe overhangs take up a non-negligible amount of mass. The improvement to saturation versus material usage was studied for these machines early on and deemed not to be a positive trade, as the extra material is better used elsewhere, for example by increasing the stator bar axial length and providing space for another coil turn.

A bulk coil geometry is initially used in FEA to further reduce the computational burden and create relatively quick estimates (i.e., 3 – 4 hours) for flux and torque. Afterwards, the coils are modeled as annular conductors that more closely reflect the proper cross-sectional area of the design as seen in Figure 53, in order to perform coil AC loss analysis. Note that ANSYS Maxwell's litz wire calculation is used to estimate the AC loss in the coils, similar to the litz wire 2D AC loss analysis during the HLM reconstruction described in Figure 42, except in this case it is for a 3D model. Chamfers are used on the corners instead of fillets to give the solver an easier time of converging and reducing requisite mesh density. The helical pitch of each coil is eliminated for the same reason. The two designs (1A and 15B) are displayed in Figure 54.

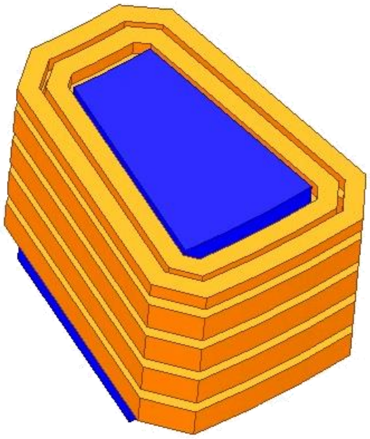

Figure 53. Annular conductor geometry (orange) used for AC loss analysis

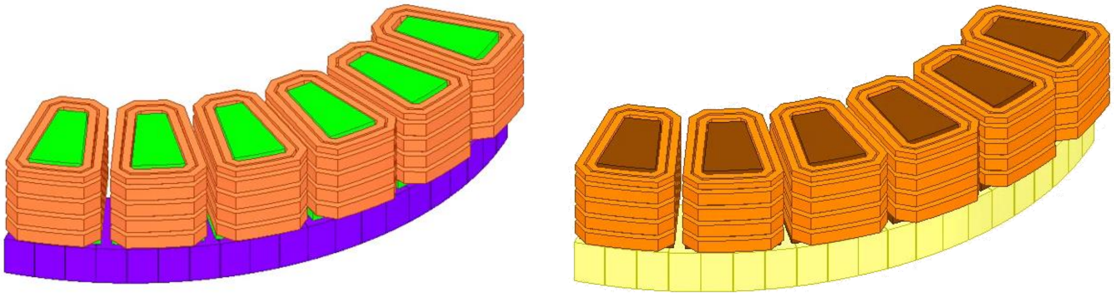

Figure 54. 90 % mass/volume design 1A (left), 110% torque design 15B (right)

Complete dimensions for both can be found in the Appendix. A comparison between the no-load phase A flux linkages over one electrical cycle in Ansys Maxwell and the analytical solution using SC mapping developed in MATLAB are displayed in Figure 55 and Figure 56 and show a close fit for both designs. Consequently, there is a high degree of accuracy when comparing the average torque calculated using equation (25) against FEA. The average torques measured in ANSYS are 26.67 Nm and 24.26 Nm, compared to the 26.45 and 24.02 Nm calculated using SC mapping. This represents an error estimate of less than 1 %. Through experimentation, error values up to 3 % have been observed for other trials when the average no-load flux density is kept below 2 T.

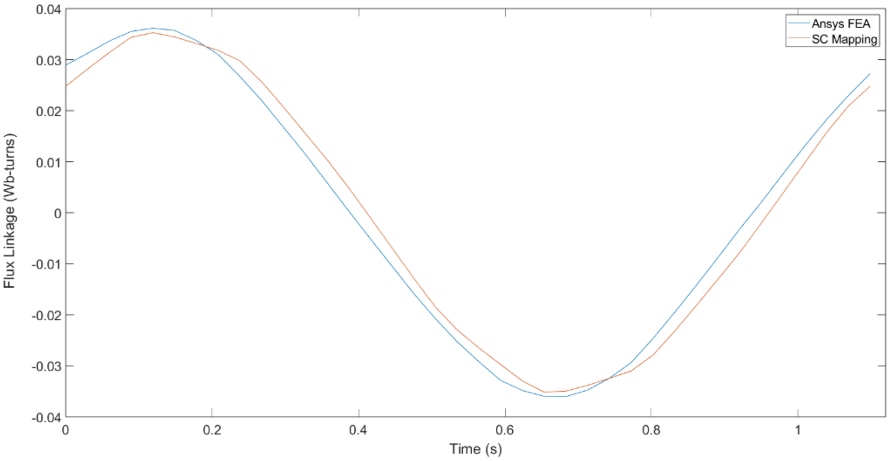

Figure 55. 110 % torque design 15B comparison between analytical SC mapping and Ansys FEA

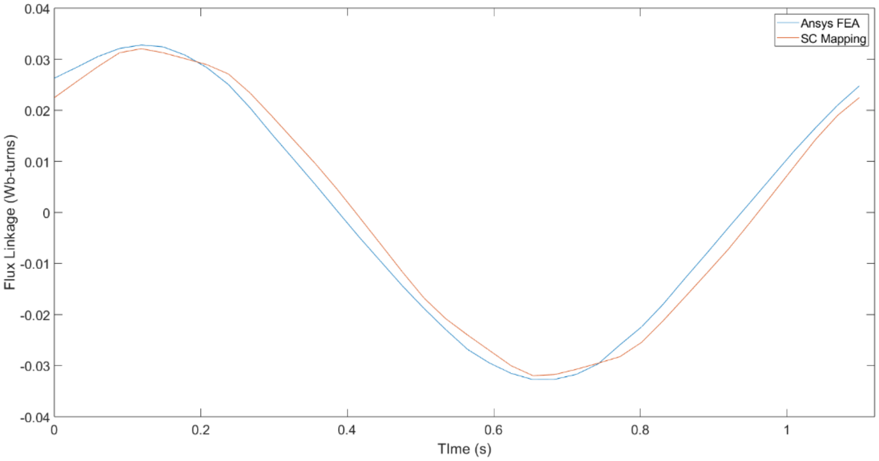

Figure 56. 90 % mass/volume design 1A comparison between analytical SC mapping and Ansys FEA

Table XV compares the time it took to complete each solution, with the analytical estimate being 34 times faster. Both solutions used an 8-core intel i7-9700 processor with 64 GB of RAM. The MATLAB solution is able to make much more efficient use of the multiple cores available due to its parallel processing capabilities. FEA does benefit to a certain extent from multi-core use, but typically depends much more on single-core processing speed. Note that for the full factorial experiment the number of radial sections (described in Section 3.4) were reduced from 7 to 2, and the electrical cycle was halved (thanks to periodicity), in order to reduce the average simulation time even further to under 120 s per iteration, while still retaining reasonable solution accuracy. Table XVI through Table XIX compare the performances of NASA's RFM design to the two AFM concepts chosen. Note that '*' values were not reported by NASA and so were taken from the reconstruction.

Table XV. Comparison of solution time between FEA and analytical

ANSYS Maxwell 3D FEA	7680 s
MATLAB SC Mapping Analytical Equations	224 s

Table XVI. Machine comparison, size and mass

	NASA's RFM	110 % Torque AFM	90 % Mass/Volume AFM
Active Outer Diameter	156.45 mm	152.21 mm	144.18 mm
Active Inner Diameter	111.6 mm	112.28 mm	103.05 mm
Active Axial Length	49.7 mm *	49.6 mm	47.4 mm
Active Volume	19,223 mm^2	19,223 mm^2	17,245 mm^2
Phase Turns	96	144	144
Copper Fill Factor	56.18 %	47.36 %	46.27 %
Coil Fill Factor	63.76 % *	59.20 %	57.83 %
Slot Fill Factor	67.33 % *	62. 89 %	61.45 %
Copper Mass	1.00 kg	0.765 kg	0.747 kg
Stator Steel Mass	0.826 kg	0.833 kg	0.738 kg
Rotor Steel Mass	0.099 kg	0 kg	0 kg
Magnet Mass	0.418 kg	0.735 kg	0.612 kg
Total Mass	2.343 kg	2.333 kg	2.097 kg

In Table XVI, the outer diameter of the 110 % AFM design is comparable to the RFM, when accounting for a requisite extra 2 mm clearance between the end turns and the housing. The 90 % mass/volume AFM diameter is roughly 8 mm smaller (again, including clearance) and produces the specified 10 % reduction in cross-sectional area and volume. Comparing the machines further, it can be seen that both AFMs possess significantly lower copper, coil, and slot fill factors than the RFM design, ranging from 4.4 – 9.9 % lower. Coupled with the segmented nature of the stator bars, this should theoretically make them easier to wind than the RFM, since each bar can be wound independently before full stator assembly. Note that the slot fill is estimated for the AFM designs by assuming a $1/\sqrt{0.8}$ larger conductor size in both width and thickness (i.e., Elektrisola's 80 % litz bundle fill factor). Slot fill for the AFMs assume the same 0.127 mm liner is used on the stator bar and shoe surfaces for insulation as with the RFM. All three designs are relatively comparable in axial length and are assumed to occupy the full 66.04 mm upon mechanical assembly.

The AFMs both possess higher magnet mass than the RFM. For the 90 % mass/volume design it is 46 % higher and for the 110 % torque design it is 75 % higher. This is due, at least in part, to the larger airgap lengths present in the AFMs as compared to RFMs, caused by the lack of a rotor back iron but also from the double airgap that comes with the YASA structure, increasing the flux path reluctance and requiring more magnet material to generate sufficient airgap flux densities. The AFMs also use more turns per phase, 50 % more than the RFM. In addition to the increased airgap length, this is also due to the much smaller airgap cross-sectional area present in the AFM designs that restricts how much flux the airgap can support. This area is around 50 % lower than the RFM design for both AFMs. This limitation is caused mostly by material mass constraints which limit the inner diameter to outer diameter ratios of the two AFM designs to 0.76 – 0.78. This is towards the higher end of optimal ratios for AFM inner/outer diameter combinations which are typically between 0.6 – 0.8. The AFMs make up for this by using less copper but also less cobalt steel (i.e., Stator, rotor steel), which is extremely expensive, much more so than the magnets, and is worth minimizing.

Table XVII demonstrates all three designs have comparable overall efficiency of greater than 93 % at 4400 RPM, 22 Nm, as per the design requirement. This is assuming 50 W of bearing loss for each. Table XVIII shows that all three designs are capable of achieving the 24 Nm torque requirement at 5400 RPM. Torque ripple, though not one of NASA's design constraints, is added for reference to show that it is around 6 – 7 % for each, assuming ideal sinusoidal current waveforms.

Table XVII. Final machine comparison, performance at 4400 RPM

	NASA's RFM	90 % Mass/Volume AFM	110 % Torque AFM
Torque	22 Nm	22.1 Nm	22.1 Nm
Efficiency	96.61 %	96.66 %	96.85 %

Table XVIII. Final machine comparison, performance at 5400 RPM

	NASA’s RFM	90 % Mass/Volume AFM	110 % Torque AFM	
Torque	24 Nm	24 Nm	24 Nm	26.6 Nm
Torque Ripple	7.1 % *	6.7 %	6.0 %	7.0 %
Current	50 A	50 A	45.1 A	50 A
Winding Loss	253.8 W	258 W	210.5 W	264.6
Stator Core Loss	117.6 W	124.2 W	125.4 W	127 W
Rotor Core Loss	3.85 W	0 W	0 W	0 W
Magnet Loss	15.0 W	12.1 W	15.2 W	16.7 W
Total Loss	390.25 W	394.30 W	351.10 W	408.30 W

The total loss for the 90 % mass/volume AFM is on par with the RFM at 24 Nm. The 110 % torque AFM produces lower losses than the RFM at 24 Nm, being 10 % lower, due to the reduced current required. The 110 % torque design, as its namesake suggests, is capable of an additional 10 % torque beyond the requirement (and also consequently what the RFM is capable of) exceeding 26.4 Nm. At 110 % torque the total losses also exceed the RFM by about 5 %, with most of the addition coming from the stator. This may pose thermal challenges during prolonged operation of the machine. While the heat coming from the winding loss travels more easily from encapsulant to the housing in AFMs (since it does not have to pass through slot liner and stator bar) and dissipates faster, the reverse is true for the stator bar core loss, since the bars are no longer connected to a back iron which contacts the housing. Also, there is typically much less contact area between the stator and housing in AFMs, resulting in diminished performance of the housing as a heat sink. While NASA’s thermal simulations suggest the RFM can effectively dissipate 390 W of heat at peak operation, a future thermal analysis is needed to confirm that the AFM can do likewise.

Table XIX demonstrates that all three designs exceed the 22 Nm requirement at max speed and are below the minimum line-to-line voltage of 385 V (i.e., 222 V phase voltage) with each being capable of delivering up to their peak torque. The 90 %

Table XIX. Final machine comparison, performance at 5460 RPM

	NASA's RFM	90 % Mass/Volume AFM	110 % Torque AFM
Torque	24 Nm	24 Nm	26.6 Nm
Phase Voltage	188.4 V *	188.6 V	207 V
Phase Inductance	311 μH *	305 μH	304 μH

mass/volume AFM likely possesses a base speed comparable to the RFM which is around 6100 RPM. The 110 % torque design possesses a much lower base speed, but phase voltage is still 7 % lower than the supply voltage at max speed, which leaves room for tolerance during prototyping. An inductance map was not reported/compiled by NASA and so it was not done for the AFM designs either. It is therefore not clear what the minimum phase inductance is for any design, but it is calculated as being above 300 μH at 5460 RPM for all, which is substantially more than the minimum requirement of 75 μH.

4.5 Summary

This chapter introduced a radial flux surface permanent magnet machine designed by staff at NASA's GRC which is intended for use as a high lift motor for NASA's Maxwell X-57 all-electric plane, capable of achieving up to 24 Nm at 5460 RPM and a peak estimated efficiency of 96.6 %. With an active weight of just 2.34 kg, it has a specific power of 5.64 kW/kg. NASA left the project as open-source with the expectation of further improvement from the public, and so a redesign as an axial flux machine was proposed within this chapter. The RFM was first reconstructed based on details provided by NASA to gain a better understanding of its performance and limitations. Afterwards, two separate designs were targeted with the intention of increasing torque by 10 % in the first design while holding mass, volume and efficiency constant, and decreasing mass and volume by 10 % in the second design while holding torque and efficiency constant. The SC mapping technique was used in a full factorial experiment within MATLAB to quickly analyze a large array of combinations (8000 and 20,000), before settling on two candidates. Cad designs were created for the two machines in Siemens NX and imported into Ansys Maxwell 3D for FEA. The 110 % torque design achieved its torque, mass, and volume targets and while it reduced losses by up to 10 % at requisite 24 Nm torque, at 110 % torque rating it could not stay within the maximum power loss limits reported by NASA's RFM and increased by 5 %. More analysis is needed to confirm if this can be sustained thermally during continuous operation. The 90 % mass/volume AFM design achieved its objectives while performing equivalent to the RFM in terms of torque and efficiency and should be considered a viable candidate for high lift motor redesign as an axial flux machine.

5. Radial Flux Machine Design with Halbach Array for Electric Aircraft

5.1 Introduction to High-Speed Radial Flux Machines for Megawatt Applications

While aircraft have been trending towards increased use of electric machines in various integrated sub-systems for several decades, the potential for an electric propulsion system has taken on an increased sense of urgency with the plight of global warming and the aim of reducing green-house gas emissions. Most of the developments to date have been on relatively small electric aircraft designed to fill the role of air taxis due to present limitations in the electric powertrain systems that make scaling up difficult, particularly the low energy density in batteries. However, there is a growing need for advances in high power electric machine packaging as well. NASA's advanced air transportation technologies (AATT) project identified the need for Megawatt-class electric machines capable of specific power ratings not yet commercially available but are expected to be achieved in the near future for advanced hybrid and full-electric aircraft. Such example architectures include the single aisle turbo-electric aircraft concept (STARC-ABL), which calls for a scalable electric motor with a specific power of 13.2 kW/kg and efficiency of 96 % that could be used to propel a 19-passenger fully electric aircraft as well as up to 150-passenger hybrid aircraft, depending on the quantity, power rating and configuration of machines [51]. This specific power is over twice as much as the Siemens SP260D as seen in Figure 57, an electric motor with one of the highest specific power ratings used commercially in aerospace to date, and over six times as much as a typical electric road vehicle. The United Technology Research Center/Rolls-Royce hybrid-geared turbofan (HGTF) concept architecture calls for similarly high specific power megawatt machines [52].

To address the current gap in electric machine technology and improve the state of the art, there are numerous prototypes in various stages of testing today. These include high temperature superconductor (HTS) machines and non-HTS machines. HTS

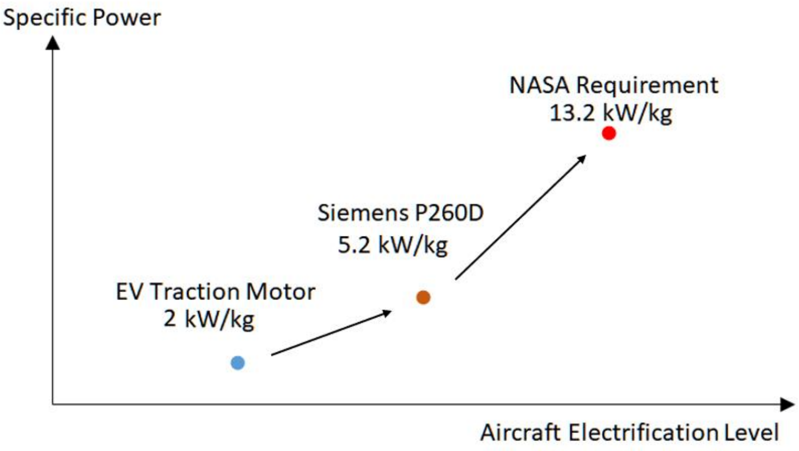

Figure 57. Electric machine specific power [53]

machines, while a promising technology capable of delivering very high specific powers, are still an active area of development. Their deployment typically requires cryogenic refrigeration systems that increase overall system mass, complexity, cost, and reduce operational reliability. NASA's N3-X hybrid-wing-body turboelectric distributed propulsion is one such concept architecture that deploys superconducting motors and generators [54].

Non-HTS machines are a much more mature field of technology that are considered capable of reaching the required power densities for aerospace in the near term. Within the non-HTS hierarchy there are both high speed and low speed machines. Low speed machines produce higher torque levels to achieve power output objectives which typically means higher stator excitations. This typically results in the need for stronger, thicker components to support the torsional stress along with increased heat rejection coolant systems. The 2.7 MW ring induction motor in development by NASA and Ohio State University is an example of a low speed (2500 RPM) megawatt machine used for NASA's hybrid gas electric propulsion (HGEP) architecture concept [55].

High-speed machines, in contrast, can be lighter and more compact, increasing overall system power densities, although a considerable part of the mass reduction may be lost due to mechanical transmission complexity increase when a gearbox is required. To date, there are three such high-speed motor projects that are in prototype testing. These include a 1 MW machine developed by Honeywell, a 4 MW machine developed by University of Nottingham and Rolls-Royce, and 1 MW machine developed by the University of Illinois and NASA. The specifications of these machines are documented in Table XX. The closest project to reaching its target objectives appears to be Honeywell's, which has a technology readiness level of 6 (i.e., full system prototype demonstration) out of 9. Their wound field synchronous (WFS) machine, while groundbreaking in terms of specific power for WFS technology, is much lower than either of the other two projects, and WFS high speed megawatt machines have many decades worth of pre-existing prototype development to draw from, in contrast to the other projects. This includes development at least as far back as 1979, with the prototyping of a 14 KRPM, 2.5 MW

Table XX. Select high speed megawatt machines for aerospace applications [56]–[60]

Organization	University of Illinois/NASA	Honeywell	University of Nottingham/Rolls-Royce
Nominal Speed (RPM)	15,000	19,000	15,000
Max Power (MW)	1	1	4
Phases	3	6	3 x 8
Type	Air Core Permanent Magnet, Outer Rotor	Wound Field Synchronous	Surface Permanent Magnet, Inner Rotor
Coolant	Forced Air	Oil conduction and spray	Oil stator flooding
Specific Power (kw/kg)	14.4	7.9	17.3
Most Recent Test (MW)	N/A	0.9	0.126

WFS generator by Aeroject Electrosystems for Westinghouse Electric, which was to be used for helicopter propulsion applications and had a specific power of 3.7 kW/kg [61]. In 2011, a WFS generator was developed by Electrodynamics Associates for the United States Air Force that reached 2.5 MW peak, 1.2 MW continuous with a specific power of 14.1 and 6.8 kW/kg respectively, and was targeted towards directed energy weapon applications [62], [63]. Because of this history, the relatively low specific power target, and the general robustness of working with WFS technology [64] it is anticipated that Honeywell's machine will reach commercial availability sooner than its counterparts.

It is also worth mentioning that the list of companies currently investigating highspeed megawatt aerospace propulsion applications is not limited to the three aforementioned prototypes, just that the details of their projects are mostly confidential at this time. For example, there are projects by Collins-Aerospace/Pratt & Whitney, as well as General Electric with as yet undisclosed speed ratings and machine topologies [65], [66] that will likely be unveiled in the near future. There is also another 2.5 MW generator under development by Rolls-Royce which was initially part of the E-Fan X project before its cancellation (and is now acting as a stand-alone project) that has already achieved 1 MW during testing [67].

5.1.1 Initial Proof of Concept Prototype Specifications

Typical project budgets for designing aerospace machines can be astronomical. Researchers at McMaster University have been tasked with designing a high-speed megawatt machine for aerospace applications with a relatively modest specific power target (considering NASA's future roadmap, see Figure 57) of 7 kW/kg and low thermal rating to keep the costs grounded. In anticipation of the lengthy development time, expense, and test facility limitations associated with the creation of a megawatt machine, a scaled down proof-of-concept has been proposed that can demonstrate core technologies required to achieve targeted speed, specific power and thermal regulation. The initial project specifications for a surface permanent magnet (SPM) prototype that can effectively do this are listed in Table XXI. NO18 grade silicon steel is selected for

Table XXI. Initial prototype specifications

Speed	20,000 RPM
Phase Voltage	750 V
Phases	3
Maximum Winding Temperature	180 $^{\circ}C$
Maximum Lamination Temperature	180 $^{\circ}C$
Maximum Magnet Temperature	150 $^{\circ}C$
Continuous Mechanical Power	100 kW
Peak Mechanical Power	150 kW
Machine Specific Power	7 kW/kg
Maximum Current Density	17.5 A/mm^2
Maximum Slot Fill Factor	50 %
Rotor Configuration	SPM

stator and rotor laminations due to its excellent permeability and core loss characteristics, while N40EH magnet grade is selected due to its ability to withstand the relatively high temperatures required. The speed and specific power requirements are most similar to electric machines used in NASA's subsonic ultra green aircraft research project (SUGAR-volt) which employs 1.3 MW machines in the range of 3-5 kW/kg at speeds of 13 KRPM for a parallel hybrid (gas/battery) aircraft concept [68]. A system diagram example of this architecture is displayed in Figure 58, where the battery-motor combination supplement pre-existing turbofan-fuel capabilities. While several machine configurations were initially considered for McMaster University's project, two in particular were singled out for further analysis. These include a 12/10 outer rotor and 36/6 inner rotor surface permanent magnet machine. Ansys Motor-CAD coupled electromagnetic and thermal simulations are used for preliminary study, which implement an intuitive parameterized motor model interface front-end, coupled with a 2D fast finite element analysis and lumped parameter thermal network back-end for the two domains, respectively. Elsewhere, for more detailed analysis and customized geometries, non-coupled Ansys Maxwell electromagnetic FEA is used.

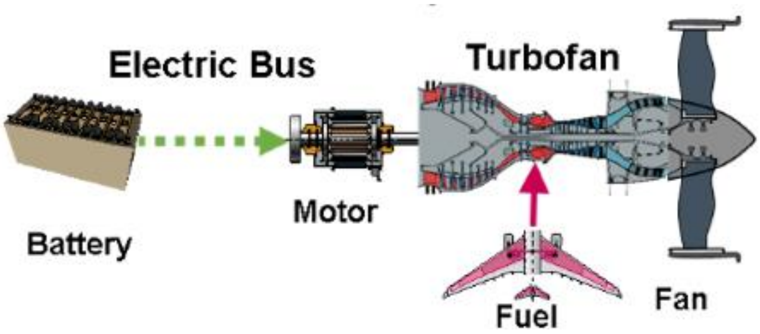

Figure 58. Parallel hybrid aircraft architecture [69]

5.2 Outer Rotor Design

The design of the outer rotor machine is diagramed in Figure 59 and Figure 60.

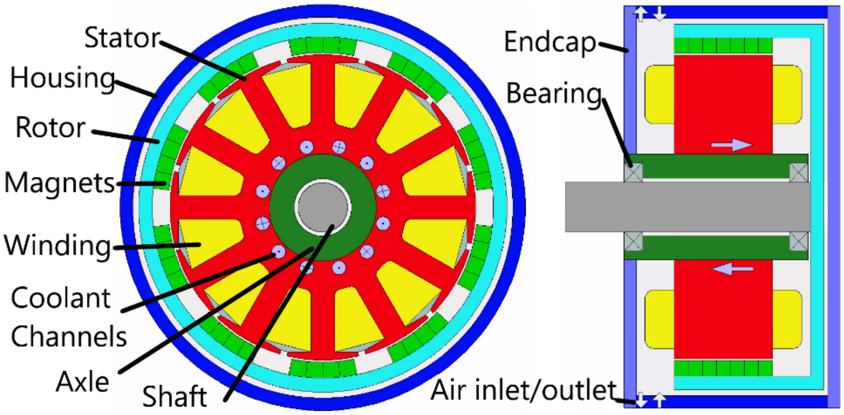

Figure 59. 12/10 outer rotor configuration top view (left), side view (right)

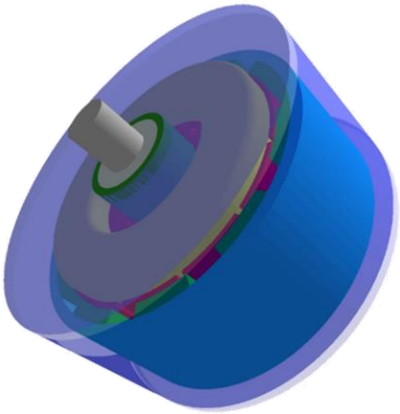

Figure 60. 12/10 outer rotor configuration 3D view with transparent housing

The machine dimensions of the outer rotor configuration are listed in Table XXII. The concept consists of 12 stator slots and 10 magnet poles. This is a fairly common configuration for a fractional slot concentrated winding machine that adheres to the $N_s = 2pp \pm 2$ rule (N_s being number of stator slots, 2pp being total magnet poles) that is recommended to avoid unbalanced magnetic forces as well as keep the magneto motive force (MMF) harmonics low [70]. The main advantage of this topology is the reduced end turn lengths that come from the fractional slot concentrated winding configuration which minimizes total resistive loss in the stator coils. It also has a relatively small airgap due to the retainer being on the outer rotor diameter (not shown) instead of the magnet face. The magnets form a regular North-South polar array but are segmented both axially and radially to a high degree in order to lower the magnet eddy current losses. The machine's winding specifications are listed in Table XXIII, with a winding schematic shown in Figure 61. A 16 AWG conductor was selected as a starting point, with suitable insulation thicknesses chosen to avoid partial voltage discharge. A single layer winding is selected to relax the insulation requirements for the relatively high operating voltage, and also to maximize the fundamental winding factor. The windings are fully encapsulated. Note that

Table XXII. 12/10 outer rotor machine dimensions

Stack Length	50 mm
Rotor OD	186 mm
Rotor ID	172.2 mm
Magnet Thickness	8 mm
Mechanical Air Gap	1 mm
Stator Yoke Thickness	15.1 mm
Stator Tooth Width	12 mm
Shoe Thickness	2 mm
Magnet Pole Arc Angle	115 eDeg
Slot Fill factor	49.6 %
Active Mass	7.64 kg

Table XXIII. 12/10 outer rotor winding specifications

Wire slot fill	49.6 %
End Winding Fill	45.9 %
Liner Thickness	0.2 mm
Number of Turns Per Coil	25
Number of Strands Per Coil	6
Wire Diameter	1.29 mm
Wire Insulation Thickness	0.1 mm
Double/Single Layer	Single
Connection Style	Series
Fundamental Winding Factor	0.966

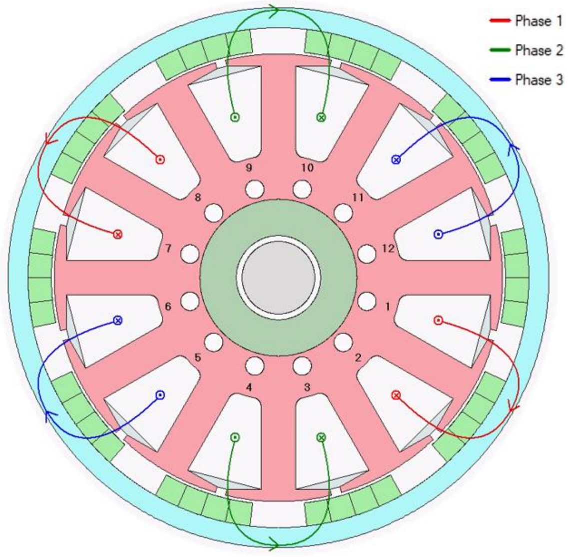

Figure 61. 12/10 outer rotor winding schematic

slot fill factor is taken to include slot liner, insulation, copper cross-section and slot wedge.

5.2.1 Outer Rotor Electromagnetic Performance

The continuous electromagnetic performance results of the 12/10 configuration are analyzed using Ansys Motor-CAD and are displayed in Table XXIV.

Table XXIV. 12/10 outer rotor machine electromagnetic performance

Torque	47.8 Nm
Speed	20,000 RPM
Torque Ripple	11.3 %
Power	100.1 kW
Phase Current	93 A_{RMS}
Phase Voltage	618 V
Magnet Loss	320W
Stator Iron Loss	1108 W
Rotor Iron Loss	49 W
DC Copper Loss	891 W
Total Loss	2368 W
Electromagnetic Specific Power	13.1 kW/kg

It is notable that while the DC loss is kept low in this design due to shorter end turn lengths, the permanent magnet loss is comparably high due to several factors. First is the stator FSCW creating asynchronous sub-harmonics relative to the rotor, which are 0.26 and 0.71 at 2/5th and 3/5th of the fundamental frequency, respectively. Second is the slotting effect from the stator slots due to relatively close proximity of the magnets to the stator coils. Third is the high fundamental frequency of operation (which exceeds 1.6 kHz) that amplifies the stator and rotor losses, causing excess eddy and hysteresis losses.

5.2.2 Outer Rotor Thermal Performance

The coolant system for the outer rotor machine consists of hybrid forced air and liquid coolant. For the liquid cooling, series connected 6.35 mm (1/4 in.) copper pipes that snake through the stator back iron are used. This is similar in design to 2002 patent US6819016B2 filed by TM4. The main difference being that the pipes are only partially embedded in the TM4 concept, as seen in Figure 62. This is presumably for easier insertion and removal since the pipe can almost be entirely formed prior to insertion into the stator core and requires only mild work thereafter to fit it into place. The coolant

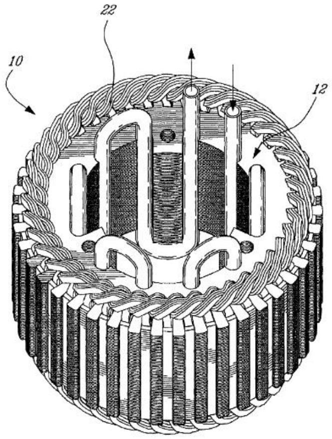

Figure 62. TM4 Patent US6819016B2 liquid cooling arrangment for electric machines concept [71]

channels are balanced to keep the pressure losses in the ~10 PSI range so as to limit the pump requirements, as well as to keep the flow type turbulent, but close to a rule-of-thumb 5 m/s maximum flow speed. Natural convection off the outer housing is assumed.

Ambient temperature, coolant inlet temperature, and coolant flow rate are all chosen as values typical for this application and represent upper limits. For air cooling, a centrifugal fan (not shown) is assumed to ventilate air in the end turn region on the exposed shaft end side. Air flow rate is estimated by comparison with the NASA 1 MW outer rotor configuration mentioned in Table XX which is cooled solely via centrifugal fan. Using the affinity laws where q, d, and N are flow rate, fan diameter and rotational speed,

$$\frac{q_1}{q_2} = \left(\frac{N_1}{N_2}\right)\left(\frac{d_1}{d_2}\right)^3 \tag{34}$$

With q_1, d_1, N_1 being 11,326 L/min, 31.76 cm, 18,000 rpm for the NASA outer rotor [72], and d_2, N_2 being 18.6 cm and 20,000 rpm for this outer rotor concept. q_2 is found to be 2528 L/min. A conservative initial estimate of half this value is applied and assumed to be 1250 L/min since both forced air and liquid cooling is used to cool this machine, in contrast to NASA’s, which needs more forced air to achieve adequate cooling.

Using the electromagnetic losses from Table XXIV, the thermal performance of the machine is analyzed in ANSYS Motor-CAD and is listed in Table XXV. Note that the electromagnetic and thermal performance were iterated upon until convergence within 1 % was achieved between the two domains.

The maximum coil temperature is 200 °C and the magnets are 157 °C. These temperatures exceed the initial specifications listed Table XXI. The coil insulation would have to be upgraded to type K or higher. A more detailed analysis would have to be performed on the magnets to assess the degree of demagnetization, and how detrimental to performance it is.

5.3 Inner Rotor Design

The design of the inner rotor machine is diagramed in Figure 63 and Figure 64.

Table XXV. 12/10 outer rotor machine thermal performance.

Coolant Inlet Temperature	65 °C
Ambient Temperature	40 °C
Coolant Flow Rate	10 L/min
End Turn Ventilation	1250 L/min
Maximum Coil Temperature	200 °C
Average Coil Temperature	178 °C
Magnet Temperature	157 °C
Coolant Outlet Temperature	67 °C
Maximum Stator Lamination Temperature	182 °C
Maximum Rotor Lamination Temperature	160 °C
Coolant Pressure	15 PSI

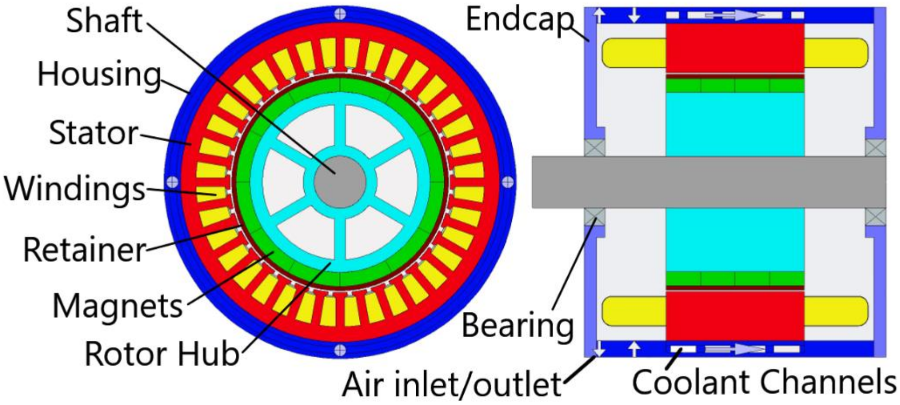

Figure 63. 36/6 inner rotor configuration top view (left), side view (right)

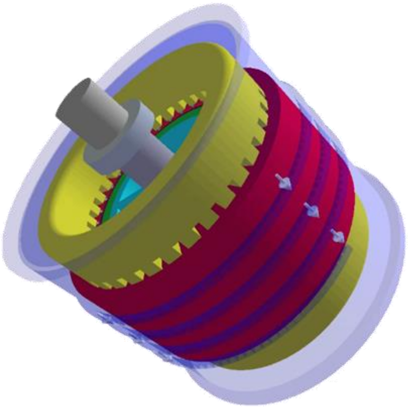

Figure 64. 36/6 inner rotor configuration 3D view with transparent housing

It consists of 36 stator slots and 6 rotor poles with a distributed winding configuration. The main advantage of this winding is a strongly sinusoidal back EMF which serves to reduce higher order harmonics and related losses, especially in the magnets. The low pole count is also particularly advantageous in this situation due to the high rotational speed. Fewer poles mean a lower fundamental frequency (1 kHz) which serves to reduce AC-related losses. The inner rotor machine's dimensions can be seen in Table XXVI. The winding specifications are listed in Table XXVII, with a winding

Table XXVI. 36/6 inner rotor machine dimensions

Stack Length	80 mm
Rotor OD	104 mm
Rotor ID	92 mm
Magnet Thickness	8 mm
Mechanical Air Gap	1 mm
Stator OD	183.6 mm
Stator Tooth Width	5 mm
Shoe Thickness	2 mm
Retainer Thickness	2.5mm
Magnet Pole Arc Angle	180 eDeg
Slot Fill factor	48 %
Active Mass	11.61 kg

schematic shown in Figure 65. Similar wire gage and insulation thicknesses from the outer rotor concept were selected for comparison. The windings are fully encapsulated. Note that the end winding axial height was determined to keep the end winding fill factor at or below the wire slot fill factor in this case.

Table XXVII. 36/6 inner rotor winding specifications

Wire slot fill	48.4 %
End Winding Fill	48.3 %
Liner Thickness	0.2 mm
Number of Turns Per Coil	7
Number of Strands Per Coil	5
Wire Diameter	1.29 mm
Wire Insulation Thickness	0.1 mm
Double/Single Layer	Single
Connection Style	Series
Fundamental Winding Factor	0.966

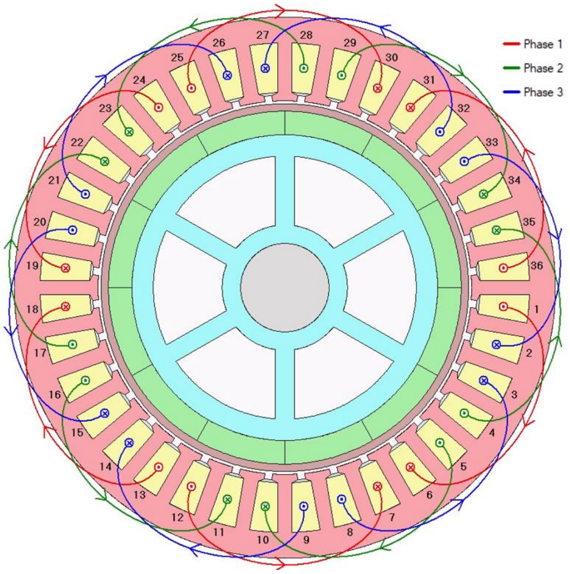

Figure 65. 36/6 inner rotor winding schematic

5.3.1 Inner Rotor Electromagnetic Performance

The inner rotor machine's electromagnetic performance was assessed using Ansys Motor-CAD and can be seen in Table XXVIII. The airgap width of the inner rotor

Table XXVIII. 36/6 inner rotor machine electromagnetic performance

Torque	47.2 Nm
Speed	20,000 RPM
Torque Ripple	8.0 %
Power	98.9 kW
Phase Current	77 A_{RMS}
Phase Voltage	655 V
Magnet Loss	16 W
Stator Iron Loss	1078 W
Rotor Iron Loss	3 W
DC Copper Loss	1166 W
Total Loss	2263 W
Electromagnetic Specific Power	8.6 kW/kg

machine required for the magnet retainer is much larger than the outer rotor and the rotor diameter much smaller, both of which contribute to a reduced torque. So too does the low pole count. To overcome this, in addition to the increased axial length, the magnets are arranged into a 4-segment (per pole pair) Halbach array to strengthen the airgap flux density. The array occupies the full circumference of the rotor, in contrast to the outer rotor design which uses around half the magnet material. In total, the inner rotor configuration's active mass is greater by ~50%, which lowers the specific power substantially.

5.3.2 Inner Rotor Thermal Performance

The coolant system for the inner rotor configuration makes use of a helical water jacket that dissipates stator heat through conduction. This is a fairly common method of cooling that has been employed extensively in the automotive industry and has the potential for greater uptake in the nascent electric aircraft aerospace industry as well.

In contrast to the outer rotor design, the inner rotor's water jacket is embedded in the aluminum housing of the machine, rather than the stator back iron. Also, the large diameter of the housing generally means that a greater active cooling area can be achieved with the inner rotor design and thus cool the machine more effectively. End turn ventilation flow rate was estimated using affinity laws in equation (34), similar to the outer rotor machine for consistency.

The thermal performance of the inner rotor design was assessed using Motor-CAD and is displayed in Table XXIX. Note that the electromagnetic and thermal performance were iterated upon until convergence within 1 % was achieved between the two domains. When compared against the outer rotor's thermal performance, the inner rotor design's losses are primarily constrained to the stator with very low rotor loss, which makes for much more effective heat dissipation through conduction to a stator water jacket. By consequence the lamination and magnet temperatures are significantly lower in the inner rotor design. Type H insulation is suitable for the maximum temperature of 162 °C that the coils see.

Table XXIX. 36/6 inner rotor machine thermal performance

Coolant Inlet Temperature	65 $°C$
Ambient Temperature	40 $°C$
Flow Rate	10 L/min
End Turn Ventilation	381 L/min
Maximum Coil Temperature	162 $°C$
Average Coil Temperature	150 $°C$
Magnet Temperature	112 $°C$
Coolant Outlet Temperature	68 $°C$
Maximum Stator Lamination Temperature	141 $°C$
Maximum Rotor Lamination Temperature	125 $°C$
Coolant Pressure	7 PSI

5.4 Chosen Configuration

The high-speed outer rotor concept has significant limitations from mechanical, electromagnetic, and thermal perspectives that make it difficult to design and operate. The rotor is supported at a single fixed end of the shaft, as seen in the simplified view in Figure 66, and by consequence its rotor, often called a ‘bell’ or ‘cup’ due to its shape, is cantilevered by the electromagnetic and centrifugal forces which act on it, especially near the magnets, during regular operation.

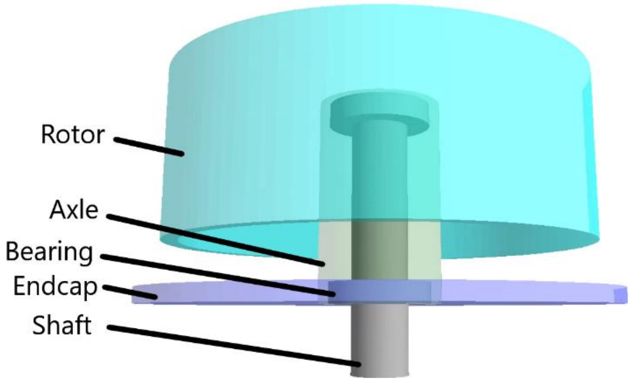

Figure 66. Simplified 3D view of outer rotor concept detailing single support

This is a common configuration for outer rotor radial flux machines that works well at low speeds for motors of this size. For high-speed operation it is typically relegated to fractional horsepower motors where magnetic and centrifugal forces are relatively small. At 20 KRPM and 100+ kW power output, the forces acting on such a rotor are far too great for typical steels to withstand and require significant reinforcement on the outer diameter. Typical reinforcement materials include composite fiber wraps and/or titanium. A 6 mm gap is left in the model between the rotor and the housing to allow for such reinforcement, as well as rotational clearance. It is notable that such reinforcement adversely affects heat transfer from the machine to the ambient environment due to poor material thermal conductivity and generally increases rotor heating.

Alternative designs make use of triple-bearing arrangements such as that used for NASA’s 60 kW propulsion motor on the SCEPTOR electric aircraft project [42] which supports the entire rotor and prevents cantilevering. A general example of this is shown in Figure 67, which demonstrates a triple supported rotor/stator which acts to reduce the cantilevering effects inherent to single support designs.

There are numerous drawbacks associated with such a configuration however, many of which are related to the large diameter bearing 3 which usually scales with the motor radius and can see very high losses that act to restrict the maximum speed. There is a limited market for motor bearings that can withstand speeds of 20,000 rpm in general.

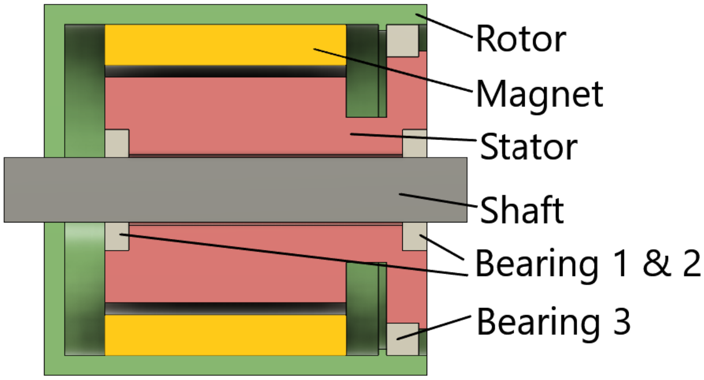

Figure 67. Triple bearing outer rotor diagram

For a large diameter bearing, high speed operational requirements can be prohibitively expensive. Bearing 3's diameter also restricts access points for a stator water jacket, which is the easiest method of liquid cooling outer rotor machines. Any coolant channels must run through the stator yoke and exit between bearing 1 and 3. The triple bearing configuration also does nothing to reduce the centrifugal forces that the rotor sees, and so outer diameter rotor reinforcement is still required for high-speed operation.

Electromagnetically and thermally speaking, it is quite challenging to minimize the losses in the outer rotor design, to the point where temperatures stay below the specified limits. A cooling circuit in the stator backiron proved insufficient to keep the end turns and magnets sufficiently cool. It is possible that the overall machine diameter could be increased, allowing for more copper cross-section in the slots and thereby lower coil losses, but this would not solve the high magnet loss, and the rotor tip speed already approaches 200 m/s (i.e., Mach 0.6), beyond which rotor stress and windage losses (not yet considered) generally become very difficult to manage. Instead, the coil loss could be reduced through increasing stack length and lowering the current, but at peak operation the phase voltage would exceed the 750 V requirement. While the outer rotor configuration could certainly be improved further, it is not immediately obvious as to how the electromagnetic/thermal limitations can be addressed, and it may be the case that the 12/10 slot/pole selection is not the ideal topology for such a machine.

The inner rotor configuration, in contrast, is much easier to implement as a high-speed machine than an outer rotor. This is for several reasons: The first is that the bearing inner diameter only needs to be as large as the shaft diameter and does not have to support a coolant circuit pass-through, making bearings cheaper and easier to source. The rotor is also doubly supported by default and therefore presents a lower risk of dangerous vibration. The rotor's diameter is also much smaller in the inner rotor configuration, with the mass being contained much closer to the center of rotation. This means that the centrifugal loading of the machine is much lower, especially in the event of a dynamic eccentricity, and so the rotor hub can be made out of regular electrical steels instead of titanium while the shaft diameter also shrinks. High speed inner rotor machines have existed for many decades and by consequence there are more resources to build one and a larger knowledge base to work with, in general. Even today's automotive traction motors routinely achieve top speeds in excess of 10,000 rpm, with Tesla's Model S traction motors capable of reaching 16,000 RPM [73] for 2012 induction motor models and is supposed to exceed 20,000 RPM for newer S Plaid interior permanent magnet motor models [74]. It is for these reasons, coupled with the much lower rotor/stator temperatures observed in the electromagnetic and thermal simulations, that an inner rotor machine is selected for further detailed analysis and prototyping.

5.5 Optimization of Radial Flux Halbach Array

5.5.1 Four, Eight, and Variable Arc Halbach Array Case Study

Several magnet configurations are analyzed in order to maximize the machine's specific power. These include 4-segment (per pole-pair) Halbach arrays (henceforth referred to as just 4-segment) with either radial or parallel magnetizations, 8-segment Halbach arrays (aka 8-segment), and variable arc 4-segment Halbach arrays (aka variable arc). These four configurations are diagramed in Figure 68. Two dimensional, 1/6th periodic models are implemented to simplify solution complexity and reduce simulation times in Ansys Maxwell.

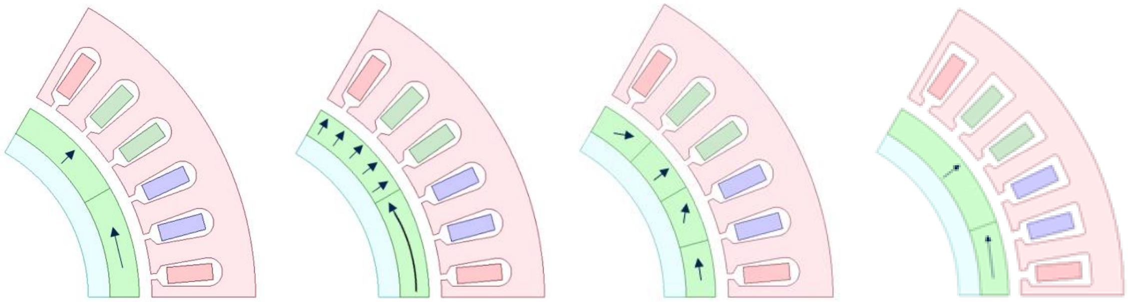

Figure 68. From left to right: 4-segment array (parallel), 4-segment array (radial), 8-segment array, variable arc array

The 4-segment array has magnets that alternate magnetic orientations by 90-degree increments. The 4-segment parallel magnetization represents the default design used for the inner rotor configuration results presented previously. Its orientations are constant and are radial or tangential to the magnet's curvature only at the magnet center of mass. The 4-segment radial magnetization possesses orientations that are changing, being everywhere radial or tangential with the magnet curvature. Note that 8-segment and variable arc arrays are also parallel magnetized, the extra suffix being dropped for brevity. The 8-segment array alternates by 45-degree increments. As was true for the axial flux Halbach array, the fundamental component of flux density increases (but with diminishing returns) for radial flux Halbach arrays that approach a continuous sinusoidal Halbach ring.

The 8-segment array is closer to a pure sinusoid than the 4-segment and should thus produce higher levels of fundamental flux density and torque. The variable arc array alternates by 90-degree increments, but the radial orientation magnet is larger than the tangential orientation magnet. For the variable arc Halbach array there is literature suggesting that 4-segment magnetized Halbachs with rotor back irons can be optimized by varying the arc angles of radial and tangential magnets in order to maximize torque output [75]. To assess this effect for parallel magnetized 4-segment Halbachs, a parametric study is run in which the radial magnet's effective arc angle (α_s) is varied from 15 to 165 electrical degrees. The setup is displayed in Figure 69. The total angle of the pole (θ) is fixed at 180 electrical degrees. Thus, the arc angle of the tangential magnet

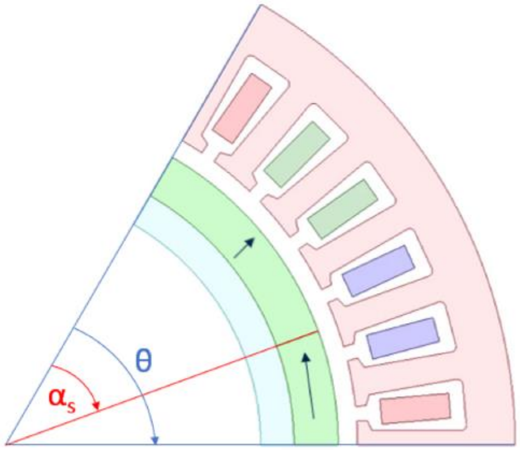

Figure 69. Parametrized angles of variable arc array

increases or decreases to accommodate the change in radial magnet. The results of the torque, torque ripple, and magnet loss are displayed in Figure 70 and Figure 71. The torque is shown to peak at an angle of 120 electrical degrees. The torque ripple, as measured in percentage, has several local minima that vary with arc angle, with the global

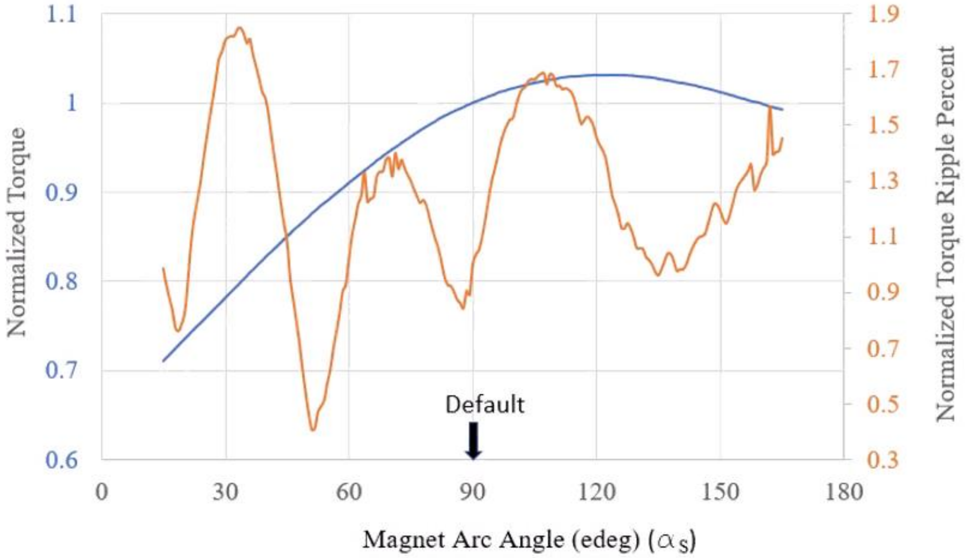

Figure 70. Variable arch Halbach parametric study, torque and torque ripple versus electrical arc angle

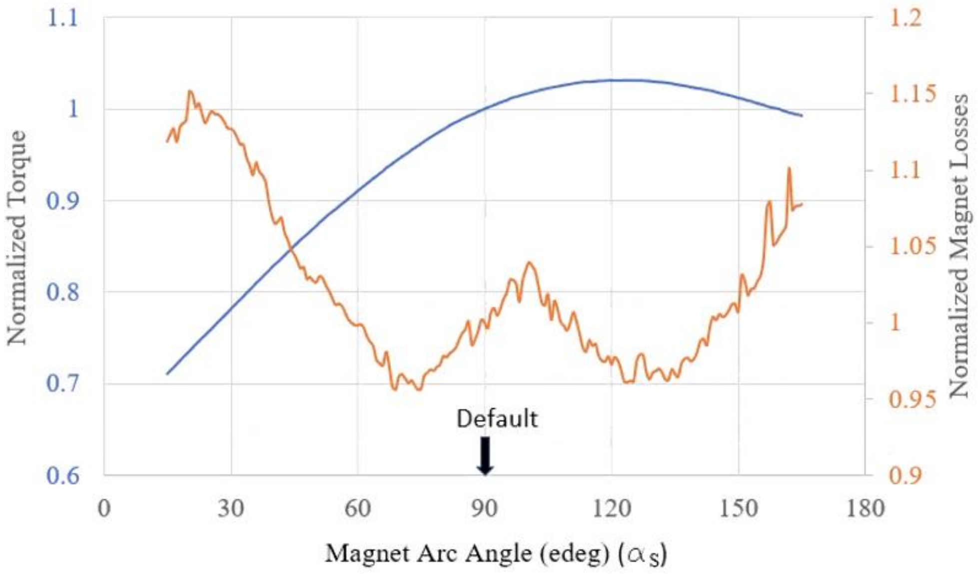

Figure 71. Variable arc Halbach parametric study, torque and magnet loss versus electrical arc angle

minimum occurring at 51 electrical degrees. The magnet losses are shown to reach a minimum at 74 electrical degrees. Thus, the torque, torque ripple and magnet loss have different angles at which their performance is optimized when using a variable arc Halbach. A radial arc angle of 135 electrical degrees is selected as the ideal angle for α_s. It has torque performance close to the theoretical maximum, magnet loss close to the theoretical minimum, and its torque ripple is close to a local minimum and far from the global maximum. Electromagnetic performance results for each potential array are displayed in Table XXX. Note that for this study, magnet temperatures are fixed at 100 °C, while coil temperatures are fixed at 150 $°C$. The 4-segment radial Halbach array possesses both lower torque and higher percentage torque ripple than the baseline parallel array and is thus dropped from consideration. The 8-segment array and variable arc array both possesses higher torque output than baseline and percentage torque ripple below baseline. The variable arc array possesses slightly higher torque, while the 8-segment possesses slightly lower torque ripple. This can be explained by examining the no-load flux density at the stator bores for each array in Figure 72. As can be observed, the 8-segment Halbach array flux density is more sinusoidal than any other array. The variable

Table XXX. Halbach array electromagnetic performances

	4-Segment Radial	4-Segment Parallel	Variable Arc	8-Segment
Torque (Nm)	47.0	48.8	50.2	49.6
Speed (RPM)	20,000			
Torque Ripple (%)	10.7	8.92	8.60	6.23
Power (kW)	98.4	102.2	105.1	103.9
Phase Current (A_{RMS})	77			
Phase Voltage (V_{peak})	642	664	678	675
Magnet Loss (W)	50	50	48	44
Stator Iron Loss (W)	862	885	912	890
Rotor Iron Loss (W)	0			
DC Loss	1175			
Total Loss (W)	2087	2110	2135	2109

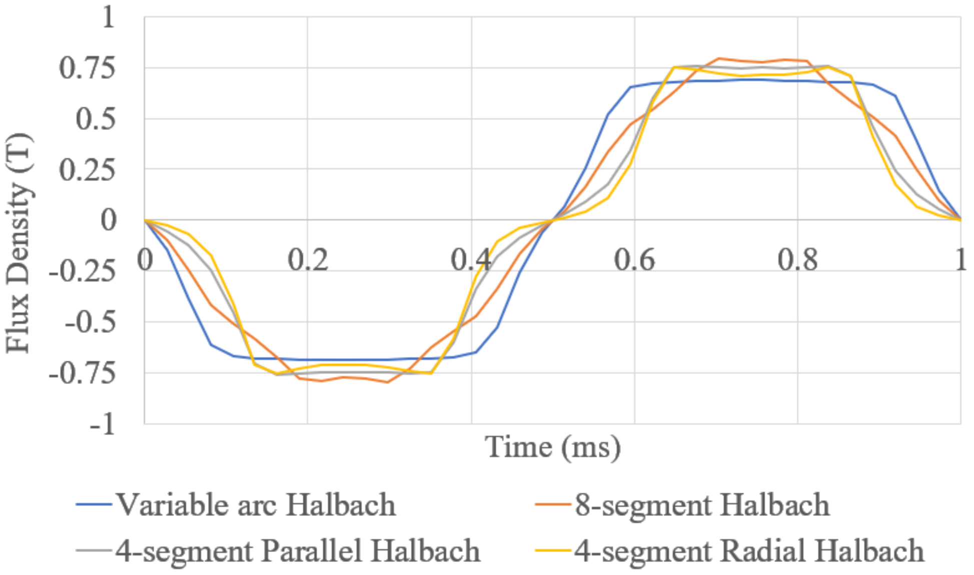

Figure 72. No-load airgap flux density at the stator bore

arc array's peak flux densities, in contrast, are broadened and flattened by the presence of harmonic distortion. The Fast Fourier Transform (FFT) of these no-load airgap flux densities are shown in Figure 73 for each array. The variable arc array, while possessing the highest fundamental harmonic magnitudes, has significant higher order harmonics, particularly the 3rd and 7th orders that contribute to an irregular flux density waveform. Since the torque is ultimately proportional to the airgap flux density, these harmonics in the sinusoid are observed in the electromagnetic torque as torque ripple.

5.5.2 Analytical Equation for Halbach Arrays

Analytical solutions exist to approximate the no-load airgap flux density obtained in radial flux Halbach arrays with rotor back irons which can then be used to provide an estimate of the electromagnetic torque. One of the most well-used equations is from [76],

$$B_{I_r} = B_r \frac{pp}{1+pp} \frac{1-\left(\frac{R_r}{R_m}\right)^{p+1}}{1-\left(\frac{R_r}{R_s}\right)^{2p}} \left[\left(\frac{r}{R_s}\right)^{p-1}\left(\frac{R_m}{R_s}\right)^{p+1} + \left(\frac{R_m}{r}\right)^{p+1}\right]\cos\left(p\theta\right) \tag{35}$$

Where B_{I_r} is the fundamental radial flux density, pp is the number of pole pairs, r is the

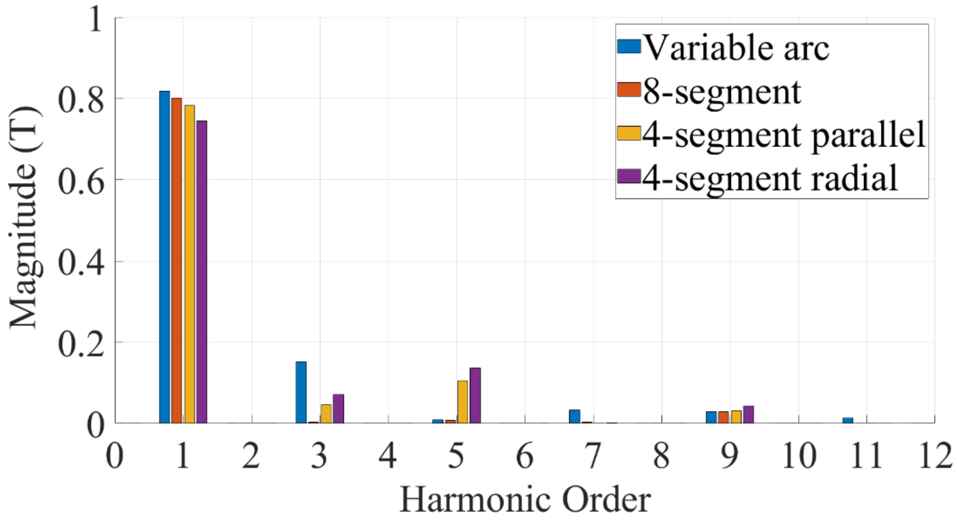

Figure 73. FFT of no-load airgap flux density at the statore bore

given radial distance from rotor's center of rotation, θ is the given arc angle, R_r, R_m, R_s are the rotor yoke radius, magnet radius and stator bore radius, respectively.

This equation makes the following assumptions:

- Infinitely permeable rotor back iron
- The Halbach is one continuous ring
- No end-effects (i.e., infinite axial length)
- No slotting effects from the stator

Use of the equations on the current rotor geometry yields the graph shown in Figure 74. Peak analytical no-load flux density is calculated to be 0.854 Tesla, as compared to the FEA calculated flux densities of 0.818, 0.801 and 0.782 Tesla for the variable arc, 8-segment and 4-segment parallel Halbach arrays, respectively. The 8-segment array most closely approximates the continuous Halbach assumption and is therefore the most applicable to equation (35). It was used as an initial flux density estimate for the 4 MW high speed permanent magnet machine in [58], which also uses an 8-segment Halbach. There are more detailed equations that deal with the effects of magnet segmentation and

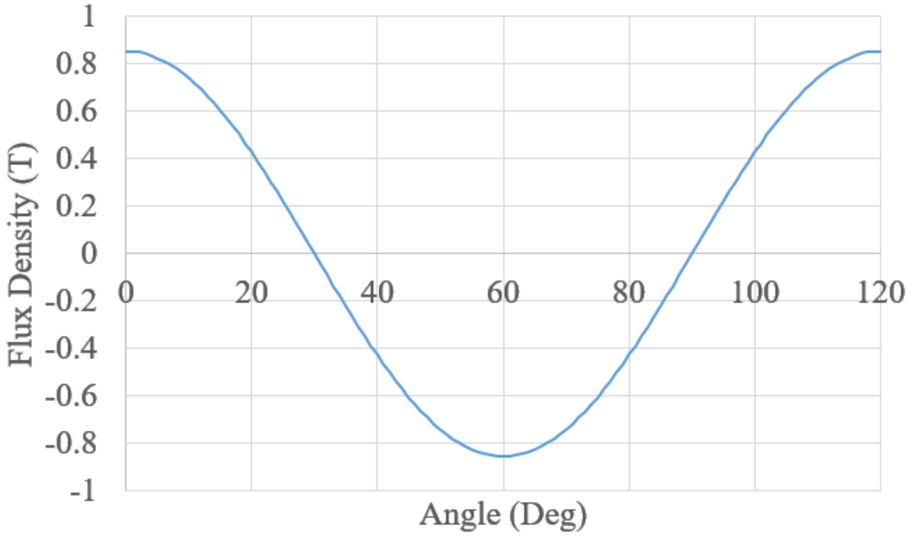

Figure 74. Analytical estimation of fundamental radial flux density in inner rotor design

slotting for regular Halbachs [77], or for variable arc arrays [75] that can improve the analytical estimation, although assumptions of infinite permeability and infinite axial length are still generally employed, and the calculation is typically more labour-intensive to complete.

5.5.3 Chosen Halbach Configuration

The 8-segment Halbach array is ultimately chosen as the preferred Halbach configuration for this design, mainly due to its reasonably high torque capabilities and lowest torque ripple. Table XXXI displays the transient coupled electromagnetic results of the machine simulated in Motor-CAD at peak performance and collected after two iterations. Maximum electromagnetic specific power achieved is 13 kW/kg and it takes 224 seconds for the winding hotspots (which are on the end turns) to reach 180 $°C$. The final temperature distribution is displayed in Figure 75.

Table XXXI. Transient Peak Performance Results

Torque	72 Nm
Speed	20,000 RPM
Torque Ripple	5.1 %
Power	151 kW
Phase Current	115 A_{RMS}
Phase Voltage	704 V
Magnet Loss	36 W
Stator Iron Loss	1150 W
Rotor Iron Loss	4 W
DC Copper Loss	2692 W
Total Loss	3882 W
Electromagnetic Specific Power	13.0 kW/kg
Overheating time	224 s

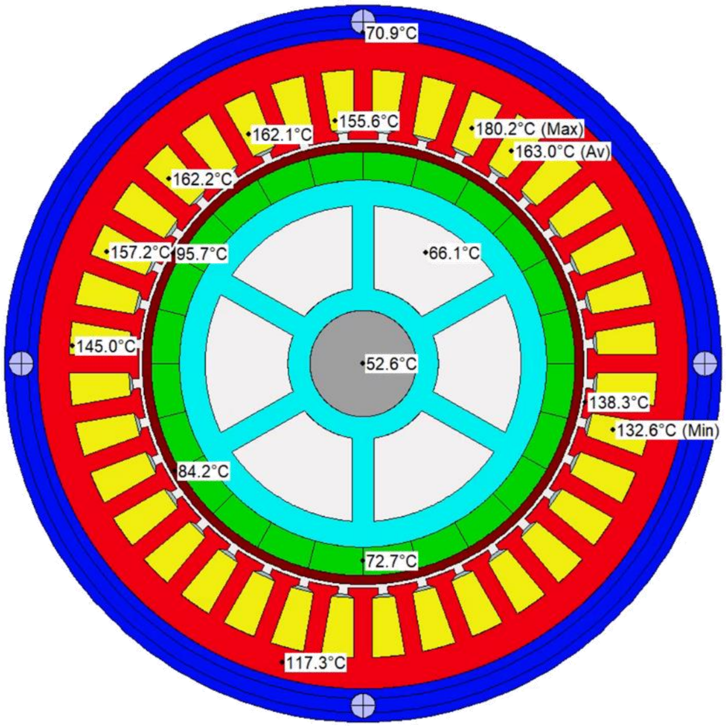

Figure 75. Transient peak performance temperature distribution for final configuration after winding hotspot reaches 180 $^{\circ}C$

Though the initial specifications listed in Table XXI are currently met, it can be seen from the results of Table XXXI that the machine performance is thermally limited. However, its specific power has the potential to be improved further through the implementation of a different cooling system. Cooling jackets, like the kind used in this concept, primarily rely on conduction from the heat generating coils, through the coil insulation, encapsulant, slot liner, stator back iron and housing before finally reaching the liquid coolant. The efficacy of this approach is limited, especially for heat dissipation in the end turns, due to the relatively low thermal conductivities of insulations and encapsulants. Also, the presence of small air gaps between slot liner and stator, as well as stator and housing, greatly increases the thermal contact resistance that heat flux encounters and restricts how much heat can be dissipated from the machine [78]. Heat dissipation can be enhanced through the use of direct cooling approaches, like stator flooding, where the coolant comes into direct contact with the source of heat generation (i.e., the coils or the stator laminations). Direct cooling approaches will increase the mechanical complexity of the machine and are left for future iterations to improve overall power rating.

5.6 Summary

This chapter introduced a proposed electric machine intended for an aerospace application with high specific power. The proof-of-concept is designed to obtain 100 kW of continuous mechanical power with a 150 kW peak condition. The technology demonstrated in this machine is aimed at scalability for a future proposed megawatt-level machine, also for aerospace applications. The initial selection of machine involved narrowing down candidates to just two main designs: The outer rotor 12/10 SPM machine with fractional slot concentrated winding and inner rotor 36/6 SPM with distributed winding. Coupled electromagnetic and thermal simulations are performed for both machines. Despite possessing lower electromagnetic specific power, the inner rotor SPM is selected for further analysis due to mechanical and thermal limitations of the outer rotor design. Four different Halbach magnet arrays are analyzed electromagnetically for the inner rotor configuration: parallel magnetized 4-segment Halbach, radial magnetized 4-segment Halbach, variable arc 4-segment Halbach and 8-segment Halbach. The 8-segment Halbach is selected for the rotor design as it possesses high torque output as well as lowest torque ripple, making it the most attractive magnet arrangement. Finally, a transient electromagnetic and thermal analysis is carried out on the chosen design at 150 kW and demonstrates 13 kW/kg electromagnetic specific power for 224 seconds, before the windings overheat. Future design iterations could improve this specific power rating by increasing insulation temperature ratings, implementing cobalt steel laminations, and using stator immersion cooling instead of a cooling jacket. These changes would allow for higher maximum machine temperatures, higher peak flux densities, lower core losses, and cooler coil temperatures.

6. Conclusions and Future Work

6.1 Conclusions

This thesis explored the use of Halbach arrays for use in electric radial flux and axial flux machines for aerospace applications. Chapter 1 introduced the concepts of Halbach arrays, radial flux and axial flux machines. Chapter 2 presented the development of analytical equations for predicting magnetic fields in axial flux Halbach arrays to be potentially used in coreless electric machines. Several configurations of Halbach were analyzed as examples and showed strong accuracy between prediction and finite element analysis. Chapter 3 presented the development of analytical equations for predicting magnetic fields in axial flux Halbach arrays, to be potentially used in steel core machines. These equations made use of Schwarz-Christoffel mapping techniques whereby the machine was sliced at multiple radii, the geometry transformed from the real plane to the much simpler ζ-plane, the magnetic scalar potential equations solved, then the sliced solution was transformed back to the real plane and amalgamated with the other slices. Chapter 4 used the equations developed in chapter 3 to redesign NASA’s all-electric Maxwell X-57 high lift propulsion radial flux motor as a steel core AFM with Halbach array. A full factorial experiment using key dimensions was performed in order to find the optimal geometry. Finalized comparisons between analytical and finite element analysis results for no-load flux linkage and subsequent peak torque showed highly accurate predictive capability. Two variants were selected from the optimization. One variant resulted in 10 % greater peak torque and power than the RFM, while holding mass and volume constant, whereas the other variant resulted in 10 % less mass and volume, while holding peak torque and efficiency constant. Chapter 5 presented the requirements for a high-speed surface permanent magnet RFM to be constructed as a proof-of-concept for a much larger megawatt machine to be used in aerospace applications. The resultant inner rotor design with 8-segment Halbach array was capable of continuous 100 kW operation and 150 kW peak power operation for limited periods at a time.

6.2 Future Work

There is future work to be performed on the thermal analysis and mechanical design of the high lift axial flux motor concept variants presented in chapter 4 in order to fully compare them against NASA's original radial flux machine, which has had extensive mechanical, thermal, and CFD studies completed. Equivalent temperatures for the magnets and windings were chosen for the AFM electromagnetic study as a placeholder, but depending on the mechanical configuration the temperature rise could be higher or lower than in the radial flux machine. While thermal analysis and CFD verification of the RFM are being performed by other researchers at MARC, mechanical analysis verification and subsequent mechanical design of the AFM was hampered by the limited information that existed for the construction of the original RFM concept, especially as to how it connected to the propeller, and so this would need to be addressed by NASA before proceeding. Improvements can also be made to the 10 % torque/power AFM concept. While it produced 10 % less total loss at 24 Nm than NASA's RFM, at 26.4 Nm (peak power) it struggled to maintain machine losses equivalent to the RFM (at its own peak power of 24 Nm) and exceeded it by 5 %. This may result in unsustainable temperatures within the AFM under continuous operation that limit its peak power use to intermitted loading only. Thermal analysis is needed to verify this, and methods to further reduce the total machine loss can be looked at.

The Schwarz-Christoffel mapping technique developed for Halbach AFMs in chapter 3 worked very well for predicting no load airgap flux densities in the HLM AFM and could be used to accurately estimate the full load torque. While it was tested extensively during the design process of the AFM HLM, it has only been tested on one slot/pole combination (24/20) at one power rating (14 – 15 kW) with one set of materials (N48H magnets, Hiperco 50 steel) to date. Testing should be carried out on other topologies, materials, and power ratings to confirm its applicability to a wider range of machine designs before drawing definitive conclusions abouts its efficacy. Also, it would be nice to collect useful information about other machine operation characteristics like back EMF, torque ripple, magnet and winding loss under full load. High levels of saturation in the presence of both electric and magnetic loading generally make it more difficult to use SC mapping because of the assumptions about linear flux density saturation that Hague's electromagnetic solution makes. Thus, a non-linear electromagnetic solution to the magnetic potential in the airgap should be implemented in order to accurately predict these characteristics under heavy saturation. There would be a trade-off between solution time and accuracy in this case, since non-linear solvers usually increase analysis complexity by carrying out multiple iterations before a solution reaches steady state.

The final area identified for future work is in the design of the 150 kW high-speed radial flux machine presented in chapter 5. As stated, it is intended to be a proof-of-concept for a scaled up megawatt machine. To that end, further electromagnetic, thermal, structural analysis and CFD are being performed by researchers at McMaster that will culminate in mechanical design, test, and verification to ensure it is a viable concept for the future megawatt prototype, also that the analyses performed match real world testing data. It would also be nice to improve the cooling efficacy of the machine, such that it could sustain 150 kW continuously, instead of its current limit of 100 kW, and so this is identified as an area of future research too. This could be achieved, for example, through an oil end turn spray cooling approach, in combination with the stator back iron coolant jacket, since most of the machine's losses are generated in the windings and stator core.

References

[1] "© [2022] IEEE. Reprinted, with permission, from [A. Forsyth, G. Pietrini, A. Callegaro and A. Emadi, Generalized Analytical Solution for N-Segment Axial Flux Halbach Arrays, 2022 IEEE Transportation Electrification Conference & Expo (ITEC), July 2022]."

[2] Z. Q. Zhu and D. Howe, "Halbach permanent magnet machines and applications: A review," *IEE Proceedings: Electric Power Applications*, vol. 148, no. 4. pp. 299–308, 2001, doi: 10.1049/ip-epa:20010479.

[3] D. Hanselman, *Brushless permanent magnet motor design*, 2nd ed. Ohio: Magna Physics Publishing, 2003.

[4] J. R. Hendershot and T. J. E. Miller, *Design of brushless permanent magnet machines*, 2nd ed. Venice, Flordia: Motor Design Books LLC, 2010.

[5] J. Hagedorn, F. Sell-Le Blanc, and J. Fleischer, *Handbook of coil winding: Technologies for efficient electrical wound products and their automated production*. Berlin, Germany: Springer Nature, 2017.

[6] J. F. Gieras, R.-J. Wang, and M. J. Kamper, *Axial Flux Permanet Magnet Brushless Machines*, 2nd ed. Springer, 2008.

[7] W. Tong, *Mechanical design of electric motors*. Boca Raton, Flordia: CRC PRess, Taylor & Francis Group, 2014.

[8] B. Zhang, T. Seidler, R. Dierken, and M. Doppelbauer, "Development of a yokeless and segmented armature axial flux machine," *IEEE Trans. Ind. Electron.*, vol. 63, no. 4, pp. 2062–2071, 2016, doi: 10.1109/TIE.2015.2500194.

[9] D. Schweigert *et al.*, "On the impact of maximum speed on the power density of electromechanical powertrains," *Vehicles*, vol. 2, no. 2, pp. 365–397, 2020, doi: 10.3390/vehicles2020020.

[10] D. Winterborne, N. Stannard, L. Sjoberg, and G. Atkinson, “An air-cooled yasa motor for in-wheel electric vehicle applications,” *IEEE Trans. Ind. Appl.*, vol. 56, no. 6, pp. 6448–6455, 2020, doi: 10.1109/TIA.2020.3025267.

[11] M. F. Khatab, Z. Zhu, H. Li, and Y. Liu, “Comparative study of axial flux magnetically geared machine with conventional axial flux YASA machine,” *2018 IEEE Int. Magn. Conf. INTERMAG 2018*, 2018, doi: 10.1109/INTMAG.2018.8508859.

[12] F. Giulii Capponi, G. De Donato, and F. Caricchi, “Recent advances in axial-flux permanent-magnet machine technology,” *IEEE Trans. Ind. Appl.*, vol. 48, no. 6, pp. 2190–2205, 2012, doi: 10.1109/TIA.2012.2226854.

[13] J. Chang *et al.*, “Design of a new type yokeless and segmented armature axial flux machine,” *Int. J. Appl. Electromagn. Mech.*, vol. 62, no. 4, pp. 823–834, 2020, doi: 10.3233/JAE-190085.

[14] F. Sahin, A. M. Tuckey, and A. J. A. Vandenput, “Design, development and testing of a high-speed axial-flux permanent-magnet machine,” *2001 IEEE Ind. Appl. Conf.*, 2001.

[15] Z. Zhang, C. Wang, and W. Geng, “Design and optimization of halbach-array pm rotor for high-speed axial-flux permanent magnet machine with ironless stator,” *IEEE Trans. Ind. Electron.*, vol. 67, no. 9, pp. 7269–7279, 2020, doi: 10.1109/TIE.2019.2944033.

[16] A. Parviainen, M. Niemelä, and J. Pyrhönen, “Modeling of axial flux permanent-magnet machines,” *IEEE Trans. Ind. Appl.*, vol. 40, no. 5, pp. 1333–1340, 2004, doi: 10.1109/TIA.2004.834086.

[17] W. K. Thompson, “Three-dimensional field solutions for multi-pole cylindrical halbach arrays in an axial orientation,” *NASA Glenn Res. Cent.*, no. 2006–214359, 2006.

[18] K. Li and J. Z. Bird, “A 3-D analytical model of a halbach axial magnetic coupling,” *2016 Int. Symp. Power Electron. Electr. Drives, Autom. Motion, SPEEDAM 2016*, pp. 1448–1454, 2016, doi: 10.1109/SPEEDAM.2016.7525881.

[19] T. C. O’Connell and P. T. Krein, “The Schwarz-Christoffel analytical method applied to electric machine slot shape optimization,” *Proc. IEEE Int. Electr. Mach. Drives Conf. IEMDC 2007*, vol. 1, pp. 341–346, 2007, doi: 10.1109/IEMDC.2007.382690.

[20] J. Laksar and L. Veg, “Reduced schwarz-christoffel conformal mapping in surface-mounted PMSM,” in *2018 18th International Conference on Mechatronics - Mechatronika (ME),* 2019, no. December 2018.

[21] L. Xue, L. Luo, and J. Pu, “Eddy current calculation of a high-speed slotted machine with Halbach magnetization at no-load condition,” *IEEE Trans. Magn.*, vol. 55, no. 11, 2019, doi: 10.1109/TMAG.2019.2932653.

[22] E. Ilhan, E. T. Motoasca, J. J. Paulides, and E. A. Lomonova, “Conformal mapping: Schwarz-Christoffel method for flux-switching PM machines,” *Math. Sci.*, vol. 6, no. 1, pp. 1–9, 2012, doi: 10.1186/2251-7456-6-37.

[23] H. Mirahki, M. Moallem, M. Ebrahimi, and B. Fahimi, “Combined on/off and conformal mapping method for magnet shape optimisation of SPMSM,” *IET Electr. Power Appl.*, vol. 12, no. 9, pp. 1365–1370, 2018, doi: 10.1049/iet-epa.2018.5166.

[24] T. A. Driscoll and L. N. Trefethen, *Schwarz-Christoffel mapping (Cambridge monographs on applied and computational mathematics)*. Cambrige, UK: Cambridge University Press, 2004.

[25] H. Mirahki, M. Moallem, M. Ebrahimi, and B. Fahimi, “Asymmetrical magnet shape optimization based on s-c mapping for torque profile mitigation in unidirectional application of spms machin,” *IEEE Trans. Transp. Electrif.*, vol. 5, no. 3, pp. 630–637, 2019, doi: 10.1109/TTE.2019.2928250.

[26] P. Upadhyay, E. Naveen Kumar, and K. Ragavan, "Assessment of noise reduction in switched reluctance motor using conformal mapping," *Proc. 2018 IEEE Int. Conf. Power Electron. Drives Energy Syst. PEDES 2018*, vol. 1, no. 8, pp. 5–8, 2018, doi: 10.1109/PEDES.2018.8707581.

[27] B. Rezaeealam and F. Rezaee-Alam, "An improved conformal mapping method for magnetic field analysis in surface mounted permanent magnet motors," *COMPEL - Int. J. Comput. Math. Electr. Electron. Eng.*, vol. 36, no. 4, pp. 892–905, 2017, doi: 10.1108/COMPEL-07-2016-0284.

[28] T. C. O'Connell and P. T. Krein, "A Schwarz-Christoffel-based analytical method for electric machine field analysis," *IEEE Trans. Energy Convers.*, vol. 24, no. 3, pp. 565–577, 2009, doi: 10.1109/TEC.2009.2025412.

[29] B. Rezaeealam and F. Rezaee-Alam, "Optimization of permanent magnet synchronous motors using conformal mappings," *Appl. Comput. Electromagn. Soc. J.*, vol. 32, no. 10, pp. 915–923, 2017.

[30] K. Abbaszadeh and F. R. Alam, "On-load field component separation in surface-mounted permanent-magnet motors using an improved conformal mapping method," *IEEE Trans. Magn.*, vol. 52, no. 2, 2016, doi: 10.1109/TMAG.2015.2493150.

[31] A. Hanic, D. Zarko, D. Kuhinek, and Z. Hanic, "On-load analysis of saturated surface permanent magnet machines using conformal mapping and magnetic equivalent circuits," *IEEE Trans. Energy Convers.*, vol. 33, no. 3, pp. 915–924, 2018, doi: 10.1109/TEC.2017.2789322.

[32] P. Zhang, Q. Ma, and X. Ping, "Modeling and analysis of switched reluctance machines using an improved conformal mapping method," *2019 22nd Int. Conf. Electr. Mach. Syst. ICEMS 2019*, pp. 4–7, 2019, doi: 10.1109/ICEMS.2019.8922515.

[33] K. Boughrara, R. Ibtiouen, D. Zarko, O. Touhami, and A. Rezzoug, "Magnetic

field analysis of external rotor permanent-magnet synchronous motors using conformal mapping," *IEEE Trans. Magn.*, vol. 46, no. 9, pp. 3684–3693, 2010, doi: 10.1109/TMAG.2010.2047508.

[34] A. Tikellaline, K. Boughrara, and N. Takorabet, "Magnetic field analysis of double excited synchronous motor using numerical conformal mapping," in *5th International Conference on Electrical Engineering*, 2017, pp. 1–6.

[35] K. Abbaszadeh and F. R. Alam, "On-Load Field Component Separation in Surface-Mounted Permanent-Magnet Motors Using an Improved Conformal Mapping Method," *IEEE Trans. Magn.*, vol. 52, no. 2, pp. 333–344, 2016, doi: 10.1109/TMAG.2015.2493150.

[36] K. Ramakrishnan, D. Zarko, A. Hanic, and G. Mastinu, "Improved method for field analysis of surface permanent magnet machines using Schwarz-Christoffel transformation," *IET Electr. Power Appl.*, vol. 11, no. 6, pp. 1067–1075, 2017, doi: 10.1049/iet-epa.2016.0712.

[37] Q. Li, B. Zhang, and A. Liu, "Electromagnetic force analysis of eccentric axial flux permanent magnet machines," *Math. Probl. Eng.*, vol. 2020, 2020, doi: 10.1155/2020/6194317.

[38] Y. Huang, B. Guo, A. Hemeida, and P. Sergeant, "Analytical modeling of static eccentricities in axial flux permanent-magnet machines with concentrated windings," *Energies*, vol. 9, no. 11, 2016, doi: 10.3390/en9110892.

[39] B. Hague, *Electromagnetic problems in electrical engineering: An elementary treatise on the application of the principles of electromagnetism to the theory of the magnetic field and of the mechanical forces in electrical machinery and apparatus*. H. Milford, 1929.

[40] K. Drobnič, L. Gašparin, and R. Fišer, "Fast and accurate model of interior permanent-magnet machine for dynamic characterization," *Energies*, vol. 12, no. 5, 2019, doi: 10.3390/en12050783.

[41] D. L. Hall *et al.*, “Development of a maxwell x-57 high lift motor reference design,” *AIAA Propuls. Energy Forum Expo. 2019*, no. August, pp. 1–24, 2019, doi: 10.2514/6.2019-4481.

[42] A. Dubois, M. van der Geest, J. Ben Bevirt, S. Clarke, R. J. Christie, and N. K. Borer, “Design of an electric propulsion system for SCEPTOR,” *16th AIAA Aviat. Technol. Integr. Oper. Conf.*, pp. 1–29, 2016.

[43] NASDA, “How will the X-57 be built?” https://www.nasa.gov/specials/X57/modification.html (accessed May 21, 2023).

[44] Elektrisola, “Single wire vs. total cross section & filling factor of litz wire.” https://www.elektrisola.com/sites/default/files/glazed_builder_images/03_RelationshipSingleWireLitzCrossSectionFillingFactor.png?fid=558 (accessed Feb. 01, 2023).

[45] NEMA, “MW 1000 calculator, 28 AWG.” https://www.nema.org/directory/products/mw-1000-calculator?size=28 (accessed Feb. 02, 2023).

[46] ANSYS, “Using litz wire in Maxwell 2D and 3D simulations,” 2021. https://www.ansys.com/blog/using-litz-wire-in-maxwell-2d-and-3d-simulations (accessed Feb. 08, 2023).

[47] N. K. Borer and M. D. Patterson, “X-57 high-lift propeller control schedule development,” *Aiaa Aviat. 2020 Forum*, vol. 1 PartF, pp. 1–17, 2020, doi: 10.2514/6.2020-3091.

[48] Tecnam, “P2006T twin engine aircraft.” https://tecnam.com/aircraft/p2006t/ (accessed Mar. 01, 2023).

[49] Elektrisola, “Litz wire.” https://www.elektrisola.com/en/Litz-Wire/Info#filling-factors (accessed Mar. 04, 2023).

[50] Elektrisola, “Profiled litz wire.” https://www.elektrisola.com/en/Products/Litz-

Wire/Products/Profiled (accessed Apr. 04, 2023).

[51] R. H. Jansen, C. Bowman, and A. Jankovsky, “Sizing power components of an electrically driven tail cone thruster and a range extender,” *16th AIAA Aviat. Technol. Integr. Oper. Conf.*, pp. 1–9, 2016, doi: 10.2514/6.2016-3766.

[52] C. Lents, L. Hardin, J. Rheaume, and L. Kohlman, “Parallel hybrid gas-electric geared turbofan engine conceptual design and benefits analysis,” *52nd AIAA/SAE/ASEE Jt. Propuls. Conf. 2016*, pp. 1–13, 2016, doi: 10.2514/6.2016-4610.

[53] C. Dong, Y. Qian, Y. Zhang, and W. Zhuge, “A review of thermal designs for improving power density in electrical machines,” *IEEE Trans. Transp. Electrif.*, vol. 6, no. 4, pp. 1386–1400, 2020, doi: 10.1109/TTE.2020.3003194.

[54] H. D. Kim, J. L. Felder, M. T. Tong, and M. J. Armstrong, “Revolutionary aeropropulsion concept for sustainable aviation: turboelectric distributed propulsion,” *21st Int. Symp. Air Breath. Engines*, pp. 1–12, 2013.

[55] NASA, “Ohio State University induction machine,” 2022. https://www1.grc.nasa.gov/aeronautics/eap/technology/electric-machines/induction-machine/ (accessed Aug. 22, 2022).

[56] Y. Chen, R. Sanchez, A. Yoon, and K. S. Haran, “Mechanical design considerations of an ‘ironless,’ high-specific-power electric machine,” *IEEE Trans. Transp. Electrif.*, vol. 3, no. 4, pp. 855–863, 2017, doi: 10.1109/TTE.2017.2733763.

[57] C. Anghel, “Hybrid electric propulsion technologies 1MW high efficiency generator [PowerPoint Slides],” 2015. [Online]. Available: https://www.nianet.org/ODM/presentations/Cristian_Anghel_-_Honeywell_-_Honeywell_Technologies_for_Hybrid_Electric_Propulsion_(002).pdf.

[58] D. Golovanov *et al.*, “4 MW class high power-density generator for future hybrid-

electric aircraft," *IEEE Trans. Transp. Electrif.*, vol. 7, no. 4, pp. 2952–2964, 2021, doi: 10.1109/TTE.2021.3068928.

[59] B. Sampson, "Honeywell's 1MW generator for hybrid-electric aircraft passes testing milestone," *Aerospace Testing International*, Jun. 2022.

[60] Rolls-Royce, "Rolls-Royce hybrid-electric propulsion system sets megawatt milestone." https://www.rolls-royce.com/media/press-releases/2021/07-12-2021-rr-hybrid-electric-propulsion-system-sets-megawatt-milestone.aspx (accessed Sep. 07, 2022).

[61] E. F. Hammond, W. S. Neff, and W. J. Shilling, "A 2.5-MVA high-voltage lightweight generator," *J. Aircr.*, vol. 16, no. 1, pp. 55–61, 1979, doi: 10.2514/3.58484.

[62] K. Yost *et al.*, "Megawatt scale hardware-in-the-loop testing of a high speed generator," *Ameican Soc. Nav. Eng.*, no. 88, 2012, [Online]. Available: http://www.dtic.mil/docs/citations/ADA558395.

[63] Wright Patterson AFB, "2.5 MW electrodynamics generator." https://www.wpafb.af.mil/News/Photos/igphoto/2000568240/ (accessed Aug. 01, 2022).

[64] Y. Wang, S. Nuzzo, H. Zhang, W. Zhao, C. Gerada, and M. Galea, "Challenges and opportunities for wound field synchronous generators in future More Electric Aircraft," *IEEE Trans. Transp. Electrif.*, vol. 6, no. 4, pp. 1466–1477, 2020, doi: 10.1109/TTE.2020.2980189.

[65] Collins Aerospace, "Collins Aerospace completes preliminary design of 1MW electric motor for Pratt & Whitney Canada's regional hybrid-electric flight demonstrator," 2022. https://www.collinsaerospace.com/news/news/2022/07/collins-complete-preliminary-design-of-1mw-electric-motor-for-pratt-whitney-canada (accessed Jul. 29, 2022).

[66] W. Palmer, “Electric skies: Boeing joins GE and NASA’s hybrid electric flight project,” 2022. https://www.ge.com/news/reports/electric-skies-boeing-joins-ge-and-nasas-hybrid-electric-flight-project (accessed Jul. 29, 2022).

[67] Rolls-Ryoce, “Rolls-Royce generator delivered for most powerful hybrid-electric propulsion system in aerospace,” 2021. https://www.rolls-royce.com/media/press-releases/2021/22-07-2021-rr-generator-delivered-for-most-powerful-hybrid-electric-propulsion-system-in-aerospace.aspx (accessed Sep. 11, 2022).

[68] M. K. Bradley, T. J. Allen, and C. K. Droney, “Subsonic ultra green aircraft research: Phase II - volume III - truss braced wing design exploration,” *NASA Tech. Rep.*, vol. CR–2015-21, no. April 2014, p. 76, 2015.

[69] NASA and Glenn Research Center, “Airplane concepts: Hybrid electric,” 2022. https://www1.grc.nasa.gov/aeronautics/eap/airplane-concepts/hybrid-electric/ (accessed Aug. 23, 2022).

[70] D. Ishak, Z. Q. Zhu, and D. Howe, “Permanent-magnet brushless machines with unequal tooth widths and similar slot and pole numbers,” *IEEE Trans. Ind. Appl.*, vol. 41, no. 2, pp. 584–590, 2005, doi: 10.1109/TIA.2005.844380.

[71] M. Houle and A. Langlois, “Liquid cooling arrangement for electric machines.” U.S. Patent 6 819 016 B2, Nov. 16, 2004.

[72] R. Sanchez, “Development of a high power density rotor,” University of Illinois at Urbana-Champaign, 2017.

[73] Tesla, “2012 Tesla Model S specifications and features.” https://www.tesla.com/sites/default/files/2012_model_s_specifications_and_features.pdf (accessed Jun. 02, 2022).

[74] G. Bower, “Engineering analysis of new Tesla Model S Plaid supercar,” 2021. https://insideevs.com/news/514385/tesla-models-plaid-engineering-analysis/ (accessed Jun. 02, 2022).

[75] P. H. Mellor and R. Wrobel, “Optimization of a multipolar permanent-magnet rotor comprising two arc segments per pole,” *IEEE Trans. Ind. Appl.*, vol. 43, no. 4, pp. 942–951, 2007, doi: 10.1109/TIA.2007.900479.

[76] Z. P. Xia, Z. Q. Zhu, and D. Howe, “Analytical magnetic field analysis of halbach magnetized permanent-magnet machines,” *IEEE Trans. Magn.*, vol. 40, no. 4 I, pp. 1864–1872, 2004, doi: 10.1109/TMAG.2004.828933.

[77] Y. Shen and Z. Q. Zhu, “General analytical model for calculating electromagnetic performance of permanent magnet brushless machines having segmented Halbach array,” *IET Electr. Syst. Transp.*, vol. 3, no. 3, pp. 57–66, 2013, doi: 10.1049/iet-est.2012.0055.

[78] S. Sequeira *et al.*, “Validation and parametric investigations using a lumped thermal parameter model of an internal permanent magnet motor,” *ASME 2020 Int. Tech. Conf. Exhib. Packag. Integr. Electron. Photonic Microsystems, InterPACK 2020*, no. October, 2020, doi: 10.1115/IPACK2020-2550.

Appendix

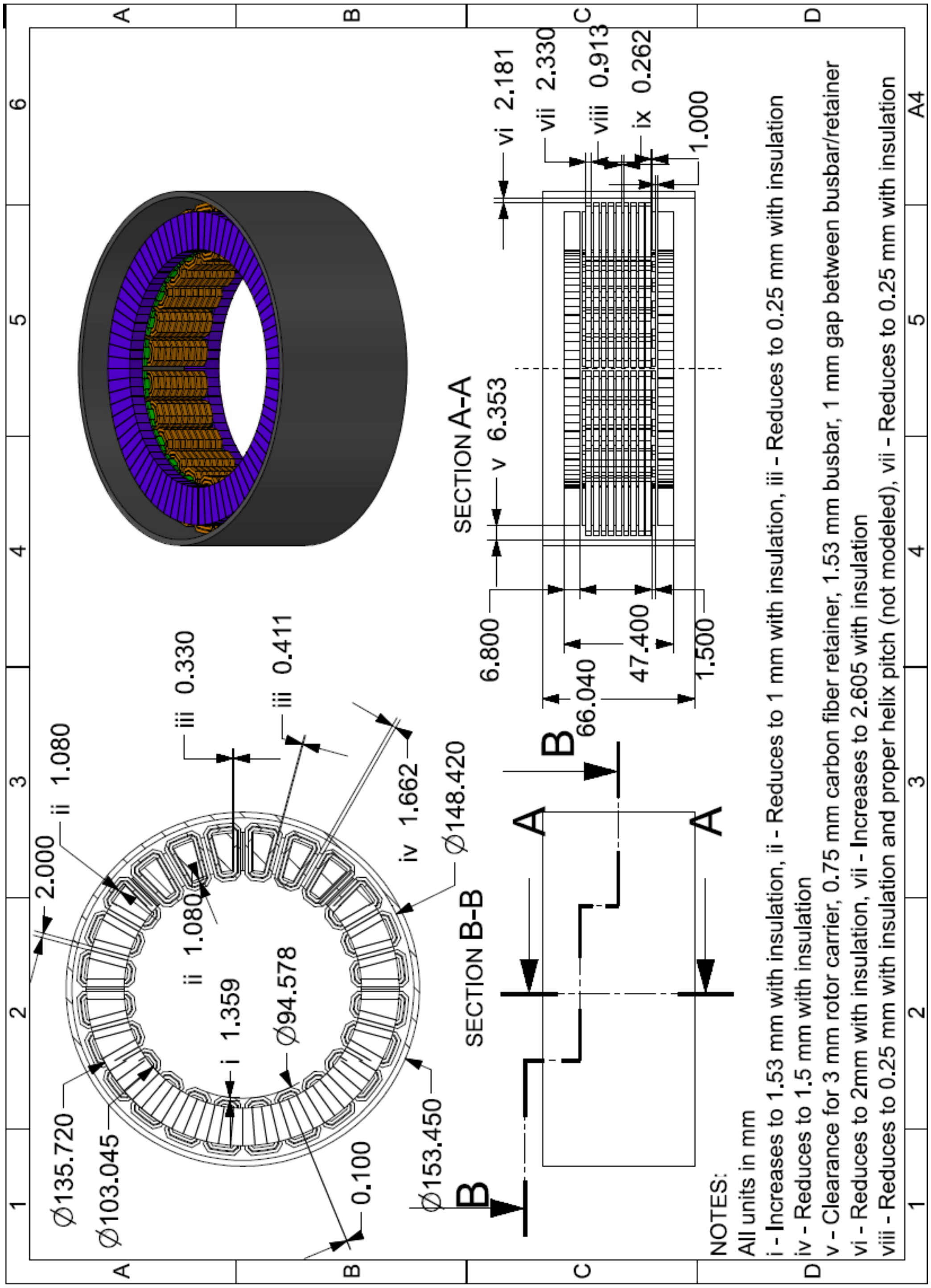

NOTES:
All units in mm
i - Increases to 1.53 mm with insulation, ii - Reduces to 1 mm with insulation, iii - Reduces to 0.25 mm with insulation
iv - Reduces to 1.5 mm with insulation
v - Clearance for 3 mm rotor carrier, 0.75 mm carbon fiber retainer, 1.53 mm busbar, 1 mm gap between busbar/retainer
vi - Reduces to 2mm with insulation, vii - Increases to 2.605 with insulation
viii - Reduces to 0.25 mm with insulation and proper helix pitch (not modeled), vii - Reduces to 0.25 mm with insulation

Figure 76. Dimensions of 90 % mass/volume AFM design

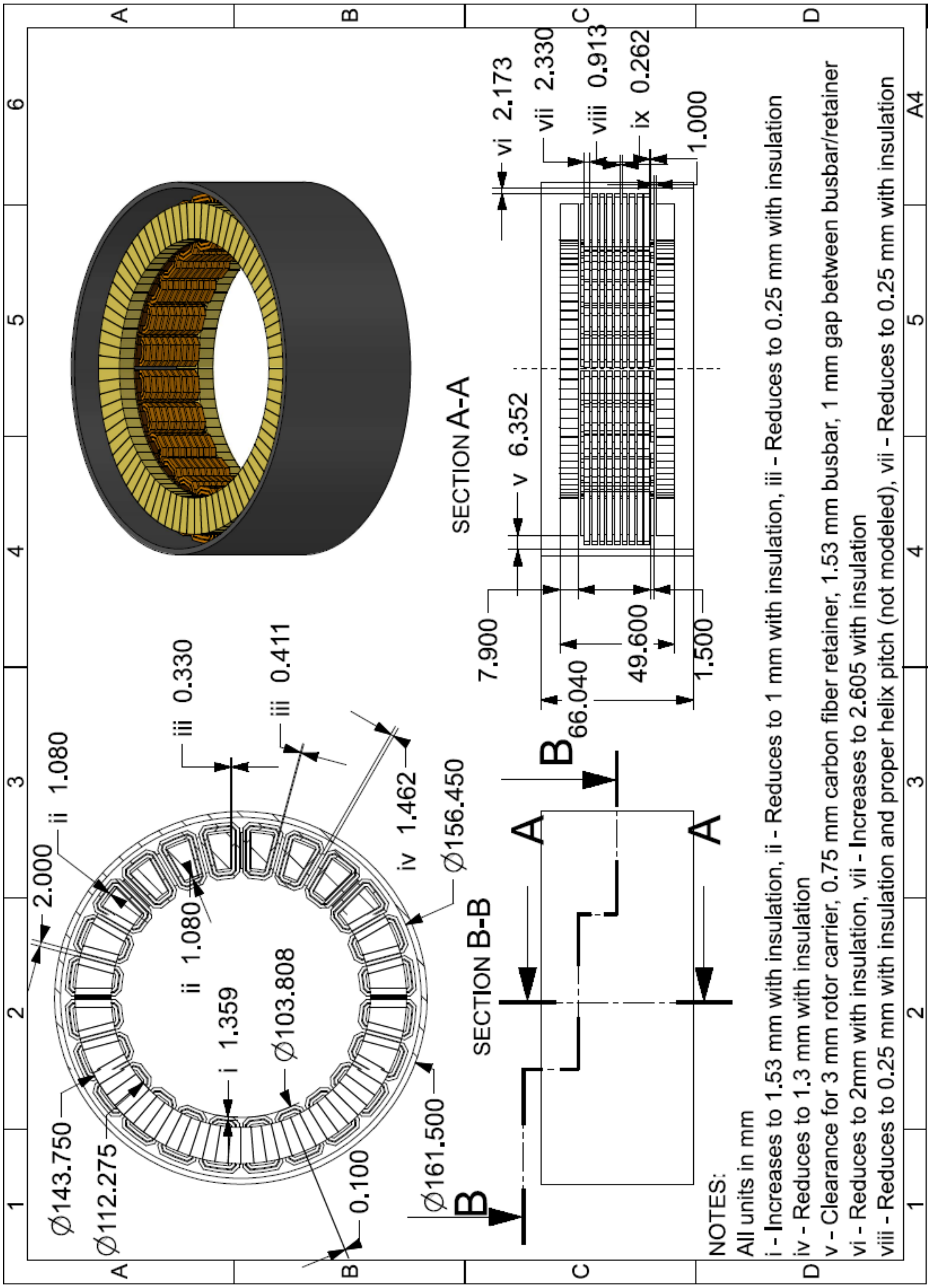

NOTES:
All units in mm
i - Increases to 1.53 mm with insulation, ii - Reduces to 1 mm with insulation, iii - Reduces to 0.25 mm with insulation
iv - Reduces to 1.3 mm with insulation
v - Clearance for 3 mm rotor carrier, 0.75 mm carbon fiber retainer, 1.53 mm busbar, 1 mm gap between busbar/retainer
vi - Reduces to 2mm with insulation, vii - Increases to 2.605 with insulation
viii - Reduces to 0.25 mm with insulation and proper helix pitch (not modeled), vii - Reduces to 0.25 mm with insulation

Figure 77. Dimensions of 110 % mass/volume AFM design